

**PHOSPHINE OXIDES, FERROCENE, AND VOLATILE ORGANIC
COMPOUNDS ADSORBED ON SURFACES: A SOLID-STATE NMR STUDY**

A Dissertation

by

PATRICK JAMES HUBBARD

Submitted to the Office of Graduate and Professional Studies of
Texas A&M University
in partial fulfillment of the requirements for the degree of

DOCTOR OF PHILOSOPHY

Chair of Committee,	Janet Bluemel
Committee Members,	Kim Dunbar
	Terry Creasy
	David Powers
Head of Department,	Simon North

May 2020

Major Subject: Chemistry

Copyright 2020 Patrick James Hubbard

ABSTRACT

Adsorption processes are very important in everyday life and in academia. They are used in chromatography and to remove pollutants from water sources or even to capture carbon dioxide. Despite the importance of adsorption, additional knowledge about the interactions between the adsorbate and the surface is still needed.

Towards this end, new mobility studies were performed in order to gain more insight into the adsorption process and the dynamics of adsorbates on the surface of a support. First, triphenylphosphine oxide was adsorbed on alumina and the disappearance of the chemical shift anisotropy (CSA) of the ^{31}P solid-state NMR signal showed that one of the mobility modes must resemble fast solution-like isotropic reorientation.

This principle was further investigated with ferrocene on activated carbon and silica. Again, a complete collapse of the CSA in the ^{13}C solid-state NMR spectra indicated isotropic mobility of the molecules on the surface of a support. In both cases, complete solid-state NMR analysis, including quantifying the enthalpy of adsorption, was performed.

Finally, in collaboration with a waste management company a prototype air purification system was designed for the removal of odorous volatile organic compounds (VOCs). The prototype performed well and removed the odor of a typical dumpster during the first four days of use. In future applications of the prototype the longevity will be increased by application of larger amounts of absorber and a different oxidizer.

ACKNOWLEDGEMENTS

I would like to thank my committee chair, Dr. Bluemel, and my committee members, Dr. Dunbar, Dr. Powers, and Dr. Creasy, for their guidance and support throughout the course of this research.

I would also like to thank Dr. Bakhmutov for showing me how to use the solid-state NMR spectrometer and always being there to answer questions.

CONTRIBUTORS AND FUNDING SOURCES

Contributors

The research described in this thesis was supervised by the committee chair, Dr. Janet Bluemel, and supported by the committee members, Dr. Kim Dunbar, Dr. David Powers of the Department of Chemistry, and Dr. Terry Creasy of the Department of Materials Science and Engineering. Dr. Bakhmutov assisted in using the solid-state NMR spectrometer for sample analyses, simulations of spectra and data evaluation. Dr. Nattamai Bhuvanesh performed one single crystal X-ray structure. All other work conducted for the thesis was completed by the student independently.

Funding Sources

This work was supported by the National Science Foundation (CHE-1300208 and CHE-1900100), by Waste Equipment LLC, and by the Department of Chemistry of Texas A&M University.

TABLE OF CONTENTS

	Page
ABSTRACT	ii
ACKNOWLEDGEMENTS	iii
CONTRIBUTORS AND FUNDING SOURCES.....	iv
TABLE OF CONTENTS	v
LIST OF FIGURES.....	vii
LIST OF TABLES	xii
CHAPTER I INTRODUCTION	1
Overview	1
Solid-State Nuclear Magnetic Resonance	4
Magic Angle Spinning (MAS)	6
Chemical Shift Anisotropy (CSA)	7
Quadrupolar Interactions.....	9
Surface Coverage and Adsorbates.....	11
Phosphine Oxides.....	12
Ferrocene.....	14
Volatile Organic Compounds (VOCs).....	16
Silica and Alumina as Support Materials.....	17
Conclusion.....	19
References	19
CHAPTER II ADSORPTION OF TRIPHENYLPHOSPHINE OXIDE ON ALUMINA	26
Introduction.....	26
Results and Discussion.....	28
Conclusions	47
Experimental Section	48
References	50

CHAPTER III FERROCENE ADSORBED ON SILICA AND ACTIVATED CARBON SURFACES: A SOLID-STATE NMR STUDY OF MOLECULAR DYNAMICS AND SURFACE INTERACTIONS	55
Introduction	55
Results and Discussion.....	61
Conclusions	87
Experimental	88
References	90
CHAPTER IV ADSORPTION OF VOLATILE ORGANIC COMPOUNDS	98
Introduction	98
Results and Discussion.....	103
Conclusion.....	126
Experimental Section	127
References	129
CHAPTER V CONCLUSION	131
APPENDIX A	133

LIST OF FIGURES

	Page
Figure 1. Depiction of the internal components of a solid-state probe and rotor.....	6
Figure 2. ^{31}P CP/MAS spectra of polycrystalline triphenylphosphine at different rotational speeds. ²⁰	8
Figure 3. ^{31}P MAS spectra of triphenylphosphine adsorbed on silica. ²⁰	8
Figure 4. ^2H Wideline spectrum of Cp₂Fe-d₂	10
Figure 5. 2D Projection of 1 used to calculate its footprint on an idealized surface.....	11
Figure 6. Three possible loadings of molecules on a surface.....	12
Figure 7. Possible modes of translational and rotational mobility of Ph ₃ PO (TPPO, 1), adsorbed on alumina in a submonolayer. The jump from one OH group to the next involves a temporary detachment from the surface.	28
Figure 8. Static $^{31}\text{P}\{^1\text{H}\}$ NMR spectra of samples 2 , 4 , and polycrystalline 1 . For the simulated and calculated $^{31}\text{P}\{^1\text{H}\}$ MAS NMR spectrum of 1 , spinning at 5 kHz, see Figure A1.	31
Figure 9. $^{13}\text{C}\{^1\text{H}\}$ CP/MAS NMR spectra of polycrystalline 1 (8.2 kHz, top) and 4 (8.0 kHz with direct ^{13}C excitation, bottom) at room temperature.	32
Figure 10. $^{31}\text{P}\{^1\text{H}\}$ static NMR spectra of 2 to 5 , recorded at 295 K. For the experimental and simulated spectra of 5 see Figure A2.	33
Figure 11. ^{31}P NMR signal intensities (arbitrary units) when using an inversion-recovery pulse sequence at 295 K for a static (0 kHz, ○) and a spinning sample (4 kHz, ■) of 3 . The inversion-recovery curves were treated with a stretched exponential $I(t) = \exp(-t/T_1)^\beta$. The solid lines were obtained with a β of 0.9 and $T_1 = 1.5$ s for the spinning, and $\beta = 0.85$ and $T_1 = 1.4$ s for the static case.	35
Figure 12. Temperature dependent static $^{31}\text{P}\{^1\text{H}\}$ NMR spectra of sample 4 , recorded at the indicated temperatures. For the experimental and simulated NMR spectrum, obtained at 253 K, see Figure A3.....	36
Figure 13. $^{31}\text{P}\{^1\text{H}\}$ NMR spectrum of static 2 recorded at 295 K and $^{31}\text{P}\{^1\text{H}\}$ MAS spectra of 4 with spinning speeds of 3 and 4 kHz at 183 K. For the experimental and simulated $^{31}\text{P}\{^1\text{H}\}$ NMR of 4 , spinning at 4 kHz at 183 K..	37

Figure 14. Temperature dependence of the rate constant K_{exch} , presented as the correlation of $\ln(K_{\text{exch}})$ with $1/T$. The values were obtained by lineshape analysis of the variable temperature static $^{31}\text{P}\{^1\text{H}\}$ NMR spectra of 4	40
Figure 15. Dependence of the exchange constant K_{exch} on the surface coverage at 295 K.	42
Figure 16. The temperature dependence of the ^{31}P T_1 time in coordinates $\ln T_1$ versus $1000/T$ obtained for a static sample of 4 . The solid line corresponds to the treatment of the experimental data according to equation (1).	44
Figure 17. ^1H MAS NMR spectrum of 4 (4 kHz, 295 K).	46
Figure 18. Room temperature $^{13}\text{C}\{^1\text{H}\}$ NMR spectra of polycrystalline ferrocene, 1 at the indicated MAS spinning speeds.	63
Figure 19. Static ^2H NMR of 2 at 345 K and 175 K. The top spectrum shows the experimental and simulated static spectra at 295 K; the sharp signal in the center is an artefact appearing often in solid-echo experiments.	65
Figure 20. $^{29}\text{Si}\{^1\text{H}\}$ MAS NMR spectra of pristine dried silica (top) and 1-75%-SiO₂ (bottom), recorded at room temperature with a spinning rate of 3.1 kHz.	66
Figure 21. $^{13}\text{C}\{^1\text{H}\}$ NMR spectra of the static sample 1-75%-SiO₂ recorded at the indicated temperatures.	67
Figure 22. Two potential motional modes leading to a sharp carbon resonance of ferrocene in 1-75%-SiO₂ . The broken line circles indicate the surface of idealized pores of the support.	69
Figure 23. $^{13}\text{C}\{^1\text{H}\}$ MAS NMR spectra of 1-75%-SiO₂ recorded at 180 K with the indicated spinning speeds. The top spectrum shows the simulation of the spectrum obtained at 850 Hz, corresponding to the CSA parameters given in Table 1.	71
Figure 24. Simulation of the $^{13}\text{C}\{^1\text{H}\}$ NMR spectrum of 1-75%-SiO₂ at 233 K. The large isotropically moving component is represented by the green line, the low intensity CSA pattern of the surface-attached ferrocene molecules is drawn in red.	72
Figure 25. Temperature dependence of the equilibrium constant (K_{eq}) depicted as $\ln(K_{\text{eq}})$ versus $1/T$, obtained for the sample 1-75%-SiO₂	74

Figure 26. Variable temperature $^{13}\text{C}\{^1\text{H}\}$ NMR spectra of a static sample of 1-75%-AC at the indicated temperatures. The top trace shows the CSA simulation of the signal at 183 K.....	76
Figure 27. Variable temperature ^2H NMR spectra of a static sample of 2-50%-AC recorded at the indicated temperatures.	77
Figure 28. Static ^2H NMR spectrum of 2-50%-AC at 263 K. The red line shows the simulation of the quadrupolar pattern with $C_Q = 97$ kHz and $\eta = 0.08$, the green line depicts the isotropic component.	79
Figure 29. Temperature dependence of the equilibrium constant K_{eq} depicted as $\ln(K_{\text{eq}})$ versus $1/T$, obtained from the samples 2-50%-AC (\square) and 2-130%-AC (\circ).	80
Figure 30. $^{13}\text{C}\{^1\text{H}\}$ MAS NMR spectrum of 2-130%-AC at a spinning speed of 9 kHz.....	81
Figure 31. Variable temperature ^2H NMR spectra collected for a static sample of 2-130%-AC at the indicated temperatures (bottom). Top spectrum: Room temperature ^2H MAS NMR of 2-130%-AC , spinning at a rate of 9 kHz.	83
Figure 32. ^{13}C MAS NMR of neat polycrystalline benzoic acid at a rotational speed of 3 kHz (top) and 4 kHz (middle), and ^{13}C NMR of a static sample of benzoic acid adsorbed on DARCO (bottom).....	103
Figure 33. ^{13}C MAS and static NMR of polycrystalline citric acid (top) and citric acid adsorbed on DARCO (bottom) in a sub-monolayer.	105
Figure 34. ^{13}C Wideline NMR of terephthalic acid adsorbed on DARCO [®]	105
Figure 35. Standard setup to test the uptake of a gas into a solid support.	106
Figure 36. ^{13}C MAS NMR of polycrystalline benzoic acid (top, 4 kHz), and a static sample of benzoic acid adsorbed on silica (150 Å average pore size, 0 kHz, bottom).....	108
Figure 37. ^{13}C Wideline NMR of terephthalic acid-modified DARCO [®] (top), benzoic acid- modified DARCO [®] (middle), and benzoic acid-modified silica (bottom) after treating the samples with triethylamine for 24 hours.	109
Figure 38. Adsorption capacities of several modified surfaces expressed in grams of triethylamine per gram of support.	112

Figure 39. Adsorption curves for several modified supports expressed as molar ratios of triethylamine versus modifier.....	113
Figure 40. Desorption curves for several modified surfaces, expressed in grams of triethylamine versus grams of support.....	113
Figure 41. Desorption curves for several modified surfaces, expressed in the molar ratios of triethylamine versus modifiers.	114
Figure 42. Phosphoric acid-modified Norit [®] pellets during the desorption experiment.	115
Figure 43. Prototype design for the air purification device used to remove VOCs from waste containers.	116
Figure 44. (A) Sealed showcase after dispersing proprietary colored VOC. (B) 15 seconds after activating the purification prototype. (C) 60 seconds after activating the prototype. (D) 120 seconds after activating the prototype. All color and scent had been removed from the showcase.....	117
Figure 45. ¹³ C Wideline solid-state NMR spectra of cyclododecane adsorbed on DARCO (top), and cyclododecane-modified DARCO [®] treated with ethyl acetate (bottom).	118
Figure 46. Adsorption curves for cyclododecane- and paraffin-modified DARCO [®] with ethyl acetate as the odor molecule.	119
Figure 47. Desorption curve of cyclododecane- and paraffin-modified DARCO [®] treated with ethyl acetate as a nonprotic and less polar scent molecule.	120
Figure 48. Reaction of nonyl aldehyde with di(hydroperoxy)propane adduct of triphenylphosphine oxide.....	120
Figure 49. ¹³ C NMR spectrum recorded after oxidation of nonyl aldehyde overnight in C ₆ D ₆ at room temperature.....	122
Figure 50. ¹ H NMR spectrum after oxidation of nonyl aldehyde overnight in C ₆ D ₆ at room temperature.....	122
Figure 51. ¹³ C NMR spectrum after the oxidation of nonyl aldehyde in 90 minutes at room temperature using one drop of H ₂ SO ₄ as an acid catalyst.	123
Figure 52. ¹ H NMR spectrum after the oxidation of nonyl aldehyde in 90 minutes at room temperature using one drop of H ₂ SO ₄ as an acid catalyst.	124

Figure 53. ^{31}P NMR spectrum of the oxidizer after exposure to the trash container for 4 days. The upfield resonance corresponds to triphenylphosphine, the downfield one to triphenylphosphine oxide from the spent Ahn oxidizer. 125

Figure 54. ^{31}P NMR of the extracted oxidizer and a test amount of triphenylphosphine oxide^{5b} after exposure to the lab atmosphere for 2 weeks..... 126

LIST OF TABLES

	Page
Table 1. Interactions in the solid state, their dependence on the external magnetic field B_0 , and maximal/typical values found for static samples.....	5
Table 2. The samples investigated were polycrystalline Ph_3PO (TPPO, 1) and 1 adsorbed on alumina with the indicated surface coverages.	30
Table 3. The temperature dependence of the rate constants, K_{exch} , obtained by lineshape analysis of the variable temperature static $^{31}\text{P}\{^1\text{H}\}$ NMR spectra of 4	39
Table 4. The dependence of the exchange constant K_{exch} obtained at 295 K on the % surface coverage of 1 on alumina.	41
Table 5. Dependence of the ^{31}P T_1 relaxation time on the temperature, obtained for a static sample of 4	43
Table 6. ^{13}C isotropic chemical shifts δ_{iso} and CSA parameters (CSA $\Delta\sigma$ and asymmetry parameter η) derived from the $^{13}\text{C}\{^1\text{H}\}$ MAS and static NMR experiments carried out for 1 , 1-75%-SiO₂ and 1-75%-AC	64
Table 7. Temperature dependence of the mole fractions found for isotropically moving molecules of 1 (P_{iso}) and surface-bound molecules (P_{bound}) in 1-75%-SiO₂ and the corresponding equilibrium constants K_{eq}	73
Table 8. Temperature dependent mole fractions of isotropically moving ferrocene molecules (P_{iso}) and surface-attached molecules (P_{bound}) and the corresponding equilibrium constants K_{eq} , determined for 2-50%-AC	78
Table 9. Temperature dependent mole fractions of isotropically moving ferrocene molecules (P_{iso}) and surface-attached molecules (P_{bound}) and the corresponding equilibrium constants K_{eq} , determined for 2-130%-AC	84
Table 10. Amounts of triethylamine odor molecules adsorbed per gram of DARCO [®] after exposure of the modified supports to vapors of the base for 24 hours...	107
Table 11. Amounts of triethylamine odor molecules adsorbed per gram of DARCO [®] after exposure of the modified supports to vapors of the base for 14 days. ...	111
Table 12. Reaction conditions for the conversion of nonyl aldehyde to nonanoic acid using the di(hydroperoxy)propane adduct of triphenylphosphine oxide.	121

CHAPTER I

INTRODUCTION

Overview

Solid-state nuclear magnet resonance (NMR) spectroscopy has become more mainstream across academia and industry. The modern techniques allow the analysis of a large variety of compounds and materials in the solid state. Classical applications are found in polymers, regardless whether they are of an organic, organic-inorganic hybrid, or organometallic nature. One can investigate the purity, tacticity and dynamics of polymers, and, for example, distinguish between crystalline and amorphous regions. Characteristics of solids in general, such as phase transitions or defects in the crystal lattice can also be studied conveniently by solid-state NMR. Furthermore, insights about structures and processes on surfaces can be gained, most importantly those of solid immobilized and heterogeneous catalysts, such as zeolites. All amorphous and insoluble substances, and compounds that would be destroyed upon solution (self-assembly materials, clathrates) can be investigated by solid-state NMR.

The bulk characteristics of substances in solution and in the solid state can be compared. For example, a coordination compound might display a different arrangement of ligands around the metal center in solution than in the solid state, when crystal packing forces are dominant. Often solid-state NMR provides the decisive clue about a disordered crystalline substance, so that a challenging X-ray structure can finally be solved with this additional piece of information because both methods are complementary. Finally, for the research discussed in this thesis it is important to know that even in the solid state dynamic

processes take place that can be analyzed with solid-state NMR. In host-guest assemblies, like substances adsorbed on the surface within pores of a support material, the adsorbate often displays several modes of mobility, including translational movements. Rotational processes of functional groups and substituents are also found in crystalline compounds. For example, a methyl group always rotates about the threefold $-\text{CH}_3$ axis at ambient temperature, while trimethylsilyl groups rotate about the threefold $-\text{SiMe}_3$ axis. The same is true for cyclopentadienyl (Cp) ligands in metallocenes that rotate about the fivefold metal-(Cp center) axis. This dissertation will focus on the use of different solid-state NMR spectroscopic techniques to study the molecular motions of triphenylphosphine oxide, ferrocene, and diverse volatile organic compounds adsorbed on the surfaces of silica, alumina and activated carbon.

The first portion of this work will cover the adsorption and mobility of triphenylphosphine oxide (**1**). Phosphine oxides represent a very important class of compounds.¹⁻⁷ They are often the byproducts of phosphine chemistry, for example, in the field of immobilized catalysts.² Phosphine oxides are also formed as stoichiometric co-products in the Wittig and Appel reactions. Furthermore, phosphine oxides can be used as probes to determine the acidity of a surface in oxide materials.³ In the first part of this dissertation different modes of mobility have been described and quantified for **1** on a neutral alumina surface.⁴

The second section will focus on the adsorption of ferrocene and ferrocene- d_2 on silica and activated carbon. Ferrocene is a classic metallocene notable for its use in catalysis. Previous work in the research group focused on describing the behavior of

different metallocenes on various supports.^{8,9} However, no attempts have been made so far at quantifying specific modes of mobility of ferrocene on support surfaces. Utilizing solid-state NMR allowed for a detailed description of the adsorption process of ferrocene on silica and activated carbon in addition to determining and quantifying the various modes of molecular motion involved.

The last chapter consists of a fundamental adsorption study of volatile organic compounds (VOCs) on activated carbon supports. Currently, activated carbon (AC) attracts great attention due to its broad range of applications in environmental chemistry, medicine and industry, for example, for gas and water purification, metal extraction, and many others.^{10,11} In spite of the importance of AC, a key understanding of the behavior of molecules adsorbed on its surface is still lacking. The main difficulty with activated carbon is not only the broad pore size distribution but also the large number of different local structures and various microenvironments. Although numerous thermochemical investigations have been carried out for simple organic molecules adsorbed on AC from vapors and solutions (benzene, toluene, ethyl chloride, carbon tetrachloride and many others),¹²⁻¹⁶ up to now there is only little knowledge about the molecular dynamics of adsorbed molecules and their interactions with the pore surfaces in AC.¹⁷ Furthermore, in collaboration with a local company, AC-based filter materials for odor control purposes have been developed.

Solid-State Nuclear Magnetic Resonance

A common theme recurring in all chapters of this dissertation are the anisotropic interactions that can be probed with solid-state NMR spectroscopy. All anisotropic interactions add up in the solid state, and they can be described in the form of their corresponding Hamiltonians.^{18,19}

$$\hat{H} = \hat{H}_Z + \hat{H}_Q + \hat{H}_D + \hat{H}_g + \hat{H}_{CS} + \hat{H}_J.$$

Hereby, only \hat{H}_Z , the Zeeman interaction, is isotropic and determined by the external magnetic field, the rest of the interactions, regarding their size and presence, is defined by the sample material itself. Typical/maximal values for H_z and the anisotropic interactions are given in Table 1. These values indicate how broad the signals can become in the solid-state NMR spectrum in case the interactions are present.

Anisotropy means that the interactions are not spherically symmetric. Therefore, these interactions are directional in space and manifest themselves in the solid state, because they are not averaged out by rapid random tumbling of the molecules like in solution. A crucial point in the following chapters will be that probing the anisotropic interactions under various conditions allows to determine mobilities in the solid state. For example, a reduction of the chemical shift anisotropy (CSA) and therewith the signal width when transitioning from polycrystalline to adsorbed substances indicates that a certain degree of reorientation of the molecules occurs on the surface. Using multinuclear and

variable-temperature solid-state NMR techniques then allows to disentangle different modes of mobility.

Table 1. Interactions in the solid state, their dependence on the external magnetic field B_0 , and maximal/typical values found for static samples.

\hat{H}_Z	Zeeman interaction	(splitting of spin energy levels in B_0)	$\sim B_0$	50 000 000 Hz (50 MHz)
\hat{H}_Q	Quadrupolar interactions	only for $I > 1/2$	1 st order H_Q independent of B_0 , 2 nd order $H_Q \sim 1/B_0$	5 000 000 Hz (5 MHz)
\hat{H}_D	Dipolar interactions	Direct Homo- and Hetero-nuclear couplings	independent of B_0	100 000 Hz (0.1 MHz)
\hat{H}_g	Interactions with electron spins	Paramagnetic samples	dependent on B_0 (complex)	100 000 Hz (100 kHz)
\hat{H}_{CS}	Chemical Shift interactions	Chemical Shift Anisotropy (CSA)	$\sim B_0$	20 000 Hz (20 kHz)
\hat{H}_J	Scalar Couplings	Indirect J couplings	independent of B_0	100 Hz

Magic Angle Spinning (MAS)

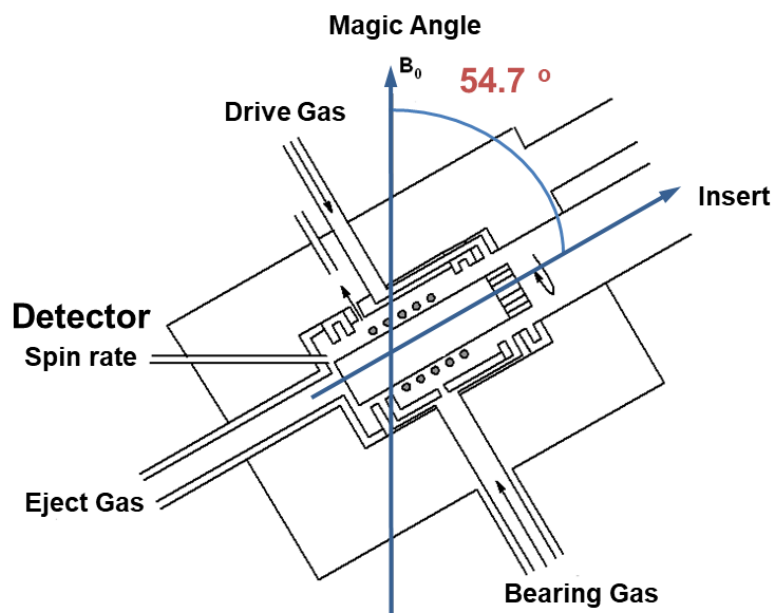


Figure 1. Depiction of the internal components of a solid-state probe and rotor.

In order to combat the anisotropic nature of interactions in solid-state NMR, specially designed probes are used that enable the rotation of a solid sample around the magic angle, 54.7° (Figure 1). In the case of chemical shift anisotropy, rotation about this angle simplifies the term $(3\cos^2\theta-1)$ to zero in the Hamiltonian of the CSA tensor in equation (1). This results in a spectrum that contains only the isotropic chemical shift; the resonance found in solution NMR, and rotational sidebands. This is particularly useful in order to gain more information from complex spectra that stem from several inequivalent nuclei.

$$(1) \quad \hat{H}_{\text{CSA}} = \underbrace{\gamma h \sigma_{\text{iso}} B_0 \hat{I}_z}_{\text{Isotropic chemical shift } (\delta_{\text{iso}})} + \gamma h B_0 \hat{I}_z \frac{1}{2} \left[(3 \cos^2 \theta - 1)(\sigma_{33} - \sigma_{\text{iso}}) + (\sin^2 \theta \cos^2 \psi (\sigma_{22} - \sigma_{11})) \right]_{\text{Rotational Sidebands}}$$

Chemical Shift Anisotropy (CSA)

As previously mentioned, the orientation of the molecule in space is important in the solid state and the chemical shift anisotropy (CSA) of a signal can be used to gauge the mobility of a molecule on a surface. For instance, the CSA of a pure powdered polycrystalline sample of triphenyl phosphine has a large ^{31}P CSA that spans ~60 ppm (Bottom, Figure 2). Even when magic angle spinning (MAS) is applied with a 4 kHz rotational speed, distinct sidebands are seen, indicating a residual CSA (Top, Figure 2).

This scenario changes upon solvent-free adsorption of a sub-monolayer of triphenylphosphine on silica. Even with no rotation, a single isotropic resonance is seen corresponding to the same resonance in solution NMR (Figure 3). Although this resonance is quite broad, it is important to note that MAS does not generate rotational sidebands and merely further decreases the residual linewidth of the signal indicating a solution-like reorientation of the triphenylphosphine molecules on the surface of silica.

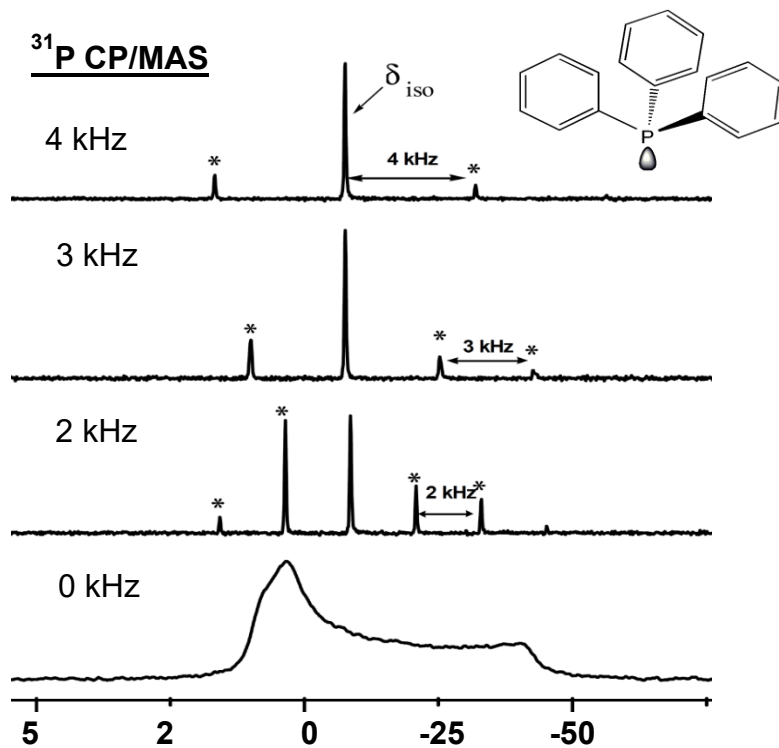


Figure 2. ³¹P CP/MAS spectra of polycrystalline triphenylphosphine at different rotational speeds.²⁰

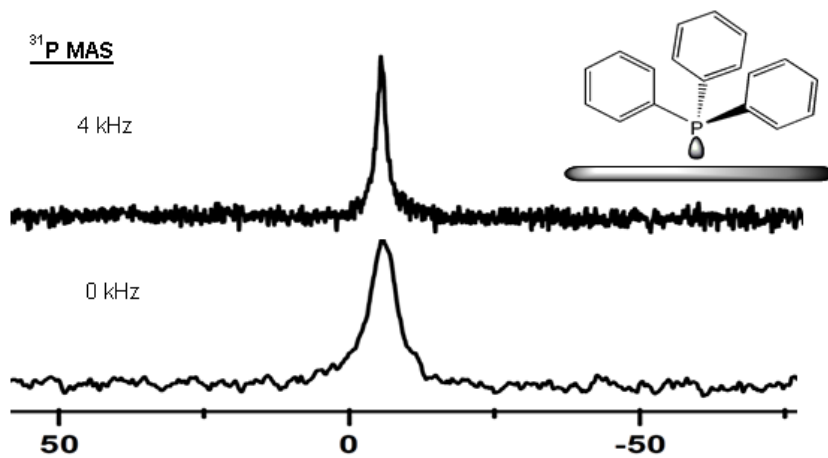


Figure 3. ³¹P MAS spectra of triphenylphosphine adsorbed on silica.²⁰

Quadrupolar Interactions

About 70 % of all nuclei possess a nuclear spin, I , that is greater than $1/2$ and are therefore quadrupolar nuclei. The electric quadrupole moment Q stems from an unsymmetric distribution of charge within the nuclei. Thus, the nuclei are not spherically symmetric anymore and there are two potential cases.

In the first case the nucleus is longer in the direction of its nuclear spin angular momentum, giving it a cigar-like shape. This sort of nucleus is known as prolate and Q is greater than zero. In the second scenario the nucleus bulges near its equator like the earth and is known as oblate. In this situation Q is less than zero.

In solution NMR fast isotropic tumbling and reorientation of the molecules typically averages out the quadrupolar interactions. The half width in solution, $\nu_{1/2}$, is given in equation (2).¹⁸

$$(2) \Delta\nu_{1/2} = 3/10 \cdot \pi \cdot (2I+3)/[I^2(2I-1)] \cdot (e^2Qq/h)^2 \cdot \tau_c$$

Here τ_c is the correlation time, q the electric field gradient, and (e^2Qq/h) is the quadrupolar coupling constant, Q_C .

From this equation it follows that the quadrupolar coupling constant can be obtained from measuring the halfwidth of a signal. The lines can be made narrower by reducing the correlation time, or in other words making the molecules in solution more mobile. For this purpose, the solvent should be as non-viscous as possible, the solution dilute, and the temperature as high as possible. The smaller the molecule, the smaller the

correlation time, and thus the smaller the halfwidth will be. This is why ^{14}N is often a favorable nucleus for measuring small organic and organometallic molecules, while in proteins or soluble polymers it is not competitive to the spin-1/2 nucleus ^{15}N .

Though quadrupolar interactions are mostly cancelled out by the rapid tumbling of the molecules in solution, in the solid state they can be prominent. First order quadrupolar interactions result when the quadrupolar coupling constant is relatively small as compared to the Zeeman interaction. If there are only first order quadrupolar interactions, the signal shapes are simple, predictable, and easy to interpret and simulate. However, in the case of second order quadrupolar interactions the quadrupolar coupling can lead to very complicated and unpredictable spectra.

Deuterium is an easy to measure quadrupolar nucleus with mostly first order quadrupolar interactions and a spin of 1. These features render it an excellent candidate for solid-state NMR studies. A typical Pake pattern is shown in the deuterium spectrum of $\text{Cp}_2\text{Fe-d}_2$ in Figure 4.

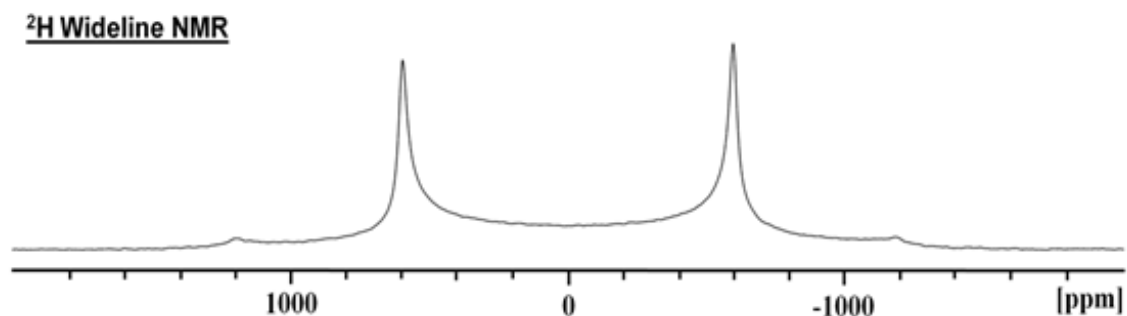


Figure 4. ^2H Wideline spectrum of $\text{Cp}_2\text{Fe-d}_2$.

From this spectrum the quadrupolar coupling constant can be derived using equation (3)¹⁸ based on the distance between the two inner peaks $\Delta\nu_i$ in Hz. Furthermore, the isotropic chemical shift for the deuterium Pake patterns is found at the center of the signal. Therefore, from the Pake pattern one can obtain δ_{iso} , as well as the characteristic quadrupolar coupling constant Q_c .

$$(3) \Delta\nu_i = 3/4 (e^2qQ/h)$$

Surface Coverage and Adsorbates

Another common theme in all chapters of this dissertation is determining the maximal amount of adsorbed compound that can be accommodated by a given surface. This question can be addressed in several ways. However, it is most straightforward to rationalize the footprint of an adsorbed compound as a 2D projection of the adsorbent on a planar surface, as depicted for **1** (Figure 5).

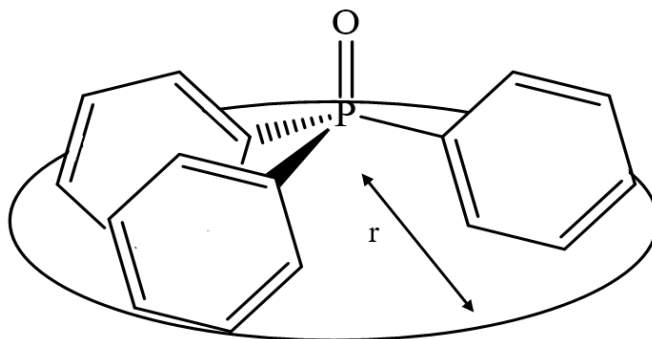


Figure 5. 2D Projection of **1** used to calculate its footprint on an idealized surface.

This view of the adsorbate allows the determination of the surface area occupied by each molecule based on the radius attained from a molecule's crystal structure. The footprint can then be used together with the known specific surface area of a support material to estimate the maximal monolayer surface coverage. In combination with the weight of adsorbed substance on one gram of support, the actual scenario can be derived. Three types of surface coverages that are often applied and found in the research presented in this thesis, namely a double layer, a monolayer, and sub-monolayer surface coverage, are depicted schematically in Figure 6.

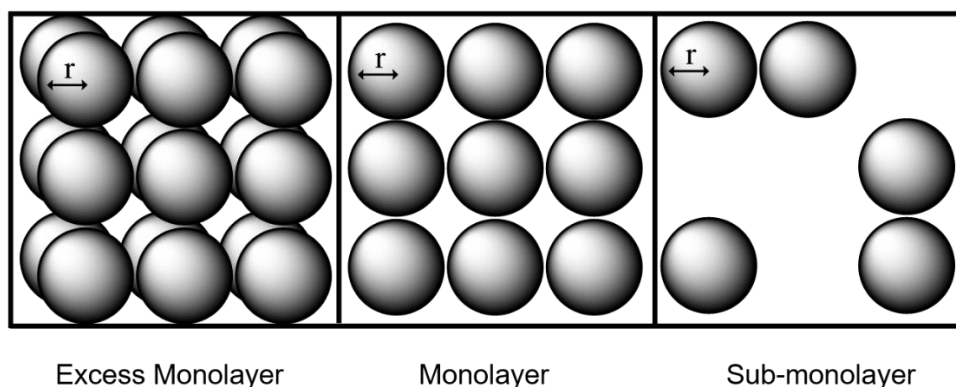


Figure 6. Three possible loadings of molecules on a surface.

Phosphine Oxides

Phosphine oxides are important synthetic targets and intermediates.^{7c,7d,21,22} For example, they are used for Mitsunobu reactions,^{22g} and recently attracted attention as redox-free Mitsunobu organocatalysts.^{22h} Phosphine oxides are also co-products of Wittig and Appel reactions and unwanted byproducts of phosphine chemistry, especially in the

field of catalysts immobilized via phosphine linkers.^{2c,23,24} They are applied to probe surface acidities²⁵ and receive attention in the decomposition of warfare agents.²⁶ One of the most important features of phosphine oxides is their unique ability to form hydrogen bonds with a variety of different donors. For example, phenols are used in combination with phosphine oxides to create extended hydrogen-bonded networks,³⁰⁻³² and hydrogen bonding with naphthol,³² sulfonic acids,³³ and water has been reported.^{29,34-36} Silanols and even chloroform crystallize as hydrogen-bonded assemblies.³⁷ Besides single crystal X-ray diffraction, ³¹P solid-state NMR spectroscopy is a powerful method to analyze the hydrogen bonding characteristics of diverse P(V) species.^{27-29,37,38}

Combining the unique potential of phosphine oxides to form hydrogen bonds with the quest for superior oxidizing agents, new types of stabilized peroxides^{35,36,39-42} that are solid, soluble in organic solvents, and exhibit well-defined structure and composition have been explored in a parallel project in the Blumel group. Chapter IV of this dissertation will describe the use of one such stabilized peroxide in air purification, $\text{Ph}_3\text{PO}(\text{HOO})_2\text{CMe}_2$,³⁹⁻⁴² adsorbed on activated carbon.

From an analytical point of view, phosphine oxides display interesting mobilities on surfaces, that have been studied by solid-state NMR.²⁷⁻²⁹ In the presented dissertation these preliminary studies are refined, and quantitative information is obtained, as outlined in chapter II. Using alumina as a different and new support, the general nature of the dry adsorption and mobility of the phosphine oxides on diverse surfaces is probed.

Ferrocene

Ferrocene was the first organometallic complex with a sandwich-type structure featuring η^5 -coordination of both cyclopentadienyl rings.⁴³ It has been characterized by single crystal X-ray diffraction in 1951. Geoffrey Wilkinson and Ernst Otto Fischer shared the 1973 Nobel Prize in Chemistry for this discovery. Ferrocene can easily be modified by deprotonation⁴⁴ and transformed into ferrocene-*d*₂ that renders it amenable to ²H NMR spectroscopy. Deuterated ferrocene will be applied to ²H solid-state NMR studies in Chapter III of this dissertation. After deprotonation, reaction with chlorophosphines yields bisphosphine ligands with a rigid backbone that find ample use, for example, in catalysis.⁴⁴ Furthermore, chiral ferrocene-modified silica gel has been applied as stationary phase in liquid chromatography.⁴⁵

The Bluemel group discovered recently that metallocenes of the type Cp₂M (Cp = cyclopentadienyl, C₅H₅) can be adsorbed on silica by dry grinding of the components in the absence of solvents.⁴⁶⁻⁴⁸ However, some of the metallocenes, like vanadocene or chromocene react quickly after the adsorption step and enter the field of organometallic surface chemistry. By reacting with a silica or alumina surface, chromocene forms the important heterogeneous Union Carbide catalyst that is used industrially for olefin polymerization under mild conditions in the absence of a co-catalyst.^{49,51} Despite the importance and large-scale application of the Union Carbide catalyst, its structure on oxide surfaces remains largely unknown. The commonly accepted partial structure of the catalytically active surface species consists of a CpCr(III) moiety that must be bound to a

surface siloxide anion, as determined mostly by solid-state NMR,⁴⁸ and XPS and IR studies.^{50,51}

In our quest to elucidate the complete structure of the surface-bound chromium species, chromocene has been dry-ground with silica in the absence of a solvent that could influence the outcome of the surface reaction. However, it turned out that even without solvent the subsequent reaction was too fast to allow for sufficient time to study the initial elementary steps by solid-state NMR or other methods. Therefore, we turned to the less reactive ferrocene that persists under inert gas for months as a metallocene with the same structure as chromocene. By obtaining a deeper insight about the dynamic processes of the adsorption of ferrocene on different surfaces, conclusions about the structurally practically identical chromocene should be possible. Especially the orientation of the ferrocene towards the surface is crucial, since the reaction, for example, with surface silanol groups can only take place after contact with the metal center, but not through the Cp ring. In other words, any, albeit temporary, sideways orientation of a metallocene should facilitate the necessary interaction of the metal with the surface. Even for adsorbed ferrocene, when oxygen is admitted, the color changes to blue and ferrocenium salts are generated at surface silanol sites,^{23e} and therefore, it can be anticipated that there must be a sideways orientation of ferrocene at some point. While there is no chemical reaction taking place when ferrocene or chromocene are adsorbed on activated carbon surfaces, comparing data from different surfaces allows for a complete quantitative analysis of the adsorption process by solid-state NMR spectroscopy, as outlined in Chapter III of this dissertation.

Volatile Organic Compounds (VOCs)

Volatile organic compounds (VOCs) are a class of organic compounds that have a high vapor pressure even at room temperature. Volatility is a measure of how easily a compound vaporizes. A common misconception is that all VOCs are liquids. However, even solids like benzoic acid have a high vapor pressure at room temperature and can be considered a VOC.

In the year 2012, the World Health Organization (WHO) estimated that air pollution was responsible for more than seven million deaths.⁵² Street vendors in Bangkok, Thailand, reported issues with their noses, throats, and lungs.⁵³ Additionally, flight crews for aircraft are exposed to numerous VOCs on a daily basis that can have significant negative health effects.⁵⁴ There is even interest in the real time assessment of VOCs in households.⁵⁵ These examples are just a small set of health issues associated with VOCs today.

Given the toxic nature of VOCs there is a plethora of research involving the remediation of these compounds in the environment. The three major materials used in the adsorption of VOCs are activated carbon, zeolites, and hypercrosslinked polymeric resins.⁵⁶ In specific activated carbon has received significant attention for its ability to adsorb VOCs due to its large surface area per gram and simplicity to modify for target adsorption.⁵⁶⁻⁶⁰

In collaboration with a waste management company we sought to utilize and apply our knowledge of adsorption in order to design a new air purification system for the removal of noxious VOCs in waste receptacles. In parallel a new air purification system

was designed, and new modified activated carbon materials were tested for their ability to adsorb/retain VOCs over an extended period of time.

Silica and Alumina as Support Materials

Heterogeneous catalysis makes use of all sorts of inorganic oxides and ceramic materials. Silica and Alumina are used extensively in the Blumel group because they are the most favorable supports for immobilized homogeneous catalysts,^{23,61} and adsorbates.^{1,2,5,6,37,46-48} As compared to polymers, for example, silica and alumina have many advantages.⁶⁵ Most importantly, in organic solvents these oxides are chemically and thermally inert, and they are available as neutral materials. They are mechanically stable and robust and can be stirred with a stirring bar in a Schlenk flask for days without being broken down into smaller particles. This is important with respect to separating and reusing the support with the bound catalyst after the reaction by letting it settle and decanting the supernatant. The particle size distribution most favorable for this purpose is 0.063-0.200 mm, corresponding to large grains that settle within five minutes from organic solvents. This large particle size also allows for easy handling of the materials in a nitrogen stream or a glove box, and filling rotors for solid-state analysis poses no problem, as compared to powders of small particles like aerosil that are hard to contain. Suppliers also offer a large variety of well-defined silica and alumina with different pore sizes and specific surface areas. Regarding the pore sizes, it is important that they are large enough to allow for catalysts, substrates, and adsorbates to enter and exit without noteworthy diffusion delays. Since the most powerful method applied in the study of this thesis is the

moderately sensitive solid-state NMR,^{18,19,23,62,63} it is indispensable to have the largest possible specific surface area that allows for maximal loading with catalyst or adsorbate and minimal bulk. Silica with an average pore size of 40 Å and a specific surface area of 750 m²/g has proven to be the optimal choice over decades of research in the Blumel group and was therefore chosen as one of the ferrocene adsorbents (Chapter III). The alumina selected for adsorbing phosphine oxides (Chapter II) has an average pore diameter of 90 Å and a specific surface area of 100 m²/g. The characteristics of the surfaces regarding acidity and moisture content can easily be controlled. Typically, to create reproducible surface qualities, oxides are dried at 300 °C for four days to remove adsorbed water and condense adjacent OH groups. Activated carbon does not readily take up moisture and can be used as obtained. Importantly, for the adsorption studies presented here, different supports were desirable to investigate whether the observed dynamic phenomena of adsorbed species were universal in nature, or only limited to one specific silica surface.

It should be pointed out that other popular porous materials are simply not viable for adsorbing ferrocene or phosphine oxides. Zeolites or metal organic frameworks (MOFs) have too small pore sizes, and the latter does not have a contiguous surface area, as it is needed for the adsorbate-adsorbent interactions and surface mobility. Additionally, for industrial collaborations the fact that alumina, silica, and activated carbon are inexpensive and environmentally benign, in contrast to MOFs, comes to the foreground.

Conclusion

In conclusion, the work presented in this dissertation has greatly expanded the general understanding of adsorption processes that take place in the absence of solvents. It has been demonstrated that dry adsorption of phosphine oxides and ferrocene does not only take place on one specific oxide support, silica, but occurs also when the vastly different surfaces of alumina and activated carbon are offered. In the case of adsorbed ferrocene, a subsequent reaction with surface silanol groups to form ferrocenium ions could be explained by its orientation towards the surface. The similarity of the obtained adsorption data for such different species as phosphine oxides and ferrocene on the diverse supports: silica, alumina, and activated carbon; suggests that dry adsorption is more generally viable than previously thought. Beyond being a mere curiosity, a first impactful application of dry adsorption for producing porous surface-modified air purification materials has been described in this dissertation.

References

1. C. R. Hilliard, N. Bhuvanesh, J. A. Gladysz, J. Blümel, *Dalton Trans.* **2012**, *41*, 1742.
2. **(a)** J. Blümel, *Coord. Chem. Rev.* **2008**, *252*, 2410-2423. **(b)** J. Guenther, J. Reibenspies, J. Blümel, *Adv. Synth. Catal.* **2011**, *353*, 443-460. **(c)** R. Silbernagel, A. Diaz, E. Steffensmeier, A. Clearfield, J. Blümel, *J. Mol. Catal. A* **2014**, *394*, 217-223. **(d)** C. Merckle, J. Blümel, *Adv. Synth. Catal.* **2003**, *345*, 584-588. **(e)** C. Merckle, J. Blümel, *Top. Catal.* **2005**, *34*, 5-15. **(f)** J. C. Pope, T. Posset, N. Bhuvanesh, J. Blümel, *Organometallics* **2014**, *33*, 6750-6753. **(g)** T. Posset, J. Blümel, *J. Am. Chem. Soc.* **2006**, *128*, 8394-8395. **(h)** T. Posset, J. Guenther, J. Pope, T. Oeser, J. Blümel, *Chem. Commun.* **2011**, *47*, 2059-2061. **(i)** K. J. Cluff, N. Bhuvanesh, J. Blümel, *Chem. Eur. J.* **2015**, *21*, 10138-10148. **(j)** J. H. Baker, N. Bhuvanesh, J. Blümel, *J. Organomet. Chem.* **2017**, *847*, 193-203.

3. R. Yerushalmi, J. C. Ho, Z. Fan, A. Javey, *Angew. Chem. Int. Ed.* **2008**, *47*, 4440.
4. (a) A. R. Wilmsmeyer, W. O. Gordon, E. D. Davis, B. A. Mantooth, T. A. Lalain, J. R. Morris, *Rev. Sci. Instrum.* **2014**, *85*, 014101. (b) J. Kemsley, *Chem. Eng. News* **2014**, *92*, 29.
5. S. Kharel, T. Jia, N. Bhuvanesh, J. H. Reibenspies, J. Blümel, J. A. Gladysz, *Chem. Asian J.* **2018**, *13*, 2632-2640.
6. C. R. Hilliard, S. Kharel, K. J. Cluff, N. Bhuvanesh, J. A. Gladysz, J. Blümel, *Chem. Eur. J.* **2014**, *20*, 17292-17295.
7. (a) T. Kovacs, G. Keglevich, *Curr. Org. Chem.* **2017**, *21*, 569-585. (b) D. Herault, D. H. Nguyen, D. Nuel, G. Buono, *Chem. Soc. Rev.* **2015**, *44*, 2508-2528. (c) M. D. Fletcher, *Organophosphorus Reagents*, **2004**, 171-214. (d) H. R. Hays, D. J. Peterson, *Org. Phosphorus Compounds*, **1972**, *3*, 341-500. (e) H. Adams, R. C. Collins, S. Jones, C. J. A. Warner, *Org. Lett.* **2011**, *13*, 6576-6579.
8. K. J. Cluff, J. Blümel, *Organometallics* **2016**, *35*, 3939-3948.
9. K. J. Cluff, M. Schnellbach, C. R. Hilliard, J. Blümel *J. Organomet. Chem.* **2013**, *744*, 119-124.
10. H. Marsh, F. Rodriguez-Reinoso, *Activated Carbon* (Oxford: Elsevier), **2006**.
11. S. Bubanale, Shivashankar, M. History, *Intern. J. Engin. Research & Technol.* **2017**, *6*, 495-497.
12. N. Wibowo, L. Setyadi, D. Wibowo, J. Setiawan, S. Ismadji, *J. Hazard. Materials* **2007**, *146*, 237-242.
13. M. M. Dubinin, N. S. Polyakov, L. I. Kataeva, *Carbon* **1991**, *29*, 481-488.

14. H. L. Chiang, C. P. Huang, P. C. Chiang, *Chemosphere* **2002**, *46*, 143-152
15. H. Hindarso, S. Ismadji, F. Wicaksana, N. Mudjijati, H. Indraswati, *J. Chem. Eng. Data* **2001**, *46*, 788–791.
16. M. C. Basso, A. L. Cukierman, D. Arundo, *Chem. Res.* **2005**, *44*, 2091–2100.
17. Y. Xu, T. Watermann, H.-H. Limbach, T. Gutmann, D. Sebastianib, G. Buntkowsky, *Chem. Phys.* **2014**, *16*, 9327- 9336.
18. C. A. Fyfe, C.F.C. Press, Guelph, Canada, **1983**.
19. T. M. Duncan, T. M. Farragut, Press: Chicago, IL, **1990**.
20. Y. Yang, Dissertation, University of Heildelberg, **2007**.
21. S. Kharel, T. Jia, N. Bhuvanesh, J. H. Reibenspies, J. Blümel, J. A. Gladysz, *Chem. Asian J.* **2018**, *13*, 2632-2640.
22. (a) J. Chrzanowski, D. Krasowska, J. Drabowicz, *Heteroatom Chem.* **2018**, *29*, e21476. (b) T. Kovacs, G. Keglevich, *Curr. Org. Chem.* **2017**, *21*, 569-585. (c) D. Herault, D. H. Nguyen, D. Nuel, G. Buono, *Chem. Soc. Rev.* **2015**, *44*, 2508-2528. (d) M. D. Fletcher, *Organophosphorus Reagents*, **2004**, 171-214. (e) H. R. Hays, D. J. Peterson, *Org. Phosphorus Compounds*, **1972**, *3*, 341-500. (f) H. Adams, R. C. Collins, S. Jones, C. J. A. Warner, *Org. Lett.* **2011**, *13*, 6576-6579. (g) K. C. K. Swamy, N. N. B. Kumar, E. Balaraman, K. V. P. P. Kumar, *Chem. Rev.* **2009**, *109*, 2551-2651. (h) R. H. Beddoe, K. G. Andrews, V. Magne, J. D. Cuthbertson, J. Saska, A. L. Shannon-Little, S. E. Shanahan, H. F. Sneddon, R. M. Denton, *Science* **2020**, *365*, 910-914. (i) D. W. Stephan, *Science* **2016**, *354*, 1248. (j) J. M. Bayne, D. W. Stephan, *Chem. Soc. Rev.* **2016**, *45*, 765-774. (k) X. Cai, S. Majumdar, G. C. Fortman, L. M. Frutos, M. Temprado, C. R. Clough, C. C. Cummins, M. E. Germain, T. Palluccio, E. V. Rybak-Akimova, B. Captain, C. D. Hoff, *Inorg. Chem.* **2011**, *50*, 9620-9630.
23. Selected references: (a) J. Blümel, *Coord. Chem. Rev.* **2008**, *252*, 2410-2423. (b) J. Guenther, J. Reibenspies, J. Blümel, *Adv. Synth. Catal.* **2011**, *353*, 443-460. (c) R. Silbernagel, A. Diaz, E. Steffensmeier, A. Clearfield, J. Blümel, *J. Mol. Catal. A*, **2014**, *394*, 217-223. (d) J. H. Baker, N. Bhuvanesh, J. Blümel, *J. Organomet. Chem.* **2017**, *847*, 193-203. (e) J. C. Pope, T. Posset, N. Bhuvanesh, J. Blümel, *Organometallics* **2014**, *33*, 6750-6753. (f) T. Posset, J. Guenther, J. Pope, T. Oeser, J. Blümel, *Chem.*

Commun. **2011**, *47*, 2059-2061. (g) K. J. Cluff, N. Bhuvanesh, J. Blümel, *Chem. Eur. J.* **2015**, *21*, 10138-10148.

24. J. Guenther, J. Reibenspies, J. Blümel, *Mol. Catal.* **2019**, *479*, 110629.
25. (a) A. Zheng, S.-B. Liu, F. Deng, *Chem. Rev.* **2017**, *117*, 12475–12531. (b) R. Yerushalmi, J. C. Ho, Z. Fan, A. Javey, *Angew. Chem. Int. Ed.* **2008**, *47*, 4440-4442. (c) J. P. Osegovic, R. S. Drago, *J. Phys. Chem. B*, **2000**, *104*, 147-154. (d) S. Hayashi, K. Jimura, N. Kojima, *Bull. Chem. Soc. Jpn.* **2014**, *87*, 69-75. (e) S. Machida, M. Sohmiya, Y. Ide, Y. Sugahara, *Langmuir* **2018**, *34*, 12694–12701.
26. (a) A. R. Wilmsmeyer, W. O. Gordon, E. D. Davis, B. A. Mantooth, T. A. Lalain, J. R. Morris, *Rev. Sci. Instrum.* **2014**, *85*, 014101. (b) J. Kemsley, *Chem. Eng. News* **2014**, *92*, 29-30.
27. P. J. Hubbard, J. W. Benzie, V. I. Bakhmutov, J. Blümel, *J. Chem. Phys.* **2020**, *152*, 054718.
28. S. Kharel, K. J. Cluff, N. Bhuvanesh, J. A. Gladysz, J. Blümel, *Chem. Asian J.* **2019**, *14*, 2704-2711.
29. C. R. Hilliard, S. Kharel, K. J. Cluff, N. Bhuvanesh, J. A. Gladysz, J. Blümel, *Chem. Eur. J.* **2014**, *20*, 17292-17295.
30. (a) A. E. Stross, G. Iadevaia, C. A. Hunter, *Chem. Sci.* **2016**, *7*, 94-101. (b) G. Iadevaia, A. E. Stross, A. Neumann, C. A. Hunter, *Chem. Sci.* **2016**, *7*, 1760-1767. (c) R. Cuypers, E. J. R. Sudhölter, H. Zuilhof, *Chem. Phys. Chem.* **2010**, *11*, 2230-2240.
31. D. Nunez-Villanueva, C. A. Hunter, *Chem. Sci.* **2017**, *8*, 206-213.
32. N. A. Bewick, A. Arendt, Y. Li, S. Szafert, T. Lis, K. A. Wheeler, J. Young, R. Dembinski, *Curr. Org. Chem.* **2015**, *19*, 469-474.
33. S. J. Pike, C. A. Hunter, *Org. Biomol. Chem.* **2017**, *15*, 9603-9610.

34. N. J. Burke, A. D. Burrows, M. F. Mahon, J. E. Warren, *Inorg. Chim. Acta* **2006**, *359*, 3497-3506.
35. R. Joshi, S. P. Pasilis, *J. Mol. Liquids* **2015**, *209*, 381-386.
36. F. F. Arp, N. Bhuvanesh, J. Blümel, *Dalton Trans.* **2019**, *48*, 14312-14325.
37. S. Kharel, N. Bhuvanesh, J. A. Gladysz, J. Blümel, *Inorg. Chim. Acta* **2019**, *490*, 215-219.
38. (a) E. Y. Tupikina, M. Bodensteiner, P. M. Tolstoy, G. S. Denisov, I. G. Shenderovich, *J. Phys. Chem. C* **2018**, *122*, 1711-1720. (b) G. Begimova, E. Y. Tupikina, V. K. Yu, G. S. Denisov, M. Bodensteiner, I. G. Shenderovich, *J. Phys. Chem. C* **2016**, *120*, 8717-8729.
39. F. F. Arp, S. H. Ahn, N. Bhuvanesh, J. Blümel, *New J. Chem.* **2019**, *43*, 17174-17181.
40. S. H. Ahn, K. J. Cluff, N. Bhuvanesh, J. Blümel, *Angew. Chem.* **2015**, *127*, 13539-13543.
41. S. H. Ahn, N. Bhuvanesh, J. Blümel, *Chem. Eur. J.* **2017**, *23*, 16998-17009.
42. S. H. Ahn, D. Lindhardt, N. Bhuvanesh, J. Blümel, *ACS Sustainable Chem. Eng.* **2018**, *6*, 6829-6840.
43. R. Peters, D. F. Fischer, S. Jautze, *Top. Organomet. Chem.* **2011**, *33*, 139-175.
44. A. Fihri, P. Meunier, J.-C. Hierso, *Coord. Chem. Rev.* **2007**, *251*, 2017-2055.
45. L. Qiao, X. Zhou, X. Li, W. Du, A. Yu, S. Zhang, W. Wu, *Talanta* **2017**, *163*, 94-101.

46. K. J. Cluff, M. Schnellbach, C. R. Hilliard, J. Blümel, *J. Organomet. Chem.* **2013**, *744*, 119-124.
47. K. J. Cluff, J. Blümel, *Organometallics* **2016**, *35*, 3939-3948.
48. K. J. Cluff, J. Blümel, *Chem. Eur. J.* **2016**, *22*, 16562-16575.
49. M. Schnellbach, J. Blümel, F. H. Köhler, *J. Organomet. Chem.* **1996**, *520*, 227-230.
50. W. P. McKenna, S. Bandyopadhyay, E. M. Eyring, *Applied Spectrosc.* **1984**, *38*, 834-837.
51. F. J. Karol, G. L. Karapinka, C. Wu, A. W. Dow, R. N. Johnson, W. L. Carrick, *J. Polym. Sci. A1* **1972**, *10*, 2621.
52. P. M. Mannucci, M. Franchini, *Int. J. Environ. Res. Public Health* **2017**, *14*, 1048.
53. P. Kongtip, W. Thongsuk, W. Yoosook, S. Chantanakul, *Atmos. Environ.* **2006**, *40*, 7138-7145.
54. Y. Otsuka, Y. Mizohata, A. Kobayashi, S. Okubo, T. Nakadate, *The Showa Univ. J. of Med. Sci.* **2017**, *29*, 231-240.
55. P. Harb, N. Locoge, F. Thevenet, *Chem. Eng. J.* **2020**, *380*, 122525.
56. X. Li, L. Zhang, Z. Yang, P. Wang, Y. Yan, J. Ran, *Sep. Purif. Technol.* **2020**, *235*, 116213.
57. K. Vikrant, K.-H. Kim, W. Peng, S. Ge, Y. Sik Ok, *Chem. Eng. J.* **2020**, *387*, 123943.
58. L. Ma, M. He, P. Fu, X. Jiang, W. Lv, Y. Huang, Y. Liu, H. Wang, *Sep. Purif. Technol.* **2020**, *235*, 116146.

59. W. Qiu, K. Dou, Y. Zhou, H. Huang, Y. Chen, H. Lu, *Chin. J. Chem. Eng.* **2018**, *26*, 81-88.
60. G. Wang, B. Dou, Z. Zhang, J. Wang, H. Liu, Z. Hao, *J. Environ. Sci.* **2015**, *30*, 65-73.
61. a) P. Barbaro, F. Liguori, Eds., *Heterogenized Homogeneous Catalysts for Fine Chemicals Production*, Springer: Heidelberg, 2010. b) F. R. Hartley, *Supported Metal Complexes*; Reidel, D. Publ. Co.: Dordrecht, The Netherlands, 1985. c) D. E. DeVos, I. F. J. Vankelecom, P. A. Jacobs, Eds., *Chiral Catalyst Immobilization and Recycling*; Wiley-VCH: Weinheim, 2000. d) G. Rothenberg, *Catalysis: Concepts and Green Applications*; Wiley-VCH, Weinheim, 2008.
62. C. Merckle, J. Blümel, *Chem. Mater.* **2001**, *13*, 3617-3623.
63. (a) A. T. Bell, *NMR Techniques in Catalysis*. Taylor & Francis: 1994. (b) S. Reinhard, J. Blümel, *Magn. Reson. Chem.* **2003**, *41*, 406-416.

CHAPTER II

ADSORPTION OF TRIPHENYLPHOSPHINE OXIDE ON ALUMINA*

Introduction

Adsorbed species are typically generated by applying liquids or gases to surfaces in a first step.¹ Investigations of solid/solid adsorption processes using neat solid adsorbates and solid adsorbents in the absence of a solvent remain rare. The first examples studied by solid-state NMR were described by Günther using polycyclic aromatic hydrocarbons (PAH).^{2,3} Subsequently, the concept of solid/solid adsorption could be extended to metallocenes which sparked interest as precursors for catalysts such as the Union Carbide Catalyst (Chromocene on silica or alumina).⁴ Early research in our group resulted in a study of paramagnetic chromocenes in polycrystalline and adsorbed form,^{5,6} while Oprunenko and Günther investigated biphenylene chromium tricarbonyl complexes.⁷ Later we studied diverse diamagnetic and paramagnetic metallocenes and demonstrated that they can be adsorbed as solids on amorphous high surface area silica gel⁸⁻¹¹ and on various carbon supports.¹²

In all the cases of successful solid/solid adsorption described,²⁻¹² unique solid-state NMR¹³⁻¹⁶ features were found due to the mobilities of the adsorbate molecules on the surfaces. The anisotropic interactions dominating the signal shapes of crystalline solids,³⁻¹⁶ dipolar and quadrupolar interactions,^{13,14} as well as the Chemical Shift Anisotropy

*Reproduced with permission from “Disentangling Different Modes of Mobility for Triphenylphosphine Oxide Adsorbed on Alumina”, P. J. Hubbard, J. W. Benzie, V. I. Bakhmutov, J. Blümel, *J. Chem. Phys.* **2020**, *152*, 054718. Copyright AIP Publishing LLC.

(CSA)^{13,14} of the signals of the adsorbed species, are averaged out. Signals with a larger residual linewidth, but devoid of rotational sidebands, resulted. The broader isotropic lines have been interpreted as a consequence of the heterogeneous surroundings of the nuclei on the support surfaces, versus their environment in a single crystal.

Recently, we could show qualitatively that various solid aryl- and alkyl phosphine oxides with high melting points can also be adsorbed on silica surfaces in the absence of solvents.^{17,18} However, many questions still remain to be answered, especially with respect to the interactions of the phosphine oxides with the support. While for PAH and metallocenes, van der Waals interactions are most likely responsible for the interactions of the adsorbates with the support surfaces; for phosphine oxides hydrogen bonding additionally plays a role. It has, for example, been shown by single crystal X-ray diffraction that silanols,^{18,20} phenols,²⁰⁻²² naphthol,²³ sulfonic acids,²⁴ and even chloroform²⁰ form hydrogen-bonded adducts with phosphine oxides. We also discovered that phosphine oxides possess the unique ability to stabilize hydrogen peroxide and di(hydroperoxy)alkanes by forming strong hydrogen bonds.^{19,25-29} Furthermore, the influence of hydrogen bonding on the ³¹P solid-state NMR spectra of oxidic P(V) species has been analyzed in detail.³⁰

In this chapter, we present new results that detail the different modes of mobility that triphenylphosphine oxide (TPPO, **1**), in polycrystalline form, and adsorbed in submonolayers on alumina surfaces, can undergo. Phosphine oxide **1** has been chosen because it is not hygroscopic, in contrast to some alkylphosphine oxides,¹⁹ and its monofunctional nature avoids complications that can be encountered in the presence of a

second intramolecular PO group.¹⁸ Alumina finds a broad variety of applications in daily life and academia. In the laboratory, for example, it is used as a catalyst in organic synthesis, and as the stationary phase for chromatography. In combination with solid-state NMR spectroscopy alumina is rather neglected because of its heterogeneous nature.³⁹

Results and Discussion

It has been established previously that triphenylphosphine oxide (TPPO, **1**) can be adsorbed on silica surfaces by dry grinding without any solvent.^{17,18} The interaction of **1** with the silica surface was determined to be propagated by hydrogen bonding with surface silanol groups.^{17,20} Most importantly, when adsorbed on silica, **1** exhibits unusually high mobility on the surface at room temperature, leading to the observation of a sharp liquid-like signal in the ³¹P solid-state NMR spectra.^{17,18}

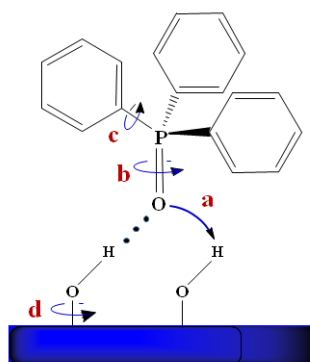


Figure 7. Possible modes of translational and rotational mobility of Ph₃PO (TPPO, **1**), adsorbed on alumina in a submonolayer. The jump from one OH group to the next involves a temporary detachment from the surface. Reprinted with permission from *J. Chem. Phys.* **2020**, *152*, 054718. Copyright 2020 AIP Publishing LLC.

When **1** is dry-ground with alumina instead of silica (Table 2), it also self-adsorbs on the surface, which most probably takes place by a translational motion as indicated by step **a** in Figure 7. We find a narrowing of the ^{31}P NMR signal as well (Figure 8). Additionally, the ^{31}P T_1 relaxation times of **1**, adsorbed on alumina, are very short with values between 2 to 4 s, in contrast to the long T_1 times of up to minutes expected for polycrystalline triarylphosphine species.^{17,40} The type of motion and reorientation of adsorbed **1**, as depicted in Figure 7 by the cases **a-d**, have not yet been investigated on any surface. Therefore, we sought to suggest a motional model for **1** on an alumina surface and to characterize the modes of mobility quantitatively. For this purpose, we have performed variable temperature NMR experiments, including ^{31}P T_1 relaxation time measurements for molecules of **1** adsorbed on alumina. In order to study the impact of the density of **1** on the surface, the coverage of the alumina surface has been varied from a dense monolayer (99%) to a sub-monolayer coverage of 25% (Table 2). Maximal coverage has been determined by offering an excess of polycrystalline **1** and determining the fraction of adsorbed versus left-over crystalline material, as described previously for adsorbed ferrocene.¹¹

Table 2. The samples investigated were polycrystalline Ph₃PO (TPPO, **1**) and **1** adsorbed on alumina with the indicated surface coverages. Reprinted with permission from *J. Chem. Phys.* **2020**, *152*, 054718. Copyright 2020 AIP Publishing LLC.

Sample	% surface coverage	mg per g of Al ₂ O ₃	mmol per g of Al ₂ O ₃	Particles on 100 nm ²
1	neat 1	-	-	-
2	25	7.33	0.0261	0.6
3	60	17.6	0.0631	1.4
4	75	22.0	0.0789	1.7
5	99	29.3	0.1040	2.3

In a first step, in order to establish the baseline spectroscopic properties of **1**, a polycrystalline sample of **1** was characterized by solid-state NMR. The static room temperature ³¹P{¹H} NMR spectrum of this compound is displayed in Figure 8. It shows a typical axially-symmetric CSA (chemical shift anisotropy) pattern.^{13,14} The spectrum, recorded at a spinning rate of 5 kHz, allows the calculation of the CSA parameters.¹⁴ The isotropic chemical shift corresponds to $\delta_{\text{iso}} = 26.0$ ppm, the CSA to $\Delta\sigma = -166$ ppm and the asymmetry parameter to $\eta = 0.06$. The values are close to those reported for the static tensor of **1**.⁴¹ Therefore, it can be concluded that no motions of polycrystalline **1** can be observed on the T₂ NMR time scale.

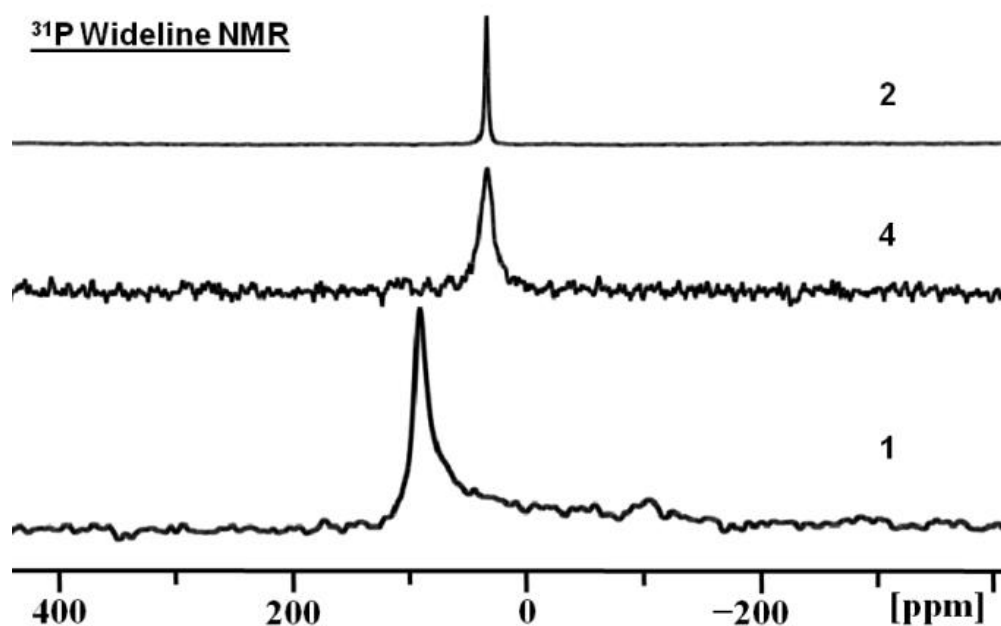


Figure 8. Static $^{31}\text{P}\{^1\text{H}\}$ NMR spectra of samples **2**, **4**, and polycrystalline **1**. For the simulated and calculated $^{31}\text{P}\{^1\text{H}\}$ MAS NMR spectrum of **1**, spinning at 5 kHz, see Figure A1. Reprinted with permission from *J. Chem. Phys.* **2020**, *152*, 054718. Copyright 2020 AIP Publishing LLC.

The ^{31}P T_1 relaxation time of **1** at 295 K, spinning at 5 kHz, has been determined as 60 s. At this point, two conclusions can be drawn from these measurements. First, the main CSA tensor component, potentially causing the relaxation via the CSA, does not change its orientation, even on the T_2 NMR time scale. Thus, the CSA mechanism can be ruled out. Second, the ^1H - ^{31}P dipole-dipole relaxation is not very effective, despite the number of protons in **1**. Obviously, this is due to the absence of free or high-amplitude rotations around the axis defined by the P=O bond and the P-C bonds. The latter is supported by the room temperature $^{13}\text{C}\{^1\text{H}\}$ CP/MAS NMR (CP, cross polarization)¹³⁻¹⁶ spectrum of polycrystalline **1**, spinning with 8.2 kHz (Figure 9, top). The spectrum shows five

relatively broad resonances for the phenyl rings, with δ values of 134.6, 133.2, 131.8, 130.2, and 128.0 ppm. In contrast to this, four resonances are observed for **1** dissolved in CDCl_3 ,^{19,42} where the phenyl groups are rotating freely around the P–C bonds. For comparison, sample **4** with **1** surface-adsorbed in a sub-monolayer on alumina only displays three resonances (Figure 9, bottom) which will be discussed at a later point. Although the mobility of polycrystalline **1** is obviously reduced as compared with surface-adsorbed **1**, or **1** in solution, limited ^1H - ^{31}P dipolar relaxation is still possible in polycrystalline **1** due to librations around the axis defined by the P=O bond and the P–C bonds.

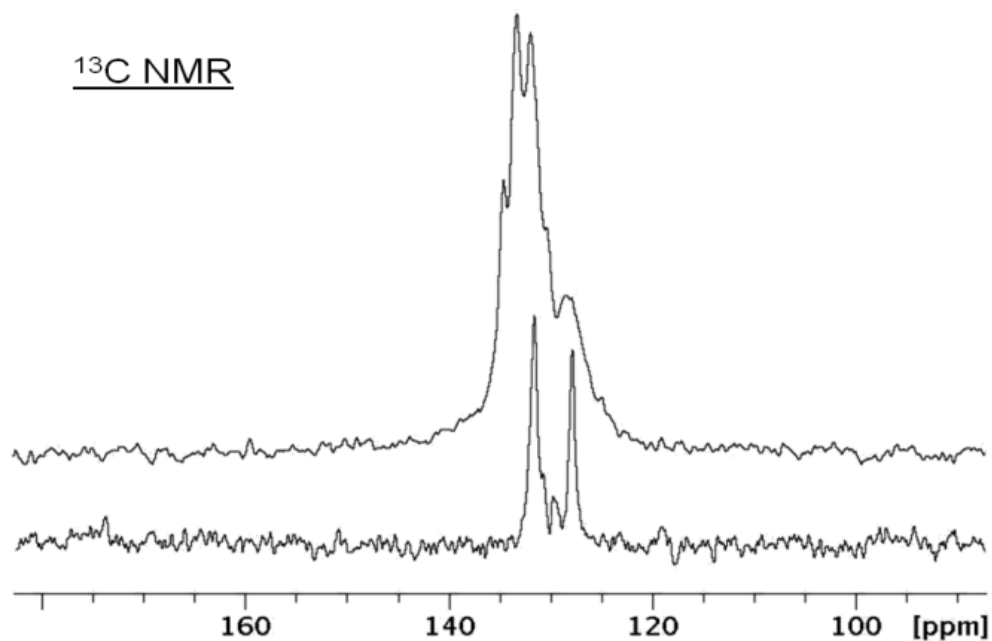


Figure 9. $^{13}\text{C}\{^1\text{H}\}$ CP/MAS NMR spectra of polycrystalline **1** (8.2 kHz, top) and **4** (8.0 kHz with direct ^{13}C excitation, bottom) at room temperature. Reprinted with permission from *J. Chem. Phys.* **2020**, *152*, 054718. Copyright 2020 AIP Publishing LLC.

The situation changes completely when proceeding from polycrystalline **1** to samples of **1** adsorbed on alumina (Table 2). In contrast to **1**, the static $^{31}\text{P}\{^1\text{H}\}$ NMR spectra of **2** to **5**, recorded at room temperature (Figure 10), exhibit a sharp resonance at $\delta(^{31}\text{P}) = 34.8$ ppm. This resonance represents the isotropic line of **1** adsorbed on the alumina surface. It is remarkable that the $^{31}\text{P}\{^1\text{H}\}$ NMR spectra of adsorbed **1**, for example of **4**, measured with ^1H - ^{31}P CP do not show any signals, even when the contact times are varied between 0.05 and 8 ms. Both spectroscopic effects correspond well to highly mobile molecules of **1** on the alumina surface, as qualitatively observed for **1** adsorbed on silica surfaces earlier.¹⁷

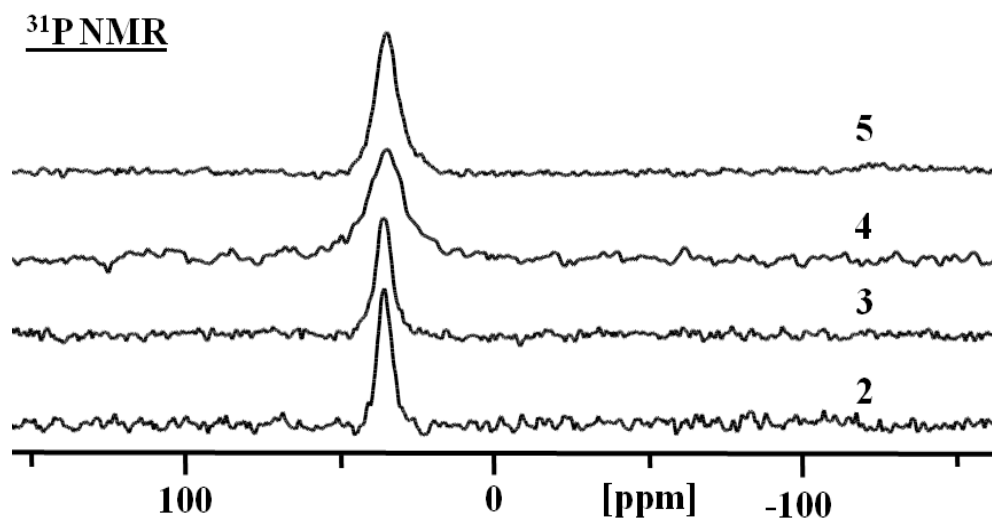


Figure 10. $^{31}\text{P}\{^1\text{H}\}$ static NMR spectra of **2** to **5**, recorded at 295 K. For the experimental and simulated spectra of **5** see Figure A2. Reprinted with permission from *J. Chem. Phys.* **2020**, *152*, 054718. Copyright 2020 AIP Publishing LLC.

Another important feature of the spectra displayed in Figure 10 is that the linewidths of the ^{31}P NMR resonances depend on the surface coverages of alumina with **1**. The halfwidths of the signals increase steadily from 0.6 kHz for **2**, to 0.7, 1.6, and 1.9 kHz for **3-5**. This result indicates that molecular motions of adsorbed **1** occur on the T_2 NMR time scale. In principle, the increased residual linewidth found for the samples 2-4 as compared to polycrystalline **1** could be the consequence of the P=O group interacting with different sites on the alumina surface. This scenario has, for example, been described in detail for the ^{15}N resonance of pyridine, adsorbed on aluminated SBA-15.^{39b} However, for adsorbed **1**, the linewidth was found to depend on the amount of alumina used per sample, or in other words, the surface coverage (Figure 10). Therefore, in the presented case the linewidth is the result of the exchange process.

The signals of adsorbed **1** do not show any CSA features (Figure 10). Therefore, isotropic, liquid-like reorientations of the molecules on the surface can be assumed. In accordance, the ^{31}P T_1 relaxation times in the alumina samples are short for static and spinning samples (5 kHz) at 295 K. The measured T_1 values are 1.4 s for **2-4** and 1.7 s for **5**. In comparison, polycrystalline **1** exhibits a ^{31}P T_1 relaxation time of 60 s under the same conditions. The practically exponential spin-lattice relaxation of the ^{31}P nuclei in the samples **2-5** is illustrated in Figure 10. This feature again corresponds to a liquid-like state of the adsorbed molecules on the alumina surface. It is important to note that, in contrast to the linewidth dependence on the degree of surface coverage (Figure 10), the ^{31}P T_1 time remains the same in the samples **2-4** and increases only insignificantly for **5**. Thus, besides

the libration motions discussed above, the molecules of adsorbed **1** show other very fast reorientations occurring on the T_1 NMR time scale.

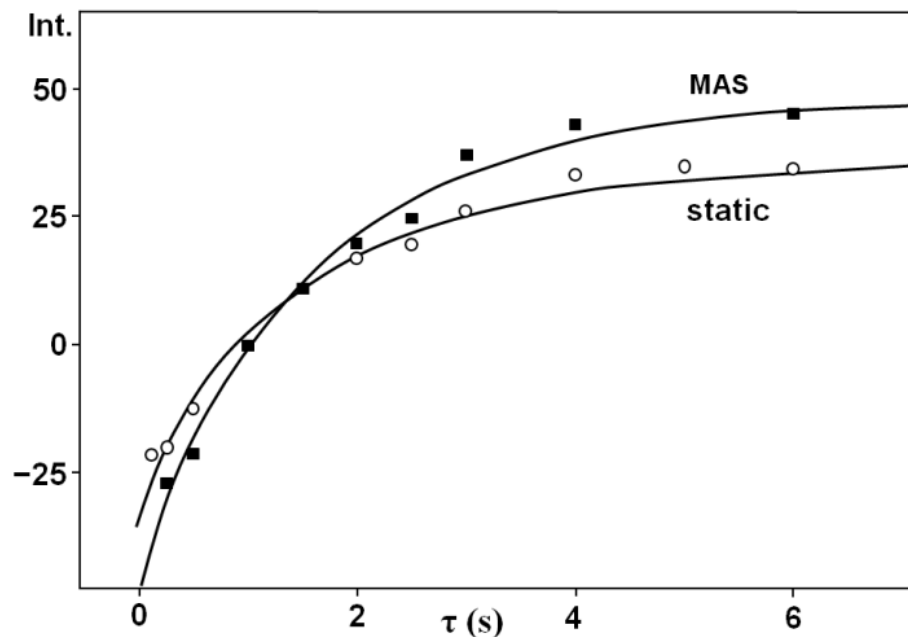


Figure 11. ^{31}P NMR signal intensities (arbitrary units) when using an inversion-recovery pulse sequence at 295 K for a static (0 kHz, ○) and a spinning sample (4 kHz, ■) of **3**. The inversion-recovery curves were treated with a stretched exponential $I(t) = \exp(-t/T_1)^\beta$. The solid lines were obtained with a β of 0.9 and $T_1 = 1.5$ s for the spinning, and $\beta = 0.85$ and $T_1 = 1.4$ s for the static case. Reprinted with permission from *J. Chem. Phys.* **2020**, *152*, 054718. Copyright 2020 AIP Publishing LLC.

The static variable temperature $^{31}\text{P}\{^1\text{H}\}$ NMR spectra, illustrated in Figure 12, characterize the slow motions in **4**. When the motions are frozen on the NMR time scale, the ^{31}P resonance experiences an evolution from a very sharp Lorentz-shaped line at 315 K to a CSA pattern at 183 K. This is confirmed by the simulation of the wide-line ^{31}P NMR spectrum of **4** at 253 K (Figure 11 and Figure A3).

The CSA pattern obtained for the sample spinning at a rate of 4 kHz was simulated to yield the isotropic chemical shift $\delta_{\text{iso}} = 34.8$ ppm, the CSA $\Delta\sigma = -110$ ppm, and the asymmetry parameter $\eta = 0.0$. It should be noted that the temperature dependence of the $\delta_{\text{iso}}(^{31}\text{P})$ is small when comparing resonances of adsorbed **1** obtained at 295 and 183 K.

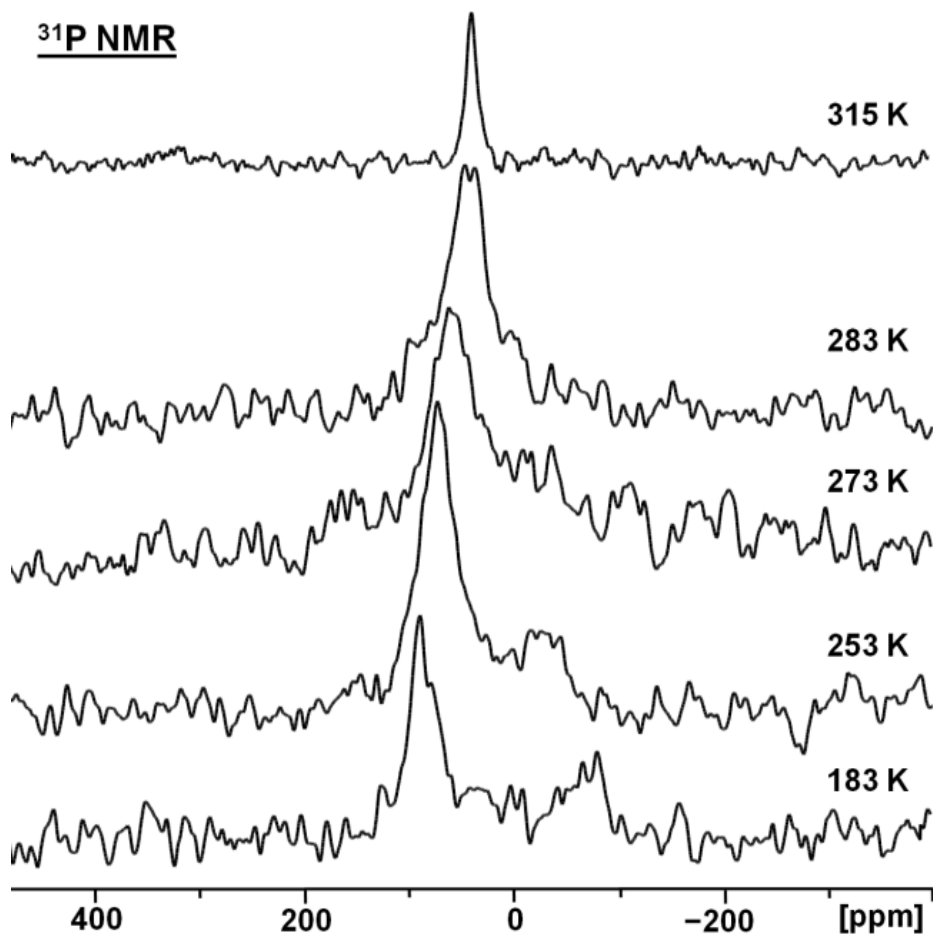


Figure 12. Temperature dependent static $^{31}\text{P}\{^1\text{H}\}$ NMR spectra of sample **4**, recorded at the indicated temperatures. For the experimental and simulated NMR spectrum, obtained at 253 K, see Figure A3. Reprinted with permission from *J. Chem. Phys.* **2020**, *152*, 054718. Copyright 2020 AIP Publishing LLC.

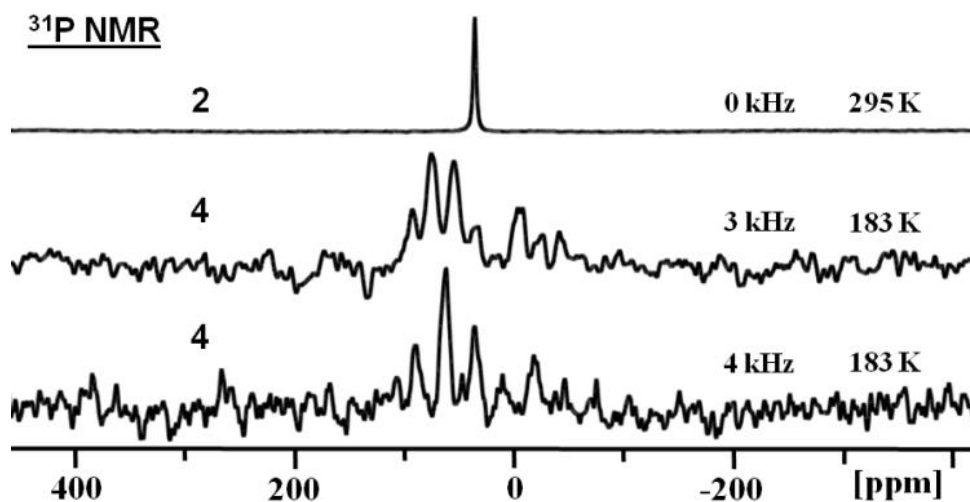


Figure 13. $^{31}\text{P}\{^1\text{H}\}$ NMR spectrum of static **2** recorded at 295 K and $^{31}\text{P}\{^1\text{H}\}$ MAS spectra of **4** with spinning speeds of 3 and 4 kHz at 183 K. For the experimental and simulated $^{31}\text{P}\{^1\text{H}\}$ NMR of **4**, spinning at 4 kHz at 183 K. Reprinted with permission from *J. Chem. Phys.* **2020**, *152*, 054718. Copyright 2020 AIP Publishing LLC.

A comparison of the $^{31}\text{P}\{^1\text{H}\}$ NMR data of **1** with those derived from samples **2-4** (Figure 9) shows that the isotropic chemical shift changes from 25 ppm for polycrystalline **1** to 35 ppm for adsorbed **1**. Similar ^{31}P downfield shifts were recently described for various trialkylphosphine oxides and **1** adsorbed on silica.^{17,18} Changes of the ^{31}P chemical shifts were also reported for substituted phenol and silanol adducts of **1** in solution⁴¹ and in the solid state.²⁰ Furthermore, H_2O_2 and di(hydroperoxy)alkane adducts of phosphine oxides display the same trend.²⁵⁻²⁹ For all these cases, the formation of hydrogen bonds between the different -OH groups and the O=P groups of the phosphine oxides has been proven independently by single crystal X-ray analyses. Therefore, the interactions between the alumina surface and adsorbed molecules of **1** can be attributed to the formation of hydrogen bonds of the type $\text{Ph}_3\text{P}=\text{O}\cdots\text{H}-\text{O}-\text{Al}$.⁴² As in the cases with other

-OH groups, the increase of the chemical shift value can be attributed to the deshielding of the ^{31}P nucleus by the electron withdrawing hydrogen bond. It should be noted, however, that the P=O group still retains its double bond. Full quaternization to Ph_3POH^+ is unlikely because alkoxyphosphonium cations of the type $[\text{R}_3\text{POR}]^+$ (R, R' = aryl, alkyl) exhibit much larger downfield shifts and CSA values.^{16b} For example, polycrystalline $[\text{Ph}_3\text{POEt}]^+\text{BF}_4^-$ resonates at 48.2 ppm and has a CSA value of 74 ppm.^{16b}

Nevertheless, the presence of a hydrogen bond to the phosphine oxide implies that there is a decreased P=O double bond character.^{19,25-29} This, in turn, could be associated with a decrease in the ^{31}P CSA value from 166 found for **1** to 110 ppm for **4**. However, since a minimal ^{31}P CSA value of 149 ppm has been found for the 2,4-dinitrophenol adduct of **1**,⁴¹ the low-temperature CSA tensor of **4** cannot be a true static tensor and some sort of motion must be present to explain the small value of 110 ppm for **4**. The best candidate for such a motional mode is the rotation around the P=O axis in hydrogen-bonded adsorbed species, illustrated as rotation **b** in Scheme 1. Finally, these interactions between the alumina surface and **1** are also visible in the ^{13}C NMR spectra of **4** (Figure 8). The *o*- and *m*-phenyl carbons become equivalent, resulting in narrow signals with δ values of 131.4 (C_i , C_o), 130.0 (C_p) and 127.7 (C_m) ppm, in accordance with the $\delta(^{13}\text{C})$ for a H_2O_2 adduct of **1** in solution.¹⁹

The temperature dependence of the $^{31}\text{P}\{^1\text{H}\}$ NMR spectra displayed in Figure 11 indicates a distinct spectroscopic effect, as the ^{31}P nuclei in **4** lose their CSA upon heating from 183 to 315 K. Such a lineshape evolution on the T_2 NMR time scale can only be observed when the hydrogen bond $\text{P}=\text{O}\cdots\text{H}-\text{O}$ dissociates and the molecules of **1** are

liberated. These molecules remain on the alumina surface due to van der Waals forces, however, they experience isotropic molecular reorientation. Eventually they form hydrogen bonds again, either with the same OH groups or adjacent ones. The simultaneous rotation of the surface OH groups (motion **d** in Figure 7) should facilitate the reattachment of **1** in the latter case that corresponds to jumps from one surface site to the next. Consequently, one should expect a dependence of the process rate on the surface coverage with **1** (see below). In this context, it should be noted that simple rotations, even very fast ones, around the axis defined by the P=O bonds in the P=O...H-O adducts (Figure 7, rotation **b**) cannot average out the CSA entirely, due to the remaining C_{3v} symmetry of surface-adsorbed molecules of **1**. The issue of surface detachment during the jumps from one OH group to an adjacent one has also been analyzed in detail for pyridine adsorbed on mesoporous silica surfaces,⁴³ however, analogies are limited because in contrast to this adsorbate, **1** is not volatile.

Table 3. The temperature dependence of the rate constants, K_{exch} , obtained by lineshape analysis of the variable temperature static $^{31}\text{P}\{^1\text{H}\}$ NMR spectra of **4**. Reprinted with permission from *J. Chem. Phys.* **2020**, *152*, 054718. Copyright 2020 AIP Publishing LLC.

T (K)	$K_{\text{exch}} (10^3 \cdot \text{s}^{-1})$
295	570
283	185
273	98
253	45

A lineshape analysis for the variable temperature ^{31}P NMR spectra of **4** (Figure S3), illustrating the loss of the CSA when increasing the temperature, has been performed within the limits of a two center exchange between δ_{33} and $\delta_{11} = \delta_{22}$ (Figure 11, 183 K) to obtain the process rate constants, K_{exch} , at different temperatures. The values summarized in Table 3 and illustrated in Figure 14 gave the kinetic characteristics $\Delta H^\ddagger = 8.5 \pm 0.5$ kcal/mol and $\Delta S^\ddagger = 7.4 \pm 2.0$ e.u.

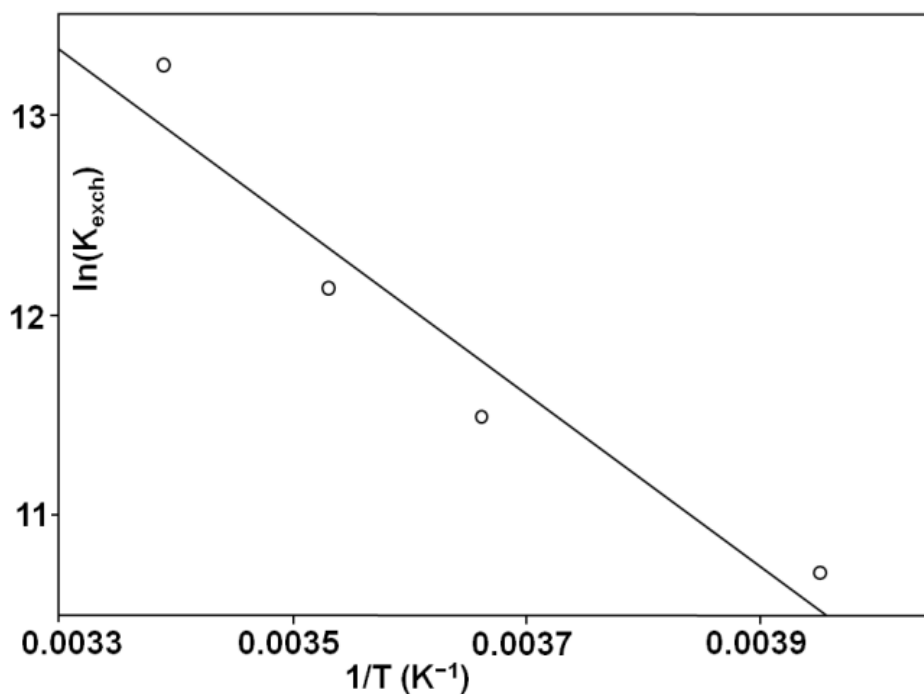


Figure 14. Temperature dependence of the rate constant K_{exch} , presented as the correlation of $\ln(K_{\text{exch}})$ with $1/T$. The values were obtained by lineshape analysis of the variable temperature static $^{31}\text{P}\{^1\text{H}\}$ NMR spectra of **4**. Reprinted with permission from *J. Chem. Phys.* **2020**, *152*, 054718. Copyright 2020 AIP Publishing LLC.

The rate constant K_{exch} also changes with the surface coverage of **1** on alumina, as determined by recording the $^{31}\text{P}\{^1\text{H}\}$ NMR spectra of samples **2-5** at 295 K (Figure 9). The values are summarized in Table 3 and graphically depicted in Figure 15. The latter shows that the rate decreases exponentially with increasing surface coverage. This result illustrates the importance of free OH surface sites, particularly for small coverages. Most probably, for large surface coverages the process goes through hydrogen bond dissociation exclusively, corresponding to a monomolecular transformation. This explains why the entropy ΔS^\ddagger (7.4 e.u., see above) is insignificant.

Table 4. The dependence of the exchange constant K_{exch} obtained at 295 K on the % surface coverage of **1** on alumina. Reprinted with permission from *J. Chem. Phys.* **2020**, *152*, 054718. Copyright 2020 AIP Publishing LLC.

Sample	% Surface Coverage	$K_{\text{exch}} (10^5 \cdot \text{s}^{-1})$
2	25	18
3	60	6.0
4	75	5.7
5	99	4.0

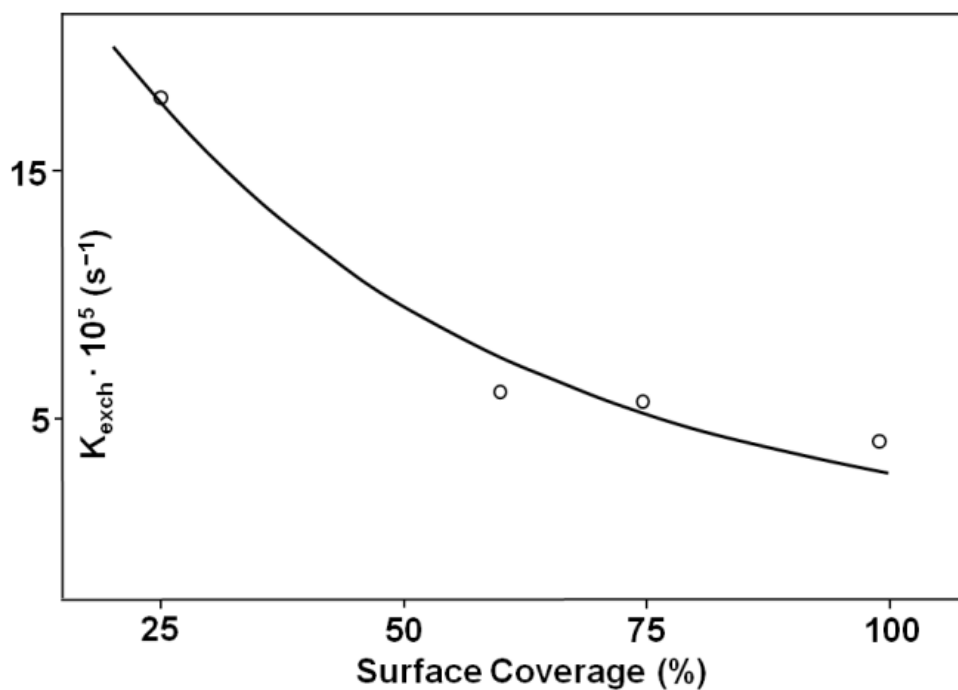


Figure 15. Dependence of the exchange constant K_{exch} on the surface coverage at 295 K. Reprinted with permission from *J. Chem. Phys.* **2020**, *152*, 054718. Copyright 2020 AIP Publishing LLC.

The variable temperature ^{31}P T_1 relaxation times, characterizing the fast reorientations of surface-adsorbed molecules of **1** in a static sample of **4** are listed in Table 4. In the context of possible relaxation mechanisms, it is important to emphasize that the relaxation is practically exponential (Figure 10) and that the ^{31}P T_1 time does not change when going from the static to spinning samples. Therefore, the spin-diffusion relaxation mechanism⁴⁴ can be ruled out.

Table 5. Dependence of the ^{31}P T_1 relaxation time on the temperature, obtained for a static sample of **4**. Reprinted with permission from *J. Chem. Phys.* **2020**, *152*, 054718. Copyright 2020 AIP Publishing LLC.

T (K)	T_1 of ^{31}P (s)
325	1.6
315	1.3
295	1.4
283	1.7
273	2.8
253	5.6
243	8.4
232	9.8

As discussed above, the ^{31}P CSA vector in **4** reorients on the T_2 NMR time scale. Therewith, the T_1 CSA relaxation mechanism is also ineffective. Figure 16 depicts the temperature dependence of the ^{31}P T_1 relaxation time in coordinates of $\ln T_1$ versus $1000/T$, characterizing fast reorientations of the adsorbed molecules of **1** in sample **4**.

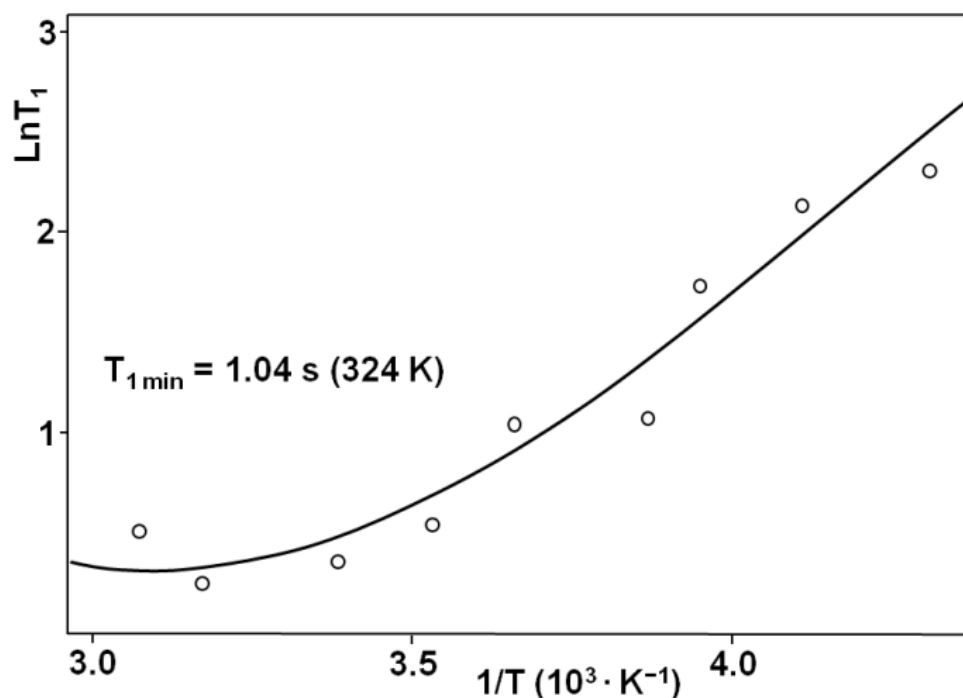


Figure 16. The temperature dependence of the ^{31}P T_1 time in coordinates $\ln T_1$ versus $1000/T$ obtained for a static sample of **4**. The solid line corresponds to the treatment of the experimental data according to equation (1). Reprinted with permission from *J. Chem. Phys.* 2020, 152, 054718. Copyright 2020 AIP Publishing LLC.

The curve in Figure 9, obtained as described below, is V-shaped and shows a ^{31}P $T_{1\text{min}}$ time of about 1 s at 324 K. This $T_{1\text{min}}$ temperature is close to the value of 341 K that was observed for the ^{31}P relaxation in the tin phosphonate material,⁴⁵ where the relaxation process is fully governed by the ^1H - ^{31}P dipolar mechanism. This mechanism is activated by rotations of phenylene rings,⁴⁵ as exemplified for adsorbed **1** as rotation **c** in Scheme 1. These rotations, in turn, reorient the dipolar $\text{P}\cdots\text{H}$ vectors. The ^{31}P $T_{1\text{min}}$ time measured in the tin phosphonate material⁴⁵ is remarkably longer (6.8 s) than the 1 s for **4**. In the context of the dipolar mechanism, however, this is not surprising because the number of protons close to the ^{31}P nuclei in the molecules of **1** is larger. In addition, the ^{31}P T_1 CSA

relaxation mechanism is obviously ineffective because the ^{31}P CSA vector in **4** reorients slowly on the T_2 NMR time scale.

Based on all the NMR data we suggest that the ^{31}P relaxation of molecules of **1** adsorbed on the alumina surface is dipolar and governed by fast rotations of the $\text{Ph}_3\text{P}=\text{O}$ molecules around the axis defined by the $\text{P}=\text{O}$ bonds, depicted as rotation **b** in Scheme 1. While the impact of phenyl group rotation according to rotational mode **c** in Scheme 1 cannot be excluded entirely at this point, the theoretically obtained energy barriers to phenyl ring rotations in solid Ph_3PO are dominated by steric interactions and comparatively high.⁴⁶ Due to the fast $\text{Ph}_3\text{P}=\text{O}$ rotations around the $\text{P}=\text{O}$ axis, the T_1 relaxation time of the phenyl protons, showing a narrow ^1H NMR signal at 6.6 ppm (Figure 17) is also short, with a value of 0.48 s. This is close to the ^1H relaxation time of the phenylene protons in the tin phosphonate materials.⁴⁵ The broad signal at about 4 ppm stems from the alumina support.

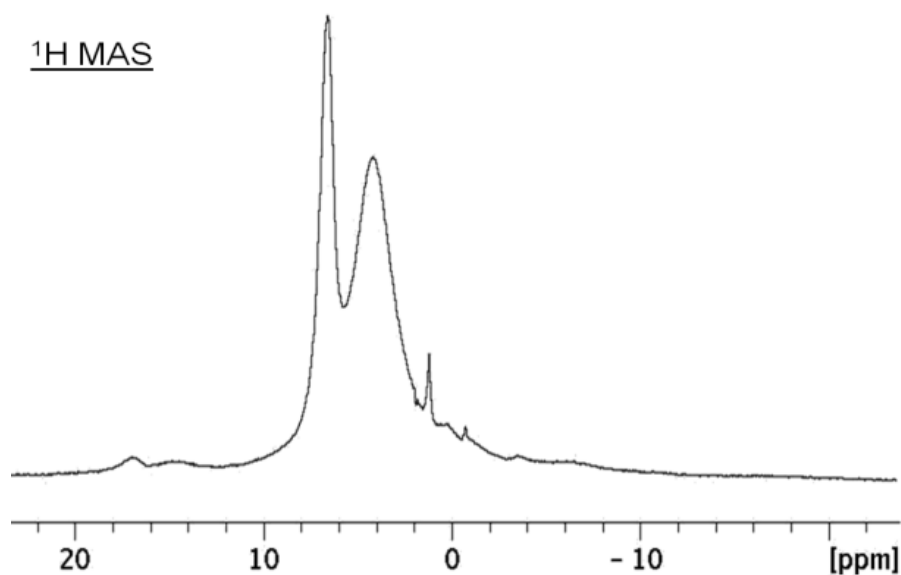


Figure 17. ^1H MAS NMR spectrum of **4** (4 kHz, 295 K). Reprinted with permission from *J. Chem. Phys.* **2020**, *152*, 054718. Copyright 2020 AIP Publishing LLC.

The variable-temperature ^{31}P T_1 relaxation in a static sample of **4** (Figure 16) has been treated with equation (4).⁴⁷

$$(4) \ 1/T_1 = (4/30) (\mu_0/4\pi)^2 r(\text{P-H})^{-6} \gamma_{\text{P}}^2 \gamma_{\text{H}}^2 \hbar^2 I_{\text{H}}(I_{\text{H}}+1) \times \{3\tau_{\text{C}}/(1+\omega_{\text{P}}^2\tau_{\text{C}}^2) + 6\tau_{\text{C}} / (1 + (\omega_{\text{P}} + \omega_{\text{H}})^2\tau_{\text{C}}^2) + \tau_{\text{C}} / (1 + (\omega_{\text{P}} - \omega_{\text{H}})^2\tau_{\text{C}}^2)\}$$

Here, ω_{P} and ω_{H} are the ^{31}P and ^1H resonance frequencies, $\omega = 2\pi\nu$, $\tau_{\text{C}} = \tau_0 \exp(\Delta E/RT)$ and ΔE is the activation energy. While in general, $1/\tau_0$ represents the frequency of attempts needed to overcome the energy barrier, here τ_0 serves only as a fitting parameter. The good fit (solid line) supports the interpretation based on a ^1H - ^{31}P dipolar mechanism and provides the activation energy ΔE of 5.4 ± 0.5 kcal/mol

characterizing the Ph₃P=O rotation around the P=O axis (rotation **b** in Scheme 1). Note that a smaller energy of 3 kcal/mol has been reported for the rotation of phenylene rings in tin phosphonate materials.⁴⁵ This is a logical consequence of the larger inertia moment of the rotating Ph₃P=O group. Interestingly, 3.6 kcal/mol also characterize the phosphate head group rotation in dimyristoylphosphatidylcholine membranes in the liquid crystalline phase.⁴⁸

Equation (1) is only valid for isotropic motions,⁴⁷ while the Ph₃P=O rotation around the P=O axis is anisotropic in nature. However, as shown earlier, when an isotropic model is applied for anisotropic motions,⁴⁹⁻⁵¹ the ΔE value is still meaningful, and the correlation time constant τ_0 remains an effective parameter. In fact, according to the fitting procedure in Figure 16, a τ_0 value can be calculated as $2.8 \cdot 10^{-6}$ for rotations in **4**.

Conclusions

Triphenylphosphine oxide (TPPO, **1**) has been adsorbed on neutral alumina by dry grinding of the components in the absence of a solvent. The adsorption proves qualitatively that there is translational mobility of **1** on the surface of alumina. Different surface coverages, from a densely packed monolayer (99% coverage) to a dilute sub-monolayer (25%) have been produced. The samples have been studied by diverse multinuclear ¹H, ¹³C, and ³¹P variable temperature solid-state NMR techniques. The interactions of **1** with the surface are dominated by hydrogen bonding of the P=O group to OH groups on the alumina surface. The ³¹P solid-state NMR spectra prove that even at low temperatures the molecules of **1** are highly mobile on the surface. Using T₁ and T₂

relaxation time analyses of the ^{31}P resonance in the solid state at variable temperatures allowed the identification and quantification of two different modes of mobility. Besides the translational mobility that consists of jumps from one hydrogen-bonding OH site on the surface to an adjacent one, a rotational movement around the axis defined by the P=O group of **1** occurs. These results are phenomenologically interesting, and they provide valuable insight about mobilities on the surface. Since adsorption on surfaces is the first step prior to reactions taking place, the deeper insight into the motional processes on the surface will lead to a better understanding of reactivities, for example, in surface-assisted and stereoselective chemistry.

Experimental Section

The $^{31}\text{P}\{^1\text{H}\}$, $^{13}\text{C}\{^1\text{H}\}$ CP, and ^1H spinning (MAS) and static (wideline) NMR experiments were carried out on a Bruker Avance 400 solid-state NMR spectrometer (400 MHz for ^1H nuclei), equipped with standard two-channel 7 mm and 4 mm MAS probe heads. The standard single pulse (direct nuclear excitation with a 50° rf pulse) and CP pulse sequences were applied for the nuclei ^{31}P and ^{13}C with recycle delays of 10 and 12 s, respectively, needed for complete spin-lattice relaxation. The contact times of 2 ms and 5 ms were adjusted for the standard $^{13}\text{C}\{^1\text{H}\}$ and $^{31}\text{P}\{^1\text{H}\}$ CP/MAS NMR experiments, respectively. The $^{13}\text{C}\{^1\text{H}\}$ MAS NMR experiment for solid TPPO required a recycle delay of 25 s due to a long ^1H relaxation time. The *tppm15* (two pulse phase modulation) pulse sequence has been used for complete ^1H decoupling. The external standards used for

referencing the solid-state NMR chemical shifts were TMS (^1H , ^{13}C) and H_3PO_4 solutions (^{31}P).

The variable temperature ^{31}P NMR experiments were performed using a standard temperature unit of the spectrometer calibrated with liquid methanol placed into a 7 mm rotor. ^{31}P T_1 relaxation times were measured by inversion–recovery ($180^\circ - \tau - 90^\circ$) experiments, the rf pulses were calibrated, and the τ delays widely varied to determine estimates of T_1 relaxation times. Relaxation (recycle) delays were adjusted to provide complete nuclear relaxation in each cycle.

The experimental ^1H and ^{31}P inversion–recovery data "signal intensity versus τ time" have been treated with a standard nonlinear fitting computer program based on the Levenberg–Marquardt algorithm.⁷¹ The statistical error margins for the determined ^{31}P T_1 relaxation times were <15%. The lineshape analysis of the variable temperature $^{31}\text{P}\{^1\text{H}\}$ static NMR spectra was performed with a Bruker DNMR program of the spectrometer software.

Pure triphenylphosphine oxide was obtained by oxidizing triphenylphosphine with aqueous hydrogen peroxide and removing hydrogen-bound water and hydrogen peroxide with molecular sieves as described earlier.³⁸

The support material aluminum oxide, (γ phase with 5-20% α phase, 99.98% purity based on metals, average pore diameter 90 Å, specific surface area 100 m^2/g) was purchased from Alfa Aesar and dried at 180 °C for 48 hours under vacuum prior to use. In a representative adsorption procedure 22.0 mg (0.079 mmol) of triphenylphosphine oxide was dry ground for five minutes together with 1 g of

aluminum oxide using a mortar and pestle. The sample was then moved to a vial and the adsorption process was allowed to proceed to completion overnight.

References

1. M. Ebener, G. Von Fircks, H. Günther, *Helv. Chim. Acta* **1991**, *74*, 1296-1304.
2. H. Günther, S. Oepen, M. Ebener, V. Francke, *Magn. Reson. Chem.* **1999**, *37*, S142-S146.
3. B. Rebenstorf, C. Panda, *J. Mol. Catal.* **1991**, *65*, 173-180.
4. P. J. Hubbard, J. W. Benzie, V. L. Bakhmutov, J. Blümel, *J. Chem. Phys.* **2020**, *152*, 054718
5. M. Schnellbach, J. Blümel, F. H. Köhler, *J. Organomet. Chem.* **1996**, *520*, 227-230.
6. Y. Oprunenko, I. Gloriov, K. Lyssenko, S. Malyugina, D. Mityuk, V. Mstislavsky, H. Günther, G. Von Firks, M. Ebener, *J. Organomet. Chem.* **2002**, *656*, 27-42.
7. K. J. Cluff, M. Schnellbach, C. R. Hilliard, J. Blümel, *J. Organomet. Chem.* **2013**, *744*, 119-124.
8. K. J. Cluff, N. Bhuvanesh, J. Blümel, *Organometallics* **2014**, *33*, 2671-2680.
9. K. J. Cluff, N. Bhuvanesh, J. Blümel, *Chem. Eur. J.* **2015**, *21*, 10138-10148.
10. K. J. Cluff, J. Blümel, *Chem. Eur. J.* **2016**, *22*, 16562-16575.
11. K. J. Cluff, J. Blümel, *Organometallics* **2016**, *35*, 3939-3948.

12. C. A. Fyfe, *Solid-State NMR for Chemists*. C.F.C. Press, Guelph, Canada, **1983**.
13. T. M. Duncan, *A Compilation of Chemical Shift Anisotropies*. Farragut Press: Chicago, IL, **1990**.
14. A. T. Bell, *NMR Techniques in Catalysis*. Taylor & Francis: **1994**.
15. (a) S. Reinhard, J. Blümel, *Magn. Reson. Chem.* **2003**, *41*, 406-416. (b) J. Sommer, Y. Yang, D. Rambow, J. Blümel, *Inorg. Chem.* **2004**, *43*, 7561-7563.
16. C. R. Hilliard, S. Kharel, K. J. Cluff, N. Bhuvanesh, J. A. Gladysz, J. Blümel, *Chem. Eur. J.* **2014**, *20*, 17292-17295.
17. S. Kharel, K. J. Cluff, N. Bhuvanesh, J. A. Gladysz, J. Blümel, *Chem. Asian J.* **2019**, *14*, 2704-2711.
18. C. R. Hilliard, N. Bhuvanesh, J. A. Gladysz, J. Blümel, *Dalton Trans.* **2012**, *41*, 1742-1754.
19. S. Kharel, N. Bhuvanesh, J. A. Gladysz, J. Blümel, *Inorg. Chim. Acta* **2019**, *490*, 215-219.
20. (a) S. J. Pike, C. A. Hunter, *Org. Biomol. Chem.* **2017**, *15*, 9603-9610. (b) A. E. Stross, G. Iadevaia, C. A. Hunter, *Chem. Sci.* **2016**, *7*, 94-101. (c) G. Iadevaia, A. E. Stross, A. Neumann, C. A. Hunter, *Chem. Sci.* **2016**, *7*, 1760-1767. (d) R. Cuypers, E. J. R. Sudhölter, H. Zuilhof, *ChemPhysChem.* **2010**, *11*, 2230-2240.
21. N. A. Bewick, A. Arendt, Y. Li, S. Szafert, T. Lis, K. A. Wheeler, J. Young, R. Dembinski, *Curr. Org. Chem.* **2015**, *19*, 469-474.
22. S. J. Pike, C. A. Hunter, *Org. Biomol. Chem.* **2017**, *15*, 9603-9610.

23. N. J. Burke, A. D. Burrows, M. F. Mahon, J. E. Warren, *Inorg. Chim. Acta* **2006**, *359*, 3497-3506.
24. F. F. Arp, N. Bhuvanesh, J. Blümel, *Dalton Trans.* **2019**, *48*, 14312–14325.
25. S. H. Ahn, K. J. Cluff, N. Bhuvanesh, J. Blümel, *Angew. Chem.* **2015**, *127*, 13539-13543, *Angew. Chem. Int. Ed.* **2015**, *54*, 13341-13345.
26. S. H. Ahn, N. Bhuvanesh, J. Blümel, *Chem. Eur. J.* **2017**, *23*, 16998-17009.
27. S. H. Ahn, D. Lindhardt, N. Bhuvanesh, J. Blümel, *ACS Sustainable Chem. Eng.* **2018**, *6*, 6829-6840.
28. F. F. Arp, S. H. Ahn, N. Bhuvanesh, J. Blümel, *New J. Chem.* **2019**, *43*, 17174-17181.
29. (a) E. Y. Tupikina, M. Bodensteiner, P. M. Tolstoy, G. S. Denisov, I. G. Shenderovich, *J. Phys. Chem. C* **2018**, *122*, 1711-1720. (b) G. Begimova, E. Y. Tupikina, V. K. Yu, G. S. Denisov, M. Bodensteiner, I. G. Shenderovich, *J. Phys. Chem. C* **2016**, *120*, 8717-8729.
30. (a) J. Blümel, *Coord. Chem. Rev.* **2008**, *252*, 2410-2423. (b) J. Guenther, J. Reibenspies, J. Blümel, *Adv. Synth. Catal.* **2011**, *353*, 443-460. (c) R. Silbernagel, A. Diaz, E. Steffensmeier, A. Clearfield, J. Blümel, *J. Mol. Catal. A* **2014**, *394*, 217-223. (d) C. Merckle, J. Blümel, *Adv. Synth. Catal.* **2003**, *345*, 584-588. (e) C. Merckle, J. Blümel, *Top. Catal.* **2005**, *34*, 5-15. (f) J. Guenther, J. Reibenspies, J. Blümel, *Mol. Catal.* **2019**, *479*, 110629.
31. (a) J. H. Baker, N. Bhuvanesh, J. Blümel, *J. Organomet. Chem.* **2017**, *847*, 193-203. (b) Y. Yang, B. Beele, J. Blümel, *J. Am. Chem. Soc.* **2008**, *130*, 3771-3773. (c) B. Beele, J. Guenther, M. Perera, M. Stach, T. Oeser, J. Blümel, *New J. Chem.* **2010**, *34*, 2729-2731.
32. (a) J. C. Pope, T. Posset, N. Bhuvanesh, J. Blümel, *Organometallics* **2014**, *33*, 6750-6753. (b) T. Posset, J. Blümel, *J. Am. Chem. Soc.* **2006**, *128*, 8394-8395. (c) T. Posset, J. Guenther, J. Pope, T. Oeser, J. Blümel, *Chem. Commun.* **2011**, *47*, 2059-2061.

33. (a) S. Reinhard, P. Soba, F. Rominger, J. Blümel, *Adv. Synth. Catal.* **2003**, *345*, 589-602. (b) F. Piestert, R. Fetouaki, M. Bogza, T. Oeser, J. Blümel, *Chem. Commun.* **2005**, 1481-1483. (c) K. J. Cluff, N. Bhuvanesh, J. Blümel, *Chem. Eur. J.* **2015**, *21*, 10138-10148.
34. (a) A. Zheng, S.-B. Liu, F. Deng, *Chem. Rev.* **2017**, *117*, 12475–12531. (b) R. Yerushalmi, J. C. Ho, Z. Fan, A. Javey, *Angew. Chem. Int. Ed.* **2008**, *47*, 4440-4442. (c) J. P. Osegovic, R. S. Drago, *J. Phys. Chem. B* **2000**, *104*, 147-154. (d) S. Hayashi, K. Jimura, N. Kojima, *Bull. Chem. Soc. Jpn.* **2014**, *87*, 69-75. (e) S. Machida, M. Sohmiya, Y. Ide, Y. Sugahara, *Langmuir* **2018**, *34*, 12694–12701.
35. (a) A. R. Wilmsmeyer, W. O. Gordon, E. D. Davis, B. A. Mantooth, T. A. Lalain, J. R. Morris, *Rev. Sci. Instrum.* **2014**, *85*, 014101. (b) J. Kemsley, *Chem. Eng. News* **2014**, *92*, 29-30.
36. S. Kharel, T. Jia, N. Bhuvanesh, J. H. Reibenspies, J. Blümel, J. A. Gladysz, *Chem. Asian J.* **2018**, *13*, 2632-2640.
37. (a) J. Chrzanowski, D. Krasowska, J. Drabowicz, *Heteroatom Chem.* **2018**, *29*, 21476. (b) T. Kovacs, G. Keglevich, *Curr. Org. Chem.* **2017**, *21*, 569-585. (c) D. Herault, D. H. Nguyen, D. Nuel, G. Buono, *Chem. Soc. Rev.* **2015**, *44*, 2508-2528. (d) M. D. Fletcher, *Organophosphorus Reagents*, ed. P. J. Murphy, Oxford University Press, **2004**, 171-214. (e) H. R. Hays, D. J. Peterson, *Org. Phosphorus Compounds* **1972**, *3*, 341-500. (f) H. Adams, R. C. Collins, S. Jones, C. J. A. Warner, *Org. Lett.* **2011**, *13*, 6576-6579. (g) K. C. K. Swamy, N. N. B. Kumar, E. Balaraman, K. V. P. P. Kumar, *Chem. Rev.* **2009**, *109*, 2551-2651. (h) R. H. Beddoe, K. G. Andrews, V. Magné, J. D. Cuthbertson, J. Saska, A. L. Shannon-Little, S. E. Shanahan, H. F. Sneddon, R. M. Denton, *Science* **2019**, *365*, 910-914.
38. (a) C. Merckle, J. Blümel, *Chem. Mater.* **2001**, *13*, 3617-3623. (b) A. A. Gurinov, Y. A. Rozhkova, A. Zukal, J. Cejka, I. G. Shenderovich, *Langmuir* **2011**, *27*, 12115-12123.
39. D. E. Axelson, Multiscience Publications Limited, Canada, **1985**.
40. C. M. Lagier, U. Scheler, G. McGeorge, M. G. Sierra, A. C. Olivieri, R. K. Harris, *J. Chem. Soc. Perkin Trans.* **1996**, *2*, 1325-1329.

41. T. A. Albright, W. J. Freeman, E. E. Schweizer, *J. Org. Chem.* **1975**, *40*, 3437-3441.
42. I. G. Shenderovich, G. Buntkowsky, A. Schreiber, E. Gedat, S. Sharif, J. Albrecht, N. S. Golubev, G. H. Findenegg, H.-H. Limbach, *J. Phys. Chem. B* **2003**, *107*, 11924-11939.
43. H. Kessemeier, R. E. Norberg, *Phys. Rev.* **1967**, *155*, 321-337.
44. J. A. Sheikh, V. I. Bakhmutov, A. Clearfield, *Magn. Reson. Chem.* **2018**, *56*, 276-284.
45. N. De Silva, F. Zahariev, B. P. Hay, M. S. Gordon, T. L. Windus, *J. Phys. Chem. A* **2015**, *119*, 8765-8773.
46. V. I. Bakhmutov, *NMR Spectroscopy in Liquids and Solids*, CRC Press, Boca Raton, Florida, 2015, 59.
47. E. J. Dufourc, C. Mayer, J. Stohrer, G. Althoff, G. Kothel, *Biophys. J.* **1992**, *61*, 42-57.
48. D. G. Gusev, D. Nietlispach, A. B. Vymenits, V. I. Bakhmutov, H. Berke, *Inorg. Chem.* **1993**, *32*, 3270-3276.
49. V. I. Bakhmutov, *Magn. Reson. Chem.* **2004**, *42*, 66-70.
50. G. Lipari, A. Szabo, *J. Am. Chem. Soc.* **1982**, *104*, 4546-4559.
51. K. A. Levenberg, *Quart. Appl. Math.* **1994**, *2*, 164-168.

CHAPTER III

FERROCENE ADSORBED ON SILICA AND ACTIVATED CARBON SURFACES: A SOLID-STATE NMR STUDY OF MOLECULAR DYNAMICS AND SURFACE INTERACTIONS*

Introduction

Carbon allotropes play an important role in modern and future advances in science and engineering, and their importance cannot be overestimated.¹ New carbon allotropes are still detected, as the recently discovered molecular C₁₈ rings show.² Common applications range from the popular carbon-supported palladium catalyst to nanometer-scale electronics of the future.¹ Importantly from an environmental perspective, organic and inorganic pollutants can be very efficiently adsorbed onto the surface of activated carbon, graphene oxide and carbon nanotubes (CNT) from aqueous solution and gas streams.³⁻¹⁰ Recently, volatile odorous compounds (VOC) have been efficiently trapped on modified activated carbon surfaces, as described in the last chapter of this thesis.¹¹

Activated carbon represents the most important allotrope that is applied on a large scale. It constitutes an indispensable sorbent in medicine, and for catalysis and purification procedures.¹² Because it is less expensive compared to other carbon allotropes, it is employed in many commercially available forms.¹² Activated carbon is also environmentally benign, as it can be derived from biomass.¹³ Furthermore, special

*Reproduced with permission from “Ferrocene Adsorbed on Silica and Activated Carbon Surfaces: A Solid-State NMR Study of Molecular Dynamics and Surface Interactions”, P. J. Hubbard, J. W. Benzie, V. I. Bakhmutov, J. Blümel, *Organometallics* **2020**, *39*, 1080-1091 DOI: 10.1021/acs.organomet.9b00800. Copyright 2020 American Chemical Society.

activated carbon materials show promise for removing CO₂ from gas streams¹⁴ and heavy metals like Hg²⁺, Cr⁶⁺ and Cd²⁺, and toxic organic contaminants from wastewater.^{3,4}

In general, the adsorption of small molecules on surfaces is important for processes in industry and academia that involve separation sciences and catalysis. NMR spectroscopic adsorption studies with activated carbon or other supports have focused mainly on *liquids* like water, alcohols and benzene.¹⁵⁻¹⁷ ²H NMR has, for example, been used to study alcohols confined in activated carbon fibers at low temperatures.¹⁷ Spectroscopic studies on adsorbed *solids* are more scarce. One example would involve phenanthrene adsorbed on biochars.¹⁸ Solid-state NMR spectroscopy^{19,20} is a powerful tool to investigate surface species, for example, immobilized catalysts on support surfaces.²¹ Furthermore, polycyclic aromatic hydrocarbons (PAH) have been adsorbed on silica²² and studied by ¹³C solid-state NMR.²³

The two most important anisotropic interactions that occur in the solid state and are utilized in NMR are the Chemical Shift Anisotropy (CSA)^{19,20} and quadrupolar interactions.¹⁹ The CSA reflects the unsymmetry of the electronic surroundings of a nucleus. The spherically rather symmetric phosphonium salts, for example, have a small ³¹P CSA in the solid state,^{21f,g} while polycrystalline phosphine oxides display a large CSA.^{24,25} The same accounts for phosphines versus their metal complexes.²¹ A large CSA manifests in solid-state NMR spectra in the form of multiple sets of rotational sidebands besides the isotropic line when samples are rotated. The CSA parameters can be derived by simulations from the spectra of rotated samples, or by measuring wideline spectra without spinning.¹⁹⁻²¹ In case a quadrupolar nucleus with nuclear spin $I = 1$ like ²H or ¹⁴N

is measured in the solid state, the large quadrupolar interactions lead to a Pake pattern.¹⁹ The distance between the center lines of this Pake pattern can be used to determine the characteristic quadrupolar coupling constant.¹⁹ In solution, both anisotropic interactions are completely averaged out and only the isotropic lines are seen in the spectra. However, in case the mobility is limited and only partial averaging occurs, the residual CSA and diminished quadrupolar coupling constant can be used to determine different modes of mobility, as described for ferrocene in the results and discussion section.

We reported recently that species like phosphine oxides²⁶ can be adsorbed on diverse surfaces by dry grinding, and we could demonstrate that they are mobile on silica surfaces.^{24,25} Regarding the adsorption of phosphine oxides on silica the interactions with the surface are rather well-defined. The oxygen of the P=O functionality forms hydrogen bonds with surface silanol groups.²⁴⁻²⁶ Molecular hydrogen-bonded adducts of P=O groups with silanols,^{24,27} phenols,^{27,28} chloroform,²⁷ hydrogen peroxide,²⁹ and di(hydroperoxy)alkanes³⁰ have all been identified by single crystal X-ray diffraction.

Recently, we discovered that metallocenes of the type Cp₂M (Cp = cyclopentadienyl, C₅H₅) can be adsorbed on silica by dry grinding of the components in the absence of solvents.³¹⁻³³ In contrast to the phosphine oxides, hydrogen bonding can be excluded for the interactions of these metallocenes with silica or activated carbon surfaces. The interactions with the surfaces must be of a van der Waals type nature, but the orientation of ferrocene with respect to the surface is not yet known.

Under an inert atmosphere ferrocene does not undergo chemical reactions even with supports such as silica or alumina, in contrast to other types of metallocenes. In contrast, the important polymerization catalysts of the type Cp_2MCl_2 react readily via the chloride ligands when they are supported on silica,^{34,35} or incorporated into polymers³⁶ or sol-gel-type materials.³⁷ But even in the absence of chloride ligands, some of the Cp_2M metallocenes react quickly with oxide surfaces after the adsorption step. On a silica or alumina surface, chromocene forms the important heterogeneous Union Carbide catalyst that is used industrially for olefin polymerization under mild conditions in the absence of a co-catalyst.^{38,39} Despite the importance of this catalyst, its structure remains largely unknown. The commonly accepted partial structure of the catalytically active surface species consists of a CpCr(III) moiety that must be bound to a surface siloxide anion, as determined by solid-state NMR,⁴⁰ and XPS and IR studies.³⁸

In our quest to elucidate the adsorption and subsequent reaction of the surface-bound chromium species, chromocene has been dry-ground with silica in the absence of a solvent that could influence the outcome of the surface reaction.⁴⁰ However, even without solvent the reaction is too fast and does not allow for sufficient time to study the initial elementary steps by solid-state NMR or other methods. Therefore, in the presented work, we turned to the less reactive ferrocene that persists under inert gas for months with the same structure as chromocene. By obtaining a deeper insight about the dynamic processes of the adsorption of ferrocene on different surfaces, conclusions about the structurally similar chromocene should be possible. Especially the orientation of the ferrocene towards the surface is of interest, since the reaction, for example, with surface silanol groups can only

take place after contact with the metal center, but not through the Cp ring. Any, albeit temporary, sideways orientation of a metallocene should facilitate the interaction of the metal with the surface. Regarding activated carbon surfaces, while there is no chemical reaction taking place when ferrocene or chromocene are adsorbed, comparing data from different surfaces allows for a complete quantitative analysis of the adsorption process by solid-state NMR spectroscopy.^{31,40} Another incentive to study the interactions of Cp₂M-type metallocenes adsorbed in monolayers with support surfaces is related to the potential creation of single atom catalysts by reducing the metal center.³³

Previously, we have explored the dry adsorption of ferrocene and other metallocenes on the surfaces of activated carbon and silica²² from a phenomenological perspective.³¹⁻³³ Even in the absence of solvents the metallocenes that have been adsorbed by dry grinding display dynamic effects. Accordingly, it could recently been demonstrated qualitatively with multinuclear dia- and paramagnetic solid-state NMR that metallocenes are mobile on the surface within the pores of amorphous silica and activated carbon.^{31-33,40} It has also been visualized on a cm length scale that ferrocene is translationally mobile in large silica gel specimens.³³ Importantly with respect to a later application in catalysis, when the adsorption is undertaken in the absence of a solvent, well-defined monolayers are formed.³³ No stacking of metallocenes in multiple layers on the surface occurs on any support.³¹⁻³³ In case an excess of metallocene is offered, it remains in its polycrystalline form and does not adsorb.

Ferrocene and its derivatives are classic organometallic compounds that play a crucial role in such important fields as catalysis, stereoselective synthesis, and chiral

chromatography.⁴¹ Therefore, it is surprising that the knowledge about the interactions with surfaces of supports like silica or activated carbon is rather limited. In fact, up to now, there is only little intrinsic understanding of the behavior of ferrocene on the surface within the pores of silica and other adsorbents.³¹⁻³³ On the other hand, the molecular dynamics of ferrocene as a guest molecule in inclusion compounds has been well studied by Mößbauer and NMR spectroscopy.^{42,43} For example, according to the ¹H line shape analysis and ¹H spin-lattice relaxation time measurements, ferrocene molecules, included in the structure of β -cyclodextrin, experience fast C₅ rotations of the Cp rings at the very low activation energy of $E_a = 0.8$ kcal/mol.⁴³ However, the overall isotropic reorientation of the ferrocene requires a much higher activation energy ($E_a = 10.7$ kcal/mol).⁴³ In contrast to such inclusion compounds, no details about reorientations of surface-adsorbed ferrocene molecules are known yet. Only isotropic reorientation has been described qualitatively at room temperature for ferrocene on silica^{31,33} and activated carbon.³² Therefore, in this contribution we study the interactions of ferrocene molecules with silica and activated carbon surfaces and their dynamic behavior quantitatively.

In this chapter, we applied variable temperature ¹³C and ²H solid-state NMR^{19,25,27,38,39} and T₁ relaxation time measurements¹⁹ to investigate the behavior of ferrocene (Cp₂Fe, (C₅H₅)₂Fe) (**1**) and its deuterated derivative, Cp₂Fe-*d*₂ (C₅H₄D)₂Fe) (**2**), in pores of silica (SiO₂) and activated carbon (AC) on the molecular scale. Using different support materials provides a deeper insight into the adsorption process itself and the ensuing mobilities of the surface species. These quantitative studies are of fundamental interest

and have wide ranging potential in fields such as catalysis, electronic devices and the separation sciences.

Results and Discussion

In this chapter, we sought to investigate the interactions of ferrocene with different support surfaces and their molecular dynamics quantitatively by solid-state NMR spectroscopy. A densely packed monolayer corresponds to 100% surface coverage. The amounts of ferrocene necessary to achieve this coverage have been determined earlier for the silica²⁸ and carbon²⁵ brands used here. In the following we report the quantitative study of a silica sample with a 75% sub-monolayer surface coverage with ferrocene (**1-75%-SiO₂**) and an activated carbon sample with a 75% surface coverage (**1-75%-AC**). Deuterium labeled ferrocene **2** has been investigated in samples with a 50% and 130% surface coverage (**2-50%-AC** and **2-130%-AC**).

Unfortunately, IR spectroscopy is not a viable method to study dynamic effects.⁴⁰ Ferrocene also does not have strong and characteristic Raman or IR bands⁴¹⁻⁴³ that would lie outside of the region where intensive and broad absorption bands of the support materials reside.^{44,45} For example, the prominent ferrocene bands (811, 1002, 1108, 1411, 3085 cm⁻¹)⁴² overlap with the broad and intensive bands of activated carbon (800-1450, 3000-3600 cm⁻¹).^{44,45}

However, solid-state NMR^{19,20} can be successfully applied to quantitatively characterize various molecular motions, when the reorientations in the magnetic field

occur on the T_2 and/or T_1 relaxation time scale. The first case is based on temperature-dependent signal line shapes of target nuclei. In the second case relaxation time measurements can be used because the molecular reorientations correspond to the Larmor frequencies of the nuclei.

Some ^{13}C T_1 spin-lattice relaxation time measurements, carried out for samples of solid ferrocene and also for materials containing intercalated ferrocene molecules, have been reported previously.⁴⁶⁻⁴⁸ It has been well established that the ^{13}C T_1 relaxation times of ferrocene molecules are controlled by very fast reorientations of the Cp rings, recognized as C_5 rotations with very low activation energy.³⁷ Therefore, these internal rotations can only be quantitatively characterized on the ^{13}C T_1 NMR time scale at extremely low temperatures. In fact, solid ferrocene shows a ^{13}C T_1 time temperature dependence, where a ^{13}C $T_{1\text{min}}$ time is observed at 110 K,⁴⁶ corresponding to an activation energy between 1.8 and 2.3 kcal/mol. Since the carbon spin-lattice relaxation times in solid ferrocene at room temperature and also at moderate temperatures are very long, they require long measurement times. This is not feasible for the characterization of our dilute samples that contain ferrocene only in sub-monolayer quantities. Furthermore, as mentioned above, the ^{13}C relaxation mechanism and its characteristics are already known for ferrocene-containing materials. Therefore, in this chapter we focus on the variable-temperature ^{13}C and ^2H solid-state NMR spectra, while the T_1 time measurements have been used only as diagnostic tests.

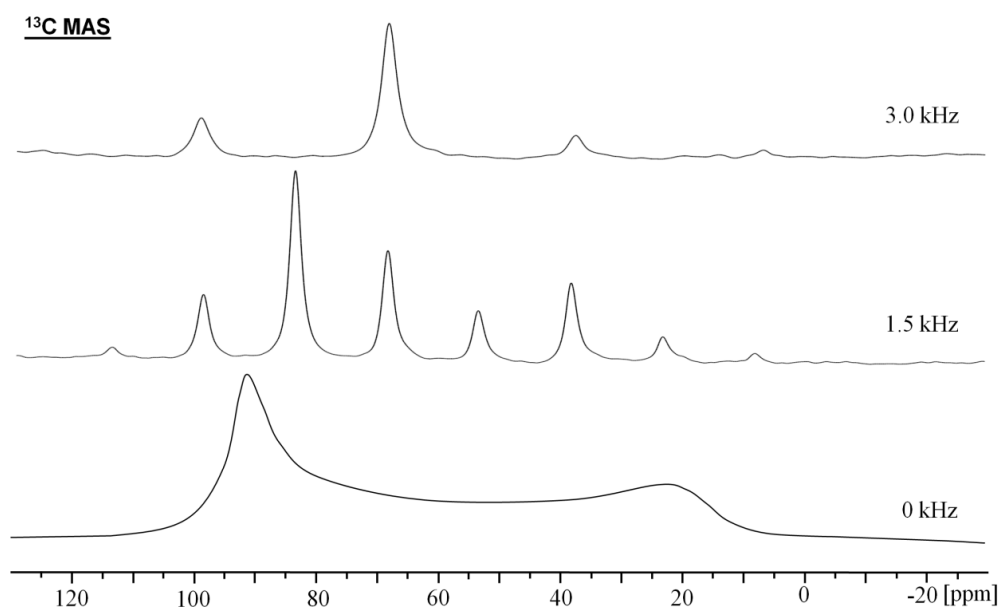


Figure 18. Room temperature $^{13}\text{C}\{^1\text{H}\}$ NMR spectra of polycrystalline ferrocene (**1**) at the indicated MAS spinning speeds. Reprinted with permission from *Organometallics* **2020**, *39*, 1080-1091. Copyright 2020 American Chemical Society.

Figure 18 shows the $^{13}\text{C}\{^1\text{H}\}$ MAS and static NMR spectra of polycrystalline ferrocene (**1**), recorded for comparison with the spectra of ferrocene molecules adsorbed on the surfaces in pores of the support materials. The static $^{13}\text{C}\{^1\text{H}\}$ NMR spectrum manifests a typical axially-symmetric CSA (chemical shift anisotropy) pattern,^{19,20} characterized by the parameters summarized in Table 6. Processing of the MAS NMR spectra led to parameters that are in excellent accordance with the theoretical and experimental studies of solid **1**.⁴⁹ Based on these studies, the static ^{13}C CSA pattern belongs to ferrocene molecules with the Cp rings rapidly rotating about their 5-fold symmetry axis. At this point it is important to emphasize that the Cp rings in solid **1** are magnetically equivalent.

Due to the fast Cp ring rotation, the ^2H NMR spectrum of static **2** shows the quadrupolar Pake pattern^{19,25,27,38,39} with a quadrupolar splitting of 72 kHz (Figure 19).

The fitting procedure (insert in Figure 2) leads to the ^2H isotropic chemical shift δ_{iso} , which is set to 0 ppm, and a quadrupolar constant C_Q of 98 ± 2 kHz with an asymmetry parameter of $\eta = 0.021$. These parameters agree well with those reported earlier.^{25,50} As follows from the spectral data, the character of the dynamics of **2** does not change with temperature.

Table 6. ^{13}C isotropic chemical shifts δ_{iso} and CSA parameters (CSA $\Delta\sigma$ and asymmetry parameter η) derived from the $^{13}\text{C}\{^1\text{H}\}$ MAS and static NMR experiments carried out for **1**, **1-75%-SiO₂** and **1-75%-AC**. Reprinted with permission from *Organometallics* **2020**, *39*, 1080-1091. Copyright 2020 American Chemical Society.

Sample	δ_{iso} (ppm)	$\Delta\sigma$ (ppm)	T (K)
1	68.6	-54 ± 2 ; $\eta = 0$	298
1-75%-SiO₂	69.9	0	298
	68.4	-52 ± 2.0 ; $\eta = 0.05$	180
1-75%-AC	68.1	0	298
	68.5	~ -55 ; $\eta = 0.2$	183

Material **1-75%-SiO₂** has been prepared by grinding the corresponding amount of **1** with silica (see Experimental Section). This procedure could potentially change the structure of the host material. Therefore, ^{29}Si solid-state NMR spectra have been measured before and after grinding. Figure 20 shows the $^{29}\text{Si}\{^1\text{H}\}$ MAS NMR spectra recorded for pristine silica and material **1-75%-SiO₂**. Both spectra look practically identical and they exhibit two poorly resolved ^{29}Si resonances at -103 and -112 ppm, representing $\text{SiO}_3(\text{OH})$

and SiO_4 structural units¹⁹ in about the same ratio. Therefore, a chemical reaction of **1** with the silica support, or a major structural change can be ruled out.

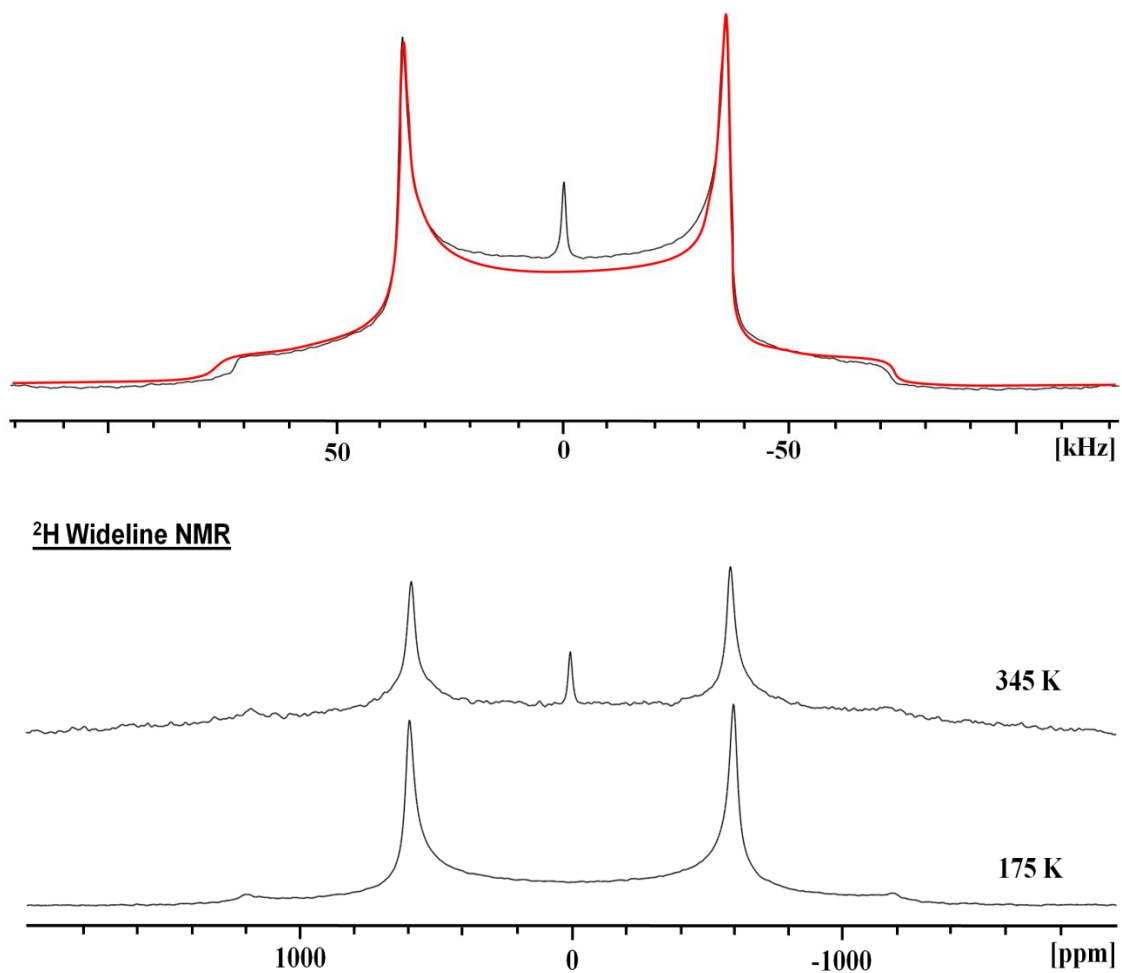


Figure 19. Static ^2H NMR of **2** at 345 K and 175 K. The top spectrum shows the experimental and simulated static spectra at 295 K; the sharp signal in the center is an artefact appearing often in solid-echo experiments. Reprinted with permission from *Organometallics* **2020**, 39, 1080-1091. Copyright 2020 American Chemical Society.

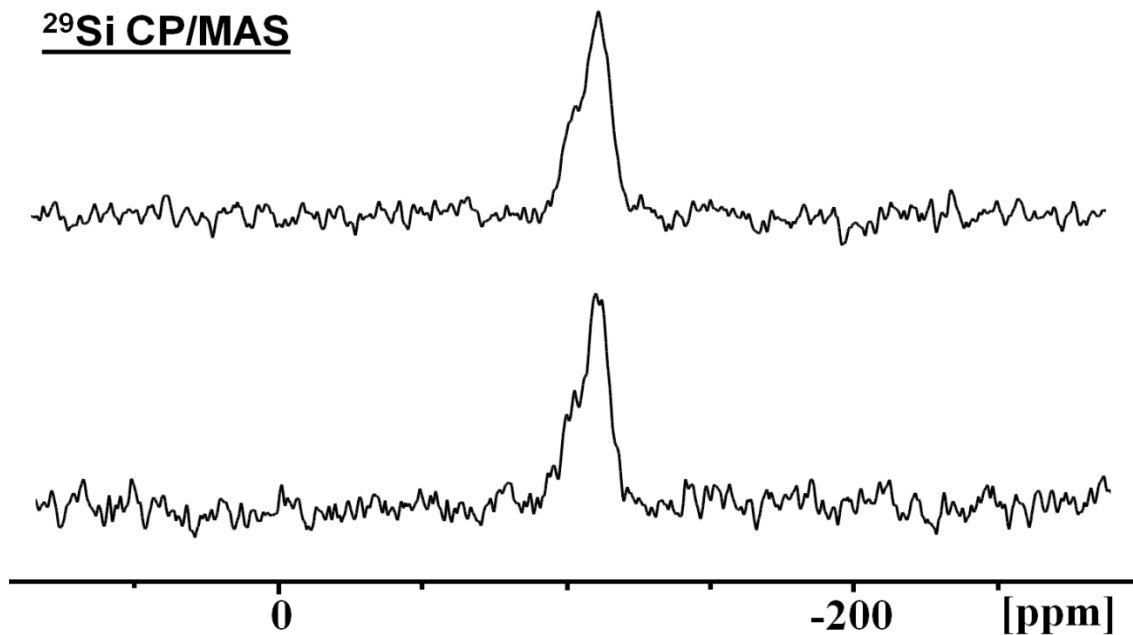


Figure 20. $^{29}\text{Si}\{^1\text{H}\}$ MAS NMR spectra of pristine dried silica (top) and **1-75%- SiO_2** (bottom), recorded at room temperature with a spinning rate of 3.1 kHz. Reprinted with permission from *Organometallics* **2020**, 39, 1080-1091. Copyright 2020 American Chemical Society.

The static variable temperature $^{13}\text{C}\{^1\text{H}\}$ NMR spectra of material **1-75%- SiO_2** , recorded at intervals of 10 K between 295 and 180 K, are presented in Figure 21. The evolution of the signal shapes with the temperature is fully reversible. In accordance with data reported earlier for ferrocene in silica²⁴ and ferrocene inclusion compounds,^{36,37} at ambient and moderately lower temperatures the spectrum manifests a sharp Lorentz-shaped resonance for the Cp rings at about 68 ppm. This feature demonstrates that an isotropic liquid-like reorientation of ferrocene in the pores of material **1-75%- SiO_2** takes place. The isotropic reorientation effectively averages out the CSA.

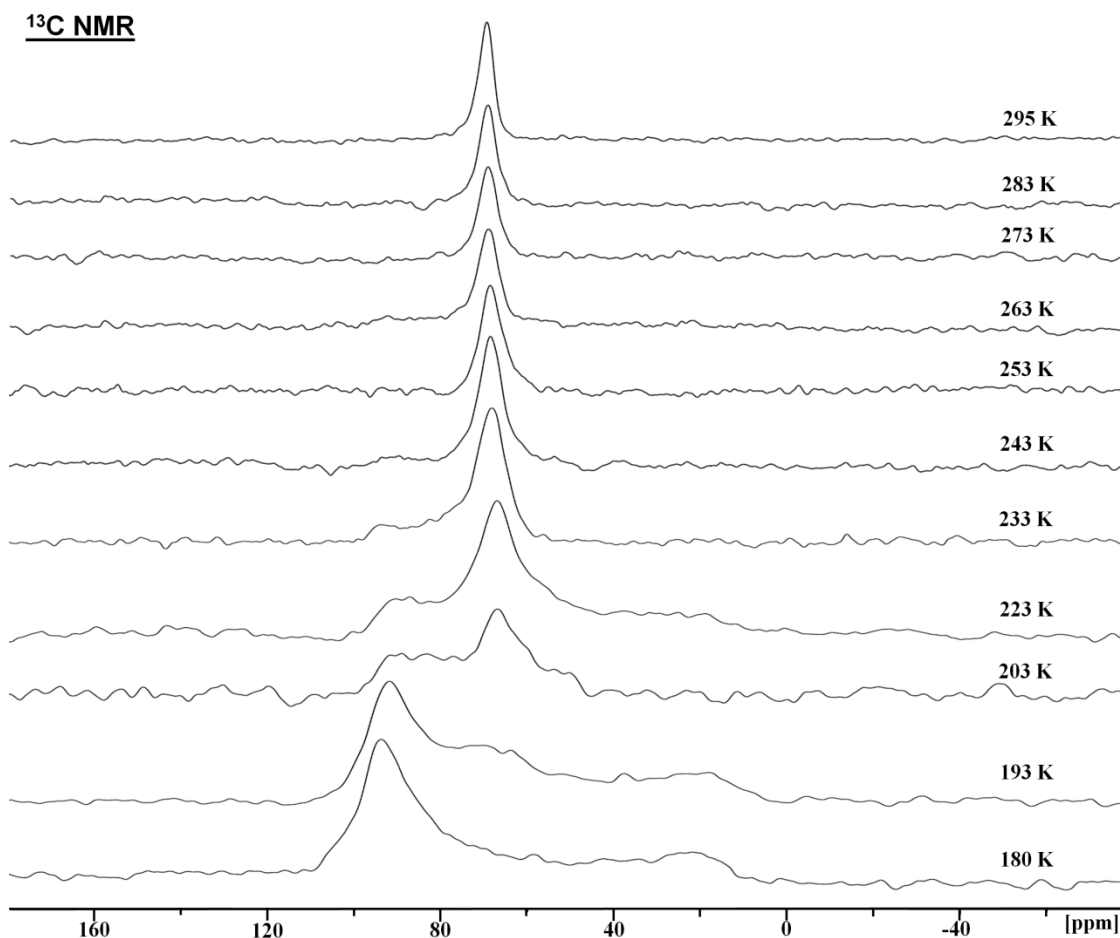


Figure 21. $^{13}\text{C}\{^1\text{H}\}$ NMR spectra of the static sample **1-75%-SiO₂** recorded at the indicated temperatures. Reprinted with permission from *Organometallics* **2020**, *39*, 1080-1091. Copyright 2020 American Chemical Society.

Based on this fact, and in contrast to inclusion compounds studied earlier,^{6,37,47} which contain a single ferrocene molecule in the structural unit, two different motional modes can be suggested for interpreting the sharp carbon resonance in the $^{13}\text{C}\{^1\text{H}\}$ NMR spectra (Figure 21). The first model (Figure 22, **A**) corresponds to the ferrocene motions occurring along the pore surface and can be imagined as a "tumbleweed scenario". Here, the bound horizontal molecular state of the ferrocene transforms to the vertical state and back again to the horizontal state. In combination with the Cp rotations around the C₅ symmetry axis,

these motions will imitate isotropic reorientations. It should be noted that recently both molecular orientations have been found for ferrocene, physically adsorbed on a metal surface, by low temperature scanning tunneling microscopy and density functional theory calculations.⁵¹ The second model (Figure 22, **B**) corresponds to a chemical exchange between the bound horizontal state (see below) and truly isotropically moving ferrocene molecules.

The choice between the models **A** and **B** for the mobility of **1** on the surface can be made by considering the temperature-dependent $^{13}\text{C}\{^1\text{H}\}$ NMR spectra in Figure 4. Upon cooling, the sharp carbon resonance experiences an evolution to show the axially symmetric CSA pattern at 180 K, belonging to immobile ferrocene molecules. As follows from the data reported in Table 1, the CSA parameters of this pattern and **1** at 298 K (Figure 18) are practically identical. Thus, surface-bound ferrocene molecules also experience the fast Cp rotations around the C_5 symmetry axis.

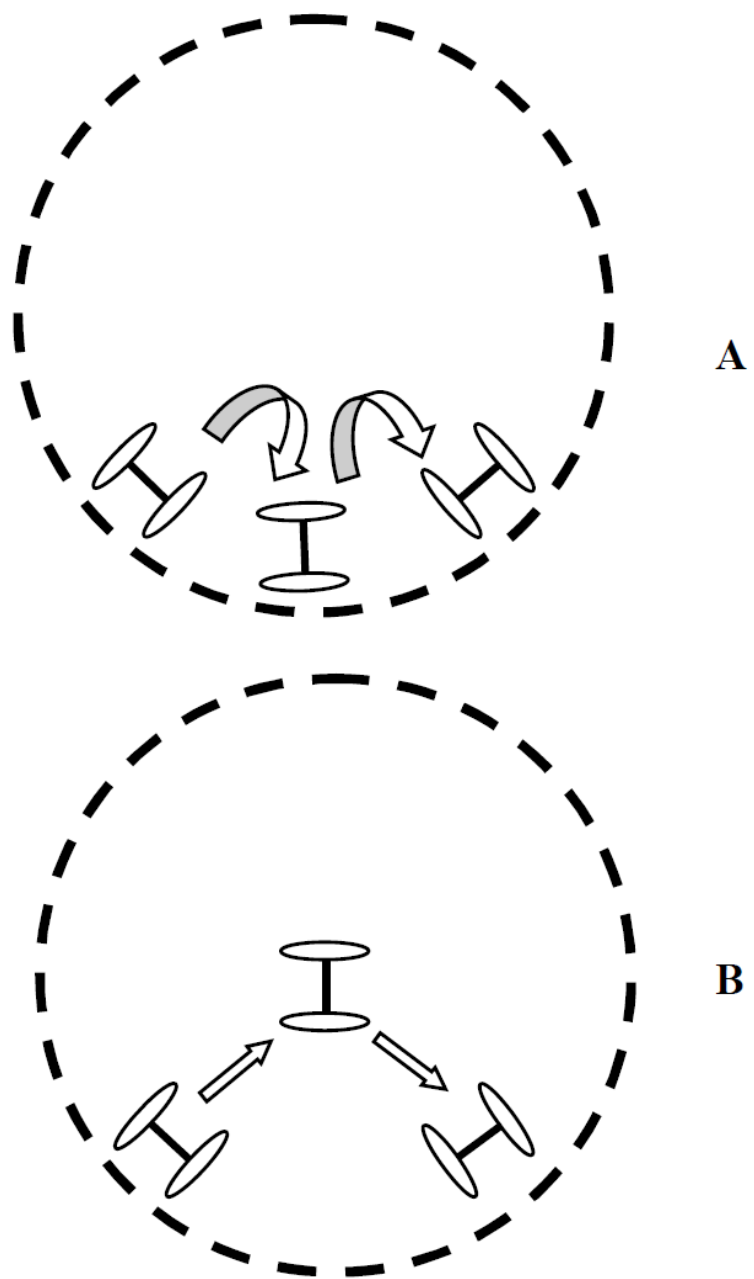


Figure 22. Two potential motional modes leading to a sharp carbon resonance of ferrocene in **1-75%-SiO₂**. The broken line circles indicate the surface of idealized pores of the support. Reprinted with permission from *Organometallics* **2020**, *39*, 1080-1091. Copyright 2020 American Chemical Society.

The following spectral features in Figure 21 are important in the context of the motional models described above (Figure 22). **(a)** The CSA pattern and the isotropic line co-exist at low temperatures. This is especially obvious in the spectra recorded at 223, 203, and 193 K. **(b)** The resonances show chemical exchange between them on the NMR time scale, as evidenced by the reversibility of the signal evolution. **(c)** The linewidth and shape of the narrow resonance does not change when cooling the sample, while the CSA pattern of a distinct separate signal appears. This again speaks for a slow exchange between the isotropic and bound states that occurs on the NMR time scale and allows van't Hoff analyses (see below). This result is only compatible with model **B** (Figure 22), as model **A** would lead to one averaged signal that broadens gradually upon cooling. The analogous interpretation accounts for the results of the variable temperature ^2H NMR spectra discussed below. **(d)** The relative populations of the resonances change with the temperature. In addition, a single ferrocene- d_5 molecule, included into a thiourea matrix,⁴² does not show the temperature evolution of the ^2H resonance between 221 and 172 K, corresponding to motions of the ferrocene molecule itself, on the NMR time scale. Thus, the experimental data only support the motional model **B** well (Figure 22).

Several $^{13}\text{C}\{^1\text{H}\}$ MAS NMR experiments were performed with different spinning speeds for **1-75%-SiO₂** at 180 K (Figure 23). As can be deduced from the MAS spectra, one single isotropic ^{13}C resonance is observed at 180 K, corresponding to both magnetically equivalent Cp rings. In accordance with this observation, the simulation of the CSA pattern in the insert of Figure 5 can be reached only by assuming the presence of one single Cp resonance. Assuming a vertical orientation of the surface-attached ferrocene

molecules, the π -electrons of one of the Cp rings are supposed to interact with the surface of silica, leading to non-equivalency of the Cp rings in the $^{13}\text{C}\{^1\text{H}\}$ MAS NMR spectra.

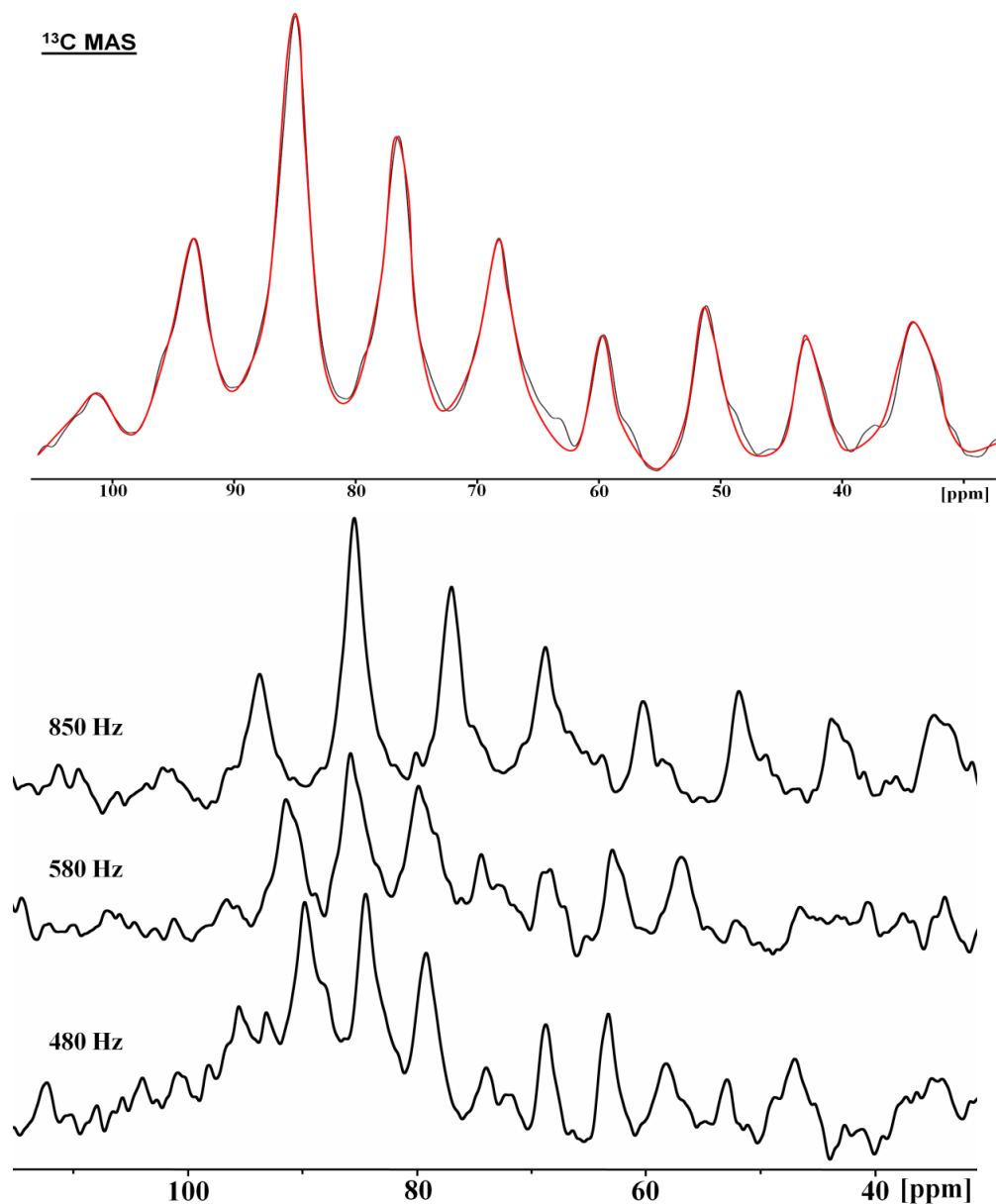


Figure 23. $^{13}\text{C}\{^1\text{H}\}$ MAS NMR spectra of **1-75%-SiO₂** recorded at 180 K with the indicated spinning speeds. The top spectrum shows the simulation of the spectrum obtained at 850 Hz, corresponding to the CSA parameters given in Table 1. Reprinted with permission from *Organometallics* **2020**, *39*, 1080-1091. Copyright 2020 American Chemical Society.

Both Cp rings in vertical molecular states could in principle participate in this interaction if the pore size of the silica were only about 7-9 Å. This would be in the range of the height of ferrocene, which is 6.7 Å, when the Van Der Waals radii of the carbon atoms are included. However, the average pore diameter of the silica used is 40 Å.

Therefore, due to the equivalency of the Cp rings in the $^{13}\text{C}\{^1\text{H}\}$ NMR spectrum of **1-75%-SiO₂** at 180 K, the horizontally oriented molecular states are much more likely. Finally, since the isotropically moving component is completely absent in the $^{13}\text{C}\{^1\text{H}\}$ NMR spectra at 180 K (Figure 21), these horizontally oriented states of ferrocene molecules, interacting with the surface of silica within the pores, are most thermodynamically stable.

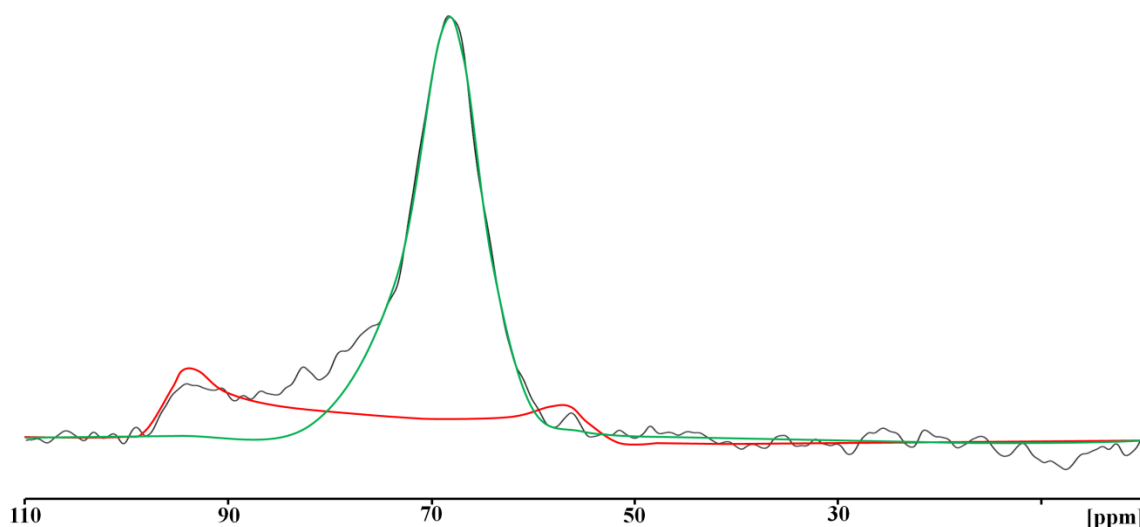


Figure 24. Simulation of the $^{13}\text{C}\{^1\text{H}\}$ NMR spectrum of **1-75%-SiO₂** at 233 K. The large isotropically moving component is represented by the green line, the low intensity CSA pattern of the surface-attached ferrocene molecules is drawn in red. Reprinted with permission from *Organometallics* **2020**, *39*, 1080-1091. Copyright 2020 American Chemical Society.

As seen in Figure 21, the signal intensity of the isotropic component increases with the temperature. The experimental and simulated $^{13}\text{C}\{^1\text{H}\}$ NMR spectra of **1-75%-SiO₂** at 233 K are shown in Figure 24. From these, the mole fractions of both components can be determined by deconvolution. Using this approach, the fractions of the surface-attached molecules (P_{bound}) and the isotropically moving molecules (P_{iso}), found between 193 and 233 K, lead to the calculated equilibrium constants ($K_{\text{eq}} = P_{\text{iso}}/P_{\text{bound}}$). The latter, summarized in Table 7, describe the transformation of bound to isotropically moving molecules. Then, the slope of the dependence of $\ln(K_{\text{eq}})$ versus $1/T$ (Figure 7) allows to determine the enthalpy that characterizes the ferrocene/silica surface interactions via the adsorption enthalpy of **1**, which can be calculated as $\Delta H^0 = -6.7 \pm 0.5$ kcal/mol with a ΔS° of $+30 \pm 2$ e.u. It should be noted at this point that the positive entropy change corresponds well to the increased randomness of the isotropic state.

Table 7. Temperature dependence of the mole fractions found for isotropically moving molecules of **1** (P_{iso}) and surface-bound molecules (P_{bound}) in **1-75%-SiO₂** and the corresponding equilibrium constants K_{eq} . Reprinted with permission from *Organometallics* **2020**, 39, 1080-1091. Copyright 2020 American Chemical Society.

T (K)	P_{iso}	P_{bound}	K_{eq}
193	0.0898	0.9102	0.0987
203	0.28	0.72	0.389
223	0.405	0.595	0.6807
233	0.763	0.237	3.219

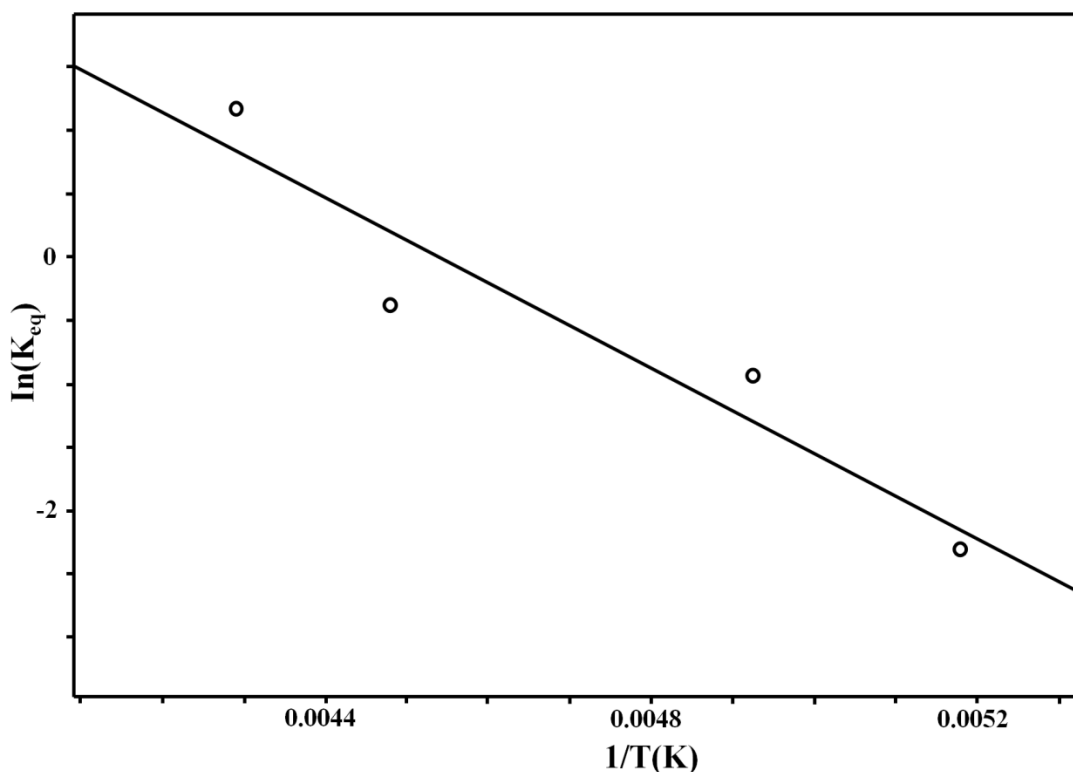


Figure 25. Temperature dependence of the equilibrium constant (K_{eq}) depicted as $\ln(K_{eq})$ versus $1/T$, obtained for the sample **1-75%-SiO₂**. Reprinted with permission from *Organometallics* **2020**, 39, 1080-1091. Copyright 2020 American Chemical Society.

As outlined above, the static $^{13}\text{C}\{^1\text{H}\}$ NMR resonances in Figure 16 show chemical exchange between the surface-attached and isotropically moving molecules of **1** within the silica pores, taking place on the T_2 NMR time scale. A quantitative line shape analysis in these spectra is obviously difficult. However, the ^{13}C line shape observed at 223 K provides an estimate of the rate constant k_{exch} as $19 \cdot 10^3 \text{ s}^{-1}$ within the limits of a three-center exchange. This value then gives a $\Delta G(223\text{K})^\ddagger$ of 6.1 kcal/mol for the exchange.

In principle, the ^{13}C NMR signal obtained at 180 K (Figure 21) could also stem from recrystallized **1** instead of molecules attached to the silica surface. The values in Table 6

show that the ^{13}C NMR parameters of polycrystalline **1** and surface-attached ferrocene molecules in **1-75%-SiO₂** are practically the same. Therefore, regarding only adsorption on one support material, there is no strong evidence that the immobile molecules are indeed located on the surface within the pores of silica, and not in crystallized **1**. However, independent evidence and clarification regarding the different scenarios can be obtained by probing material **1-75%-AC** because activated carbon, being paramagnetic, is active in EPR spectroscopy.^{11,52,53} In accordance with the paramagnetic nature of this support, the ^{13}C T_1 times determined for the Cp rings in a static sample of **1-75%-AC** are extremely short with 0.05 s (298 K), 0.06 s (283 K), and 0.06 s (273 K). In comparison, the ^{13}C T_1 relaxation times are longer than 18 s in polycrystalline **1**. Therefore, it can be assumed that the Cp rings are in contact with the surface of the activated carbon support.

The temperature evolution of the $^{13}\text{C}\{^1\text{H}\}$ NMR resonances in the spectra of static **1-75%-AC** (Figure 26) is similar to that observed for **1-75%-SiO₂**. At the static regime the ^{13}C resonance of the activated carbon support is very broad and it can be eliminated by a baseline correction. In analogy to the case of **1** on silica, the isotropic resonance of ferrocene in **1-75%-AC**, observed at 298 K with the chemical shift reported in Table 1, transforms to the CSA pattern at 183 K. However, in contrast to **1-75%-SiO₂**, the pattern is broadened significantly. In fact, the simulation of this CSA pattern (Figure 26, top) requires now a linewidth larger than 1.2 kHz with the parameters summarized in Table 1. This broadening is obviously caused by strong dipolar electron-nucleus interactions between **1** and the paramagnetic surface of the activated carbon, preventing a quantitative analysis of the spectra. This problem can be avoided by studying material **2-50%-AC**,

containing a deuterium label, which is less sensitive to paramagnetic effects. Figure 27 shows the variable temperature ^2H NMR spectra obtained from a static sample of **2-50%-AC**.

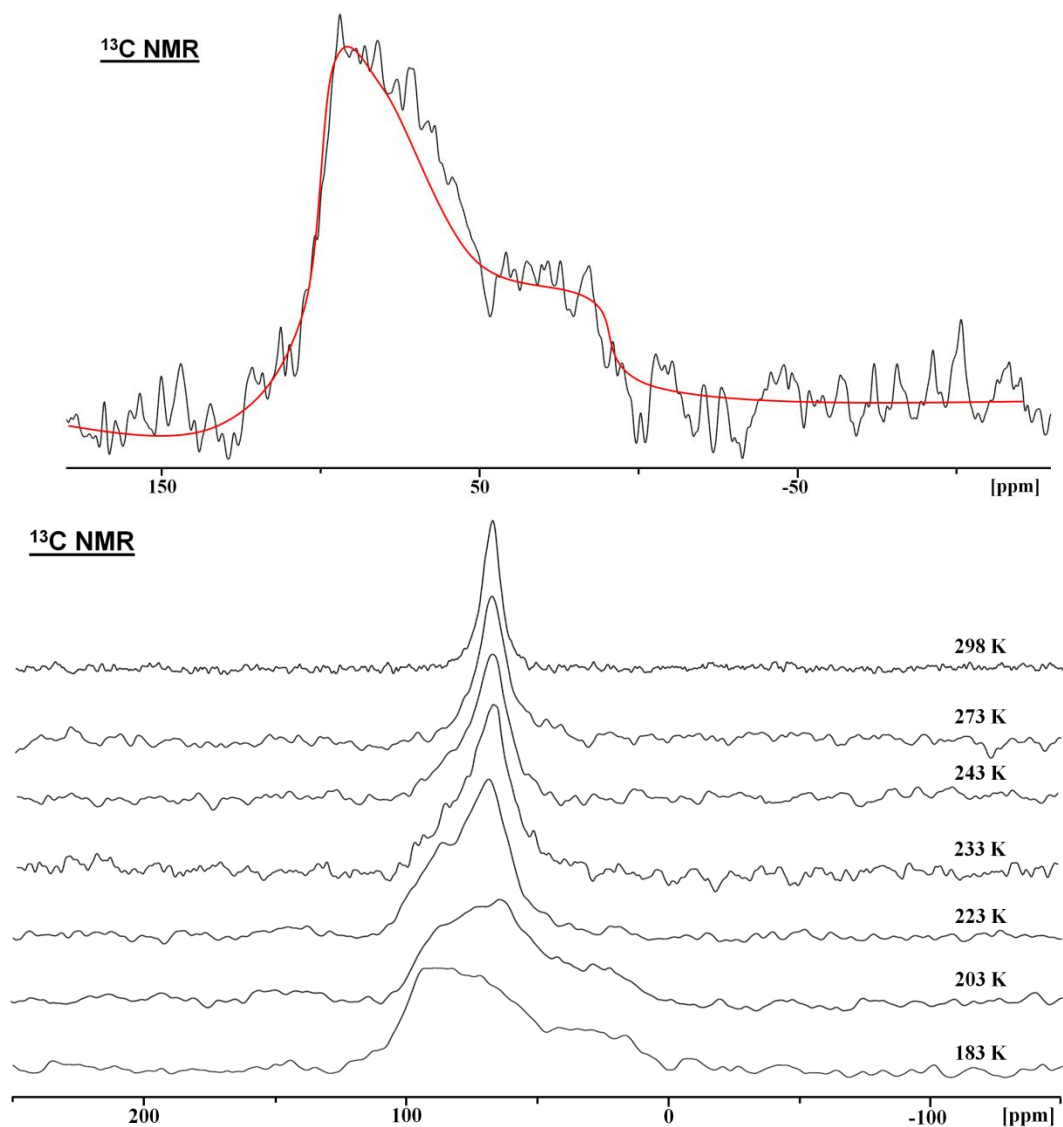


Figure 26. Variable temperature $^{13}\text{C}\{^1\text{H}\}$ NMR spectra of a static sample of **1-75%-AC** at the indicated temperatures. The top trace shows the CSA simulation of the signal at 183 K. Reprinted with permission from *Organometallics* **2020**, *39*, 1080-1091. Copyright 2020 American Chemical Society.

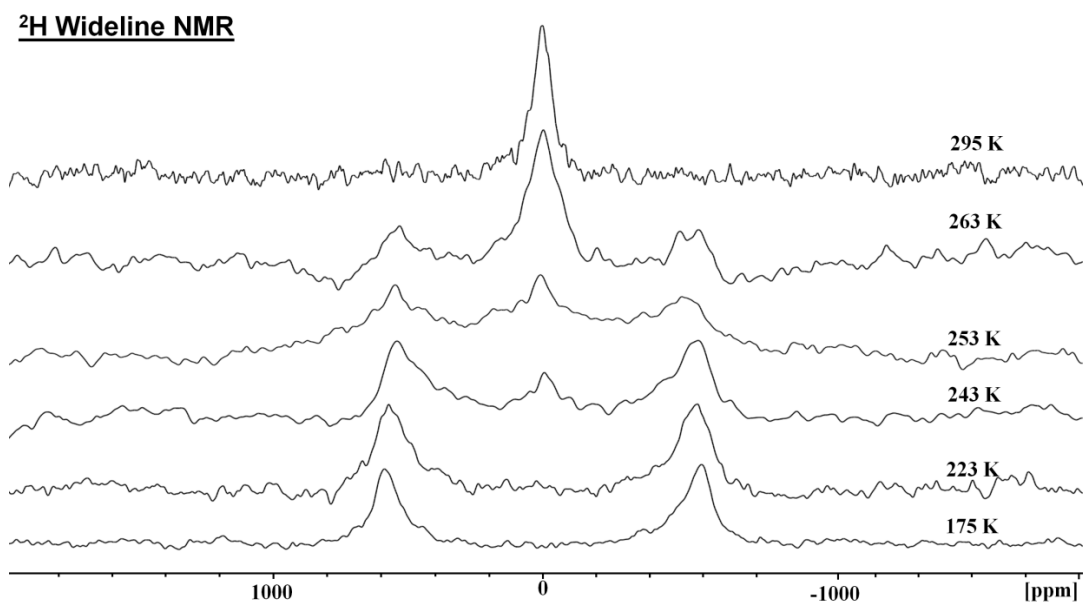


Figure 27. Variable temperature ²H NMR spectra of a static sample of **2-50%-AC** recorded at the indicated temperatures. Reprinted with permission from *Organometallics* **2020**, *39*, 1080-1091. Copyright 2020 American Chemical Society.

In accordance with the ¹³C NMR data in Figure 27, the spectrum exhibits a single deuterium resonance at 295 K, belonging to isotropically moving ferrocene molecules. Upon cooling, this resonance turns into a quadrupolar pattern¹⁹ similar to that of solid **2** in Figure 19, which can be simulated with the quadrupolar parameters $C_Q = 98 \pm 3$ kHz and $\eta = 0.08$. The same pattern, observed at low temperatures, has been reported for deuterated ferrocene (C₅D₅)₂Fe placed into a thiourea matrix.³⁶ In analogy to the case of **2**, the low temperature quadrupolar pattern of **2-50%-AC** does not show features that could be interpreted as non-equivalency of the Cp rings. Thus, the vertical molecular stance of ferrocene on the activated carbon surface is not probable. The line broadening in the ²H

low temperature spectrum (Figure 22) is most likely due to interactions with electrons of the paramagnetic activated carbon support, as described above for the ^{13}C nuclei.

The variable temperature ^2H NMR spectra of **2-50%-AC** in Figure 27 demonstrate the absence of the isotropic component at 175 K, which grows gradually, however, upon heating the ^2H NMR spectrum, recorded at 263 K and simulated as a superposition of the quadrupolar pattern and the isotropic component, is illustrated in Figure 28. It should be noted that this simulation requires the linewidth of both components to be 5.5 kHz versus 1 kHz used for the FID treatment. As in the case of the $^{13}\text{C}\{^1\text{H}\}$ NMR spectra of **1-75%-SiO₂**, deconvolution leads to mole fractions of the isotropically moving ferrocene molecules (P_{iso}) and surface-attached molecules (P_{bound}). These give, in turn, the equilibrium constants $K_{\text{eq}} = P_{\text{iso}}/P_{\text{bound}}$ summarized in Table 8.

Table 8. Temperature dependent mole fractions of isotropically moving ferrocene molecules (P_{iso}) and surface-attached molecules (P_{bound}) and the corresponding equilibrium constants K_{eq} , determined for **2-50%-AC**. Reprinted with permission from *Organometallics* **2020**, 39, 1080-1091. Copyright 2020 American Chemical Society.

T (K)	P_{iso}	P_{bound}	K_{eq}
243	0.078	0.922	0.085
247	0.11	0.89	0.124
253	0.1456	0.854	0.171
263	0.25	0.75	0.33

Comparing the values in Table 8 with those in Table 7 clearly indicates the difference between the silica versus the activated carbon support. For example, the $K_{eq} = P_{iso}/P_{bound}$ for ferrocene adsorbed on silica at 233 K equals 3.2 (Table 2), while it is 0.085 for activated carbon as the support at 243 K (Table 8). In spite of the small temperature difference, K_{eq} is orders of magnitude larger for silica than for the activated carbon sample.

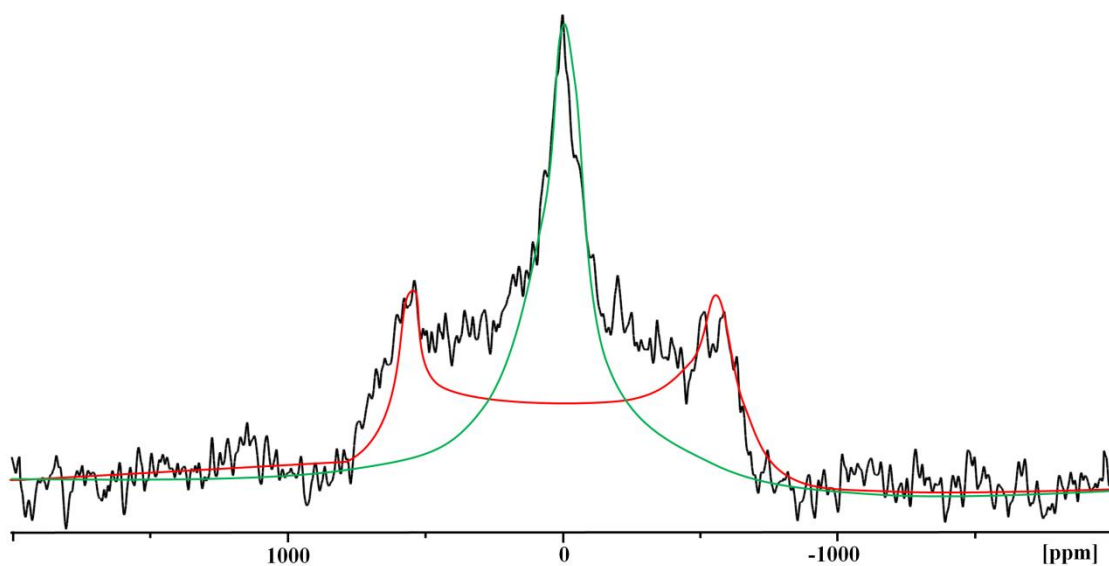


Figure 28. Static ^2H NMR spectrum of **2-50%-AC** at 263 K. The red line shows the simulation of the quadrupolar pattern with $C_Q = 97$ kHz and $\eta = 0.08$, the green line depicts the isotropic component. Reprinted with permission from *Organometallics* **2020**, 39, 1080-1091. Copyright 2020 American Chemical Society.

The straight line in coordinates $\ln(K_{eq})$ versus $1/T$ in Figure 29 leads to the adsorption enthalpy of ferrocene molecules in **AC**, ΔH^0 of -8.4 ± 1.0 kcal/mol and a ΔS° value of 30 ± 3 e.u. Finally, the additional line broadening, found at the simulation of the spectrum in Figure 28, is most likely caused by a chemical exchange between surface-

attached and isotropically moving molecules in material **2-50%-AC**. This exchange, resulting in the single sharp resonance in the room temperature ^2H NMR spectrum, could be characterized by the rate constant k_{exch} of $145 \cdot 10^3 \text{ s}^{-1}$ at 263 K within the limits of a three-center exchange, giving $\Delta G(263\text{K})^\ddagger = 6.2 \text{ kcal/mol}$. This value is close to the 6.1 kcal/mol obtained for material **1-75%-SiO₂**.

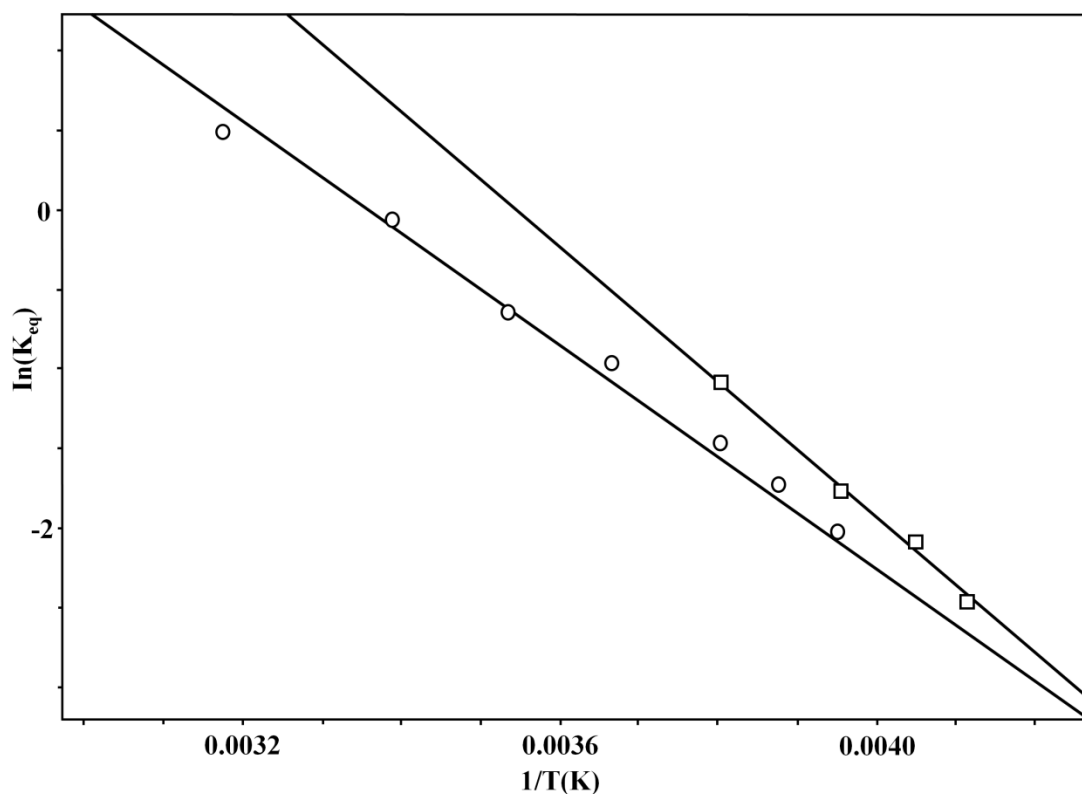


Figure 29. Temperature dependence of the equilibrium constant K_{eq} depicted as $\ln(K_{\text{eq}})$ versus $1/T$, obtained from the samples **2-50%-AC** (\square) and **2-130%-AC** (\circ). Reprinted with permission from *Organometallics* **2020**, 39, 1080-1091. Copyright 2020 American Chemical Society.

In the context of the presented study, material **2-130%-AC**, prepared with a 130% coverage of the surface, was of great interest. Figure 30 shows the room temperature $^{13}\text{C}\{^1\text{H}\}$ MAS NMR spectrum of this material, recorded with a spinning speed of 9 kHz. The broad resonance at 129 ppm can be attributed to carbons nuclei of the activated carbon support,¹¹ while the relatively sharp line belongs to the Cp rings of **2**. As in the case of **1-75%-AC**, the ^{13}C T_1 time of the Cp ring carbon nuclei is only 0.056 s, which is close to the value of 0.08 s measured for the carbons of activated carbon.¹¹ The extremely fast relaxation of the Cp rings in **2-130%-AC** supports again the assumption that ferrocene molecules are actually located in the pores of this paramagnetic material in spite of being present in excess of a monolayer in the sample. The variable temperature ^2H NMR spectra of the static sample **2-130%-AC** (Figure 31) overall resemble those displayed in Figure 27. Nevertheless, the following features deserve additional attention.

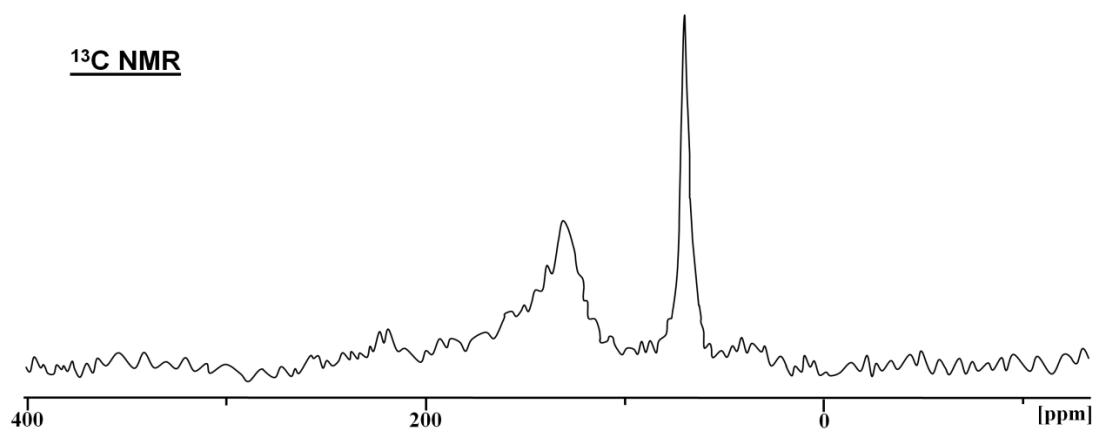


Figure 30. $^{13}\text{C}\{^1\text{H}\}$ MAS NMR spectrum of **2-130%-AC** at a spinning speed of 9 kHz. Reprinted with permission from *Organometallics* **2020**, *39*, 1080-1091. Copyright 2020 American Chemical Society.

First, even at 315 K, the ^2H NMR spectrum exhibits the low-intensity pattern with a quadrupolar splitting, corresponding to surface-attached ferrocene molecules or polycrystalline **2** (see Figure 19), located within the pores of the support. Note that this quadrupolar pattern is especially visible in the form of sidebands in the ^2H MAS spectrum of **2-130%-AC** (Figure 31, top). *Second*, in contrast to the ferrocene in material **2-50%-AC** with a sub-monolayer of **2**, the chemical exchange between liquid-like molecules and surface-bound molecules is slow on the NMR time scale. In the context of this exchange, this result is quite reasonable because decreasing the free space on the activated carbon pore surface by increasing the total amount of **2** will impede the exchange. *Third*, in spite of **2** being present in excess of a monolayer, the ^2H NMR spectra of **2-130%-AC** recorded at the lowest temperatures do not manifest the isotropic resonance. This effect can be attributed to the formation of a second layer of the ferrocene on the pore surface.

To determine the mole fractions of the isotropically moving ferrocene molecules (P_{iso}) and surface-attached molecules (P_{bound}) in **2-130%-AC**, we have used the approach described above for **2-50%-AC**. The fractions and equilibrium constants, defined again as $K_{\text{eq}} = P_{\text{iso}}/P_{\text{bound}}$, are summarized in Table 9. Figure 29 displays the corresponding correlation yielding the thermodynamic parameters ΔH^0 (-7.03 ± 0.6 kcal/mol) and ΔS° (36 ± 3 e.u.). The somewhat reduced adsorption enthalpy ΔH° when going from **2-50%-AC** to **2-130%-AC** can be explained by the formation of a second layer of **2** on the surface. One might speculate that two layers of ferrocene are, in a solid-state NMR sense, equivalent to polycrystalline **2** within the pores.

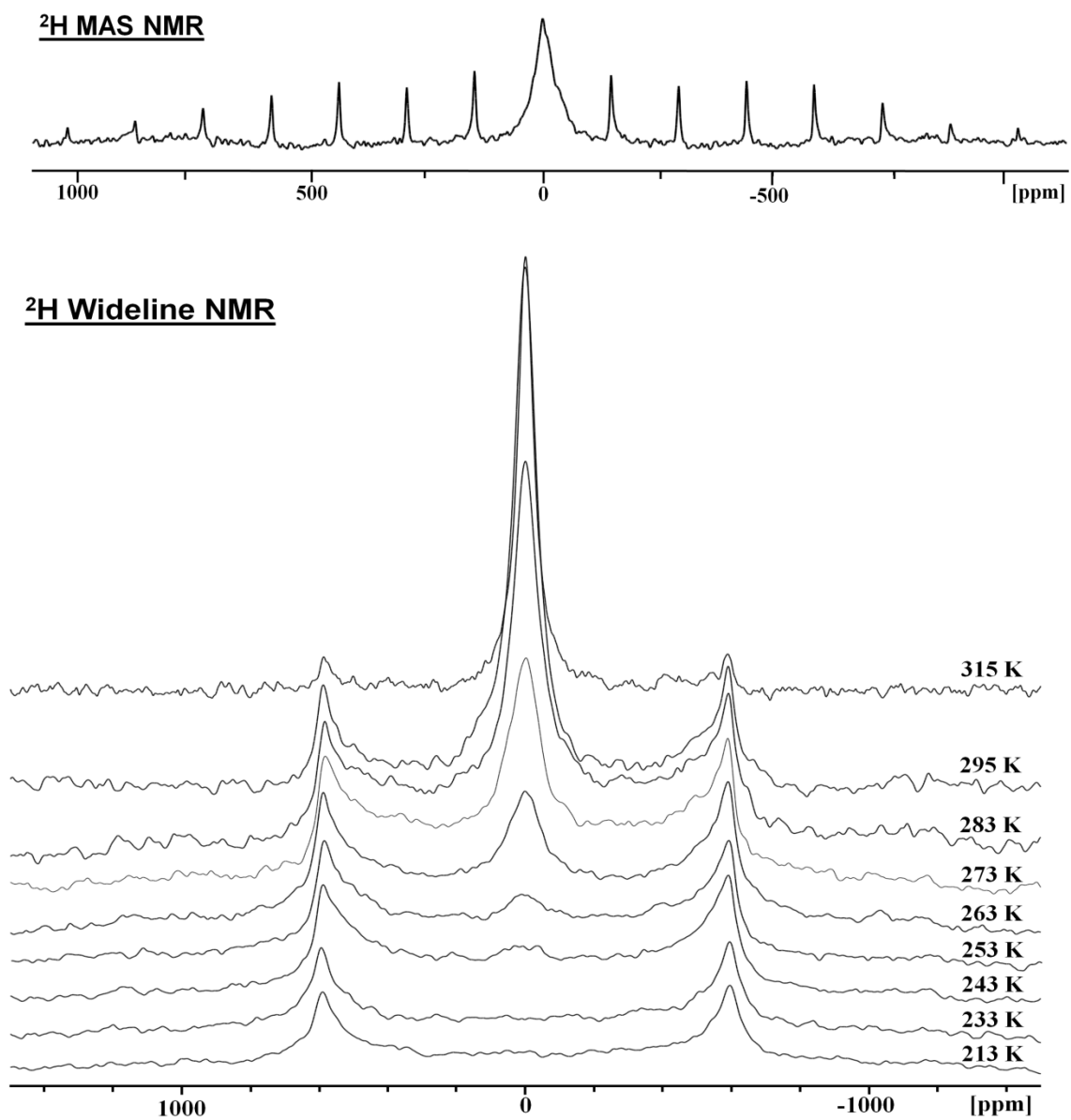


Figure 31. Variable temperature ^2H NMR spectra collected for a static sample of **2-130%-AC** at the indicated temperatures (bottom). Top spectrum: Room temperature ^2H MAS NMR of **2-130%-AC**, spinning at a rate of 9 kHz. Reprinted with permission from *Organometallics* **2020**, *39*, 1080-1091. Copyright 2020 American Chemical Society.

Table 9. Temperature dependent mole fractions of isotropically moving ferrocene molecules (P_{iso}) and surface-attached molecules (P_{bound}) and the corresponding equilibrium constants K_{eq} , determined for **2-130%-AC**. Reprinted with permission from *Organometallics* **2020**, 39, 1080-1091. Copyright 2020 American Chemical Society.

T (K)	P_{iso}	P_{bound}	K_{eq}
243	0.050	0.95	0.053
253	0.117	0.883	0.133
258	0.151	0.849	0.178
263	0.187	0.813	0.23
273	0.276	0.724	0.381
283	0.342	0.6584	0.519
295	0.484	0.516	0.9378
315	0.62	0.38	1.6316

Since the quadrupolar patterns of the individual deuterated ferrocene molecules in polycrystalline **2** and surface-attached molecules in **2-50%-AC** and **2-130%-AC** at low temperatures are practically identical, it was important to determine the difference between them by measuring the ^2H T_1 times in static samples of **2** and **2-130%-AC**. The ^2H NMR T_1 relaxation data obtained for **2** at different temperatures are 1.10 s (295 K), 0.70 s (263 K), 0.67 s (258 K), 0.39 s (213 K) and 0.15 s (185 K). To show that these values are correct, they have been presented as a correlation of $\ln(T_1)$ versus $1/T$, giving a straight line which corresponds to an activation energy of 1.9 kcal/mol for the relaxation process. Therewith, the activation energy lies in the region of 1.8 to 2.3 kcal/mol, reported

for the fast the C₅ rotation of the Cp rings.^{37,46} For a static sample of **2-130%-AC**, the ²H T₁ measurements were reliable at low temperatures, when only the quadrupolar signal was observed, resulting in the values 0.09 s (213 K) and 0.04 s (185 K). The T₁ measurement at 295 K was successful for a spinning sample of **2-130%-AC** by using the sideband pattern (Figure 31, top) to result in a ²H T₁ time of 0.35 s. Obviously, when going from **2** to **2-130%-AC**, the ²H T₁ time shortens significantly. This illustrates that dipolar electron-nucleus interactions between the ferrocene molecules and the paramagnetic surface of the activated carbon occur. We consider this effect as an additional proof that the ferrocene molecules reside on the surface within the pores of the activated carbon support.

Finally, a *fourth* feature in the ²H NMR spectra of **2-130%-AC** in Figure 13 deserves a more detailed discussion. The linewidth of the central, isotropic component of the spectrum is large, growing from 3.3 kHz at 315 K to 8.2 kHz at 273 K, while the quadrupolar pattern practically does not change. This ‘selective’ broadening is visible best in the MAS NMR spectrum (Figure 31, top), where the broadened isotropic line is observed in combination with the sideband pattern containing sharp lines. This feature has been noticed earlier²⁵ and attributed to the higher translational mobility of the adsorbed molecules of **2** upon heating the samples. However, the same spectroscopic effect can appear, when the isotropically moving molecules experience a very fast chemical exchange with additional molecular states, acting as intermediates in the slower exchange with the horizontally bound molecules. We suggest that the vertically oriented (semi-bound) molecules represent such intermediates. This explanation can be supported by the following observations. First, the broadening of the isotropic resonance does not show

quadrupolar features, which would appear in the case of slowing down translational motions at low temperatures. Second, the ^2H T_1 time of 0.021 s measured for the central component in the MAS spectrum (Figure 31) at 295 K cannot provide the experimentally observed line width of 4.3 kHz.

In summary, liquid-like behavior has been found for ferrocene molecules residing on silica and activated carbon surfaces within the pores. In both materials, the surface-attached adsorbed ferrocene molecules have been recognized as horizontally oriented thermodynamically stable states, experiencing fast rotations around the C_5 symmetry axis of the equivalent Cp rings, while the vertically oriented states can play a role as intermediates in the exchange between surface-attached and detached ferrocene molecules.

The horizontally oriented molecular states obviously do not promote the possible formation of hydrogen bonds of the type $\text{Si-O-H}\cdots\pi$ -electrons on the silica surface as well as π - p interactions⁵⁴ of ferrocene with hexagonal and pentagonal rings of the activated carbon.⁵⁵ Since the iron atoms in ferrocene molecules have a partial positive charge, their interactions with the surfaces of both silica and activated carbon are of a polar nature.⁵⁶

Adsorption enthalpies and energies of surface-adsorbate interactions depend significantly on the host structures and pore sizes.⁵⁷⁻⁶⁰ Therefore, it is difficult to compare the thermodynamic parameters obtained for the adsorption of ferrocene on silica and activated carbon surfaces. The same accounts for other adsorbates in the pores of different support materials. However, it is interesting that the enthalpy characterizing the ferrocene-surface interactions is slightly smaller for silica (-6.7 kcal/mol) than for activated carbon

(-8.4 to -7.0 kcal/mol). In fact, it is very close to the heat of adsorption of benzene in microporous SiO_2 (-6.7 kcal/mol).⁵⁸ At the same time, the ferrocene-activated carbon interactions strongly exceed π - p interactions of benzene molecules in the pores of activated carbon (-4.2 kcal/mol).¹¹

Conclusions

In this chapter variable temperature ^{13}C and ^2H solid-state NMR experiments have been performed to characterize the dynamics of ferrocene molecules adsorbed on the surface within the pores of silica and activated carbon. Ferrocene shows a liquid-like behavior in the pores of both supports. It has been demonstrated that isotropically moving molecules and surface-attached molecular states of the ferrocene experience chemical exchange. The exchange is fast on the NMR time scale in the samples **1-75%-SiO₂**, **1-75%-AC** and also in **2-50%-AC** with sub-monolayer surface coverages. This exchange has been characterized by the free energy values of $\Delta G^\ddagger = 6.1$ kcal/mol for silica and $\Delta G^\ddagger = 6.2$ kcal/mol for activated carbon at 223 and 263 K, respectively. In contrast to the sub-monolayer coverages, material **2-130%-AC**, containing an excess of the ferrocene, shows a slow exchange. This indicates that vacant surface sites are indispensable for this exchange to take place.

The thermodynamically most stable state of ferrocene and ferrocene- d_2 on the surface within the pores of both materials is the horizontally oriented state. This state is directly observed at low temperatures while fast rotation of Cp rings around their C_5 symmetry axis takes place. The adsorption enthalpies of ferrocene in the pores of activated carbon

and silica have been determined as -8.4 to -7.0 kcal/mol and -6.7 kcal/mol, respectively. It has been suggested that interactions of the adsorbed ferrocene with the surface are of a polar nature in both materials. The new insights gained on this research topic should have major implications for catalysis, as adsorption is the first step in generating many heterogeneous metallocene-based catalysts on supports, for example, the Union Carbide catalyst.

Experimental

The silica (Merck, 40 Å average pore diameter, 0.063-0.2 mm average particle size, specific surface area 750 m²/g) was dried *in vacuo* at 200° C for 2 days to remove adsorbed water and condense surface silanol groups.²²

The activated carbon DARCO KB-G was obtained from Sigma Aldrich and it has a specific surface area of 1700 m²/g and pore volumes for micro-, meso-, and macropores of 0.36, 0.95, and 0.45 mL/g, respectively. Batches were pre-dried and degassed for 3 h at 200 °C *in vacuo* (0.035 mmHg) prior to being weighed in and used for adsorbing ferrocene.

The maximal surface coverage of the silica with **1** has been determined earlier.²⁸ Sample **1-75%-SiO₂** was prepared by dry grinding of 355.0 mg (1.908 mmol) of Cp₂Fe (**1**) with 1 g of silica for 5 minutes using a pestle and mortar. The deuterated ferrocene Cp₂Fe-*d*₂ (**2**) was synthesized by double lithiation and subsequent quenching with D₂O according to a literature method.⁶¹ Sample **2-75%-SiO₂** was created by dry grinding of **2** (355.0 mg, 1.887 mmol) with 1 g of silica. The maximal monolayer surface coverage of

the activated carbon brand DARCO KB-G has been determined previously.²⁵ The samples **1-50%-AC**, **1-75%-AC**, and **1-130%-AC** were generated by dry grinding of 536.2 mg (2.882 mmol), 804.3 mg (4.323 mmol), and 1394.1 mg (7.493 mmol) of Cp₂Fe, respectively, with 1 g of DARCO.

The ¹³C{¹H}, ²⁹Si{¹H} MAS and static NMR experiments and also the static ²H NMR experiments were carried out with a Bruker Avance 400 solid-state NMR spectrometer (400 MHz for ¹H nuclei) equipped with a two-channel 7 mm MAS probe head. The standard single pulse sequences (direct nuclear excitation with a 50° radio frequency pulse) were applied for the nuclei ¹³C and ²⁹Si using recycle delays as needed for the corresponding full spin-lattice relaxation estimated based on the inversion-recovery experiments.

The ¹³C{¹H} MAS NMR experiment for **1**, performed at a spinning rate of 3 kHz, required a recycle delay of 50 s due to the long ¹³C relaxation time. The *tppm15* (two-pulse phase modulation) pulse sequence has been used for complete ¹H decoupling. TMS (Me₄Si) has been used as an external standard for the ¹³C and ²⁹Si chemical shifts, and D₂O ($\delta(^2\text{H}) = 4.75$ ppm) for referencing the ²H NMR spectra.

The static ²H NMR data were collected with a solid-echo pulse sequence (90° – τ – 90°)¹⁹ with a τ delay of 40 μ s, a 90° pulse length of 5.25 μ s, and a relaxation delay of 4 s.

Typically, 2000-2400 transients were recorded for all ²H solid-state NMR measurements. All samples were densely packed into the insert-free rotors as finely ground powders. Compressed nitrogen was used as both the bearing and drive gas for the MAS measurements.

The variable-temperature ^{13}C and ^2H NMR experiments have been performed with a standard temperature unit of the spectrometer calibrated with liquid methanol placed into a 7 mm rotor. The experimental ^{13}C and ^2H T_1 relaxation times were measured by inversion-recovery ($180^\circ - \tau - 90^\circ$) experiments, and rf pulses were calibrated and τ delays widely varied to determine rough T_1 estimates. Relaxation (recycle) delays were adjusted to provide full nuclear relaxation in each cycle.

The quadrupolar coupling constants were derived from the ^2H MAS NMR spectra using the NMR simulation program Dmfit. The error margin in this fitting procedure is ± 0.5 kHz.

The experimental ^{13}C and ^2H inversion-recovery data for the displays of signal intensity versus τ time have been treated with a standard nonlinear fitting computer program based on the Levenberg–Marquardt algorithm.⁶² The statistical errors of the ^{13}C and ^2H T_1 time determinations were $<15\%$. The lineshape analysis of the static $^{13}\text{C}\{^1\text{H}\}$ and ^2H VT NMR spectra was performed with the program DNMR in the software package of the Bruker spectrometer.

References

1. D. J. Hornbaker, S. J. Kahng, S. Misra, B. W. Smith, A. T. Johnson, E. J. Mele, D. E. Luzzi, A. Yazdani, *Science* **2002**, *295*, 828-831.
2. K. Kaiser, L. M. Scriven, F. Schulz, P. Gawel, L. Gross, H. L. Anderson, *Science* **2019**, *365*, 1299-1301.
3. J. Lee, H. Kim, S. J. Kahng, G. Kim, Y. W. Son, J. Ihm, H. Kato, Z. W. Wang, Z. T. Okazaki, H. Shinohara, Y. Kuk, *Nature* **2002**, *415*, 1005-1008.

4. V. K. Gupta, T. A. Saleh, *Environ. Sci. Pollut. Res.* **2013**, *20*, 2828-2843.
5. J. Zhao, W. Ren, H.-M Cheng, *J. Mater. Chem.* **2012**, *22*, 20197-20202.
6. T. Liu, Y. Li, Q. Du, J. Sun, Y. Jiao, G. Yang, Z. Wang, Y. Xia, W. Zhang, K. Wang, H. Zhu, D. Wu, *Colloids Surf., B* **2012**, *90*, 197-203.
7. G. Zhao, J. Li, X. Ren, C. Chen, X. Wang, **2011**, *Environ. Sci. Technol.* *45*, 10454-10462.
8. S.-T. Yang, S. Chen, Y. Chang, A. Cao, Y. Liu, H. Wang, *J. Colloid Interface Sci.* **2011**, *359*, 24-29.
9. X. Ren, C. Chen, M. Nagatsu, X. Wang, *Chem. Eng. J.* **2011**, *170*, 395-410
10. K. Yang, B. Xing, *Chem. Rev.* **2010**, *110*, 5989-6008.
11. P. J. Hubbard, V. I. Bakhmutov, J. Blümel, Small Organic Molecules Adsorbed in the Pores of Activated Carbon: Molecular Motions and Interactions with the Surface, *in preparation*.
12. M. S. Reisch, Carbon's Next Moves, *Chem. Eng. News* **2014**, *92*, 18-19.
13. A. L. Cazetta, O. Pezoti, K. C. Bedin, T. L. Silva, A. P. Junior, T. Asefa, V. C. Almeida, *ACS Sustainable Chem. Eng.* **2016**, *4*, 1058-1068.

14. M. V. Gil, N. Alvarez-Gutierrez, M. Martinez, F. Rubiera, C. Pevida, *Chem. Eng. J.* **2015**, *269*, 148-158.
15. M. M. Dubinin, R. S. Vartapetyan, A. M. Voloshchuk, J. Kaerger, H. Pfeifer, *Carbon* **1988**, *26*, 515-520.
16. A. W. Heinen, J. A. Peters, H. van Bekkum, *Appl. Catal., A* **2000**, *194-195*, 193-202.
17. H. Omichi, T. Ueda, T. Eguchi, *Adsorption* **2015**, *21*, 273-282.
18. J. Park, I. Hung, Z. Gan, O. J. Rojas, K. H. Lim, S. Park, *Bioresour. Technol.* **2013**, *149*, 383-389.
19. C. A. Fyfe, *Solid-State NMR for Chemists*. C.F.C. Press, Guelph, Canada, **1983**.
20. T. M. Duncan, *A Compilation of Chemical Shift Anisotropies*. Farragut Press: Chicago, IL, **1990**.
21. Selected examples: (a) J. Blümel, *Coord. Chem. Rev.* **2008**, *252*, 2410-2423. (b) J. Guenther, J. Reibenspies, J. Blümel, *Adv. Synth. Catal.* **2011**, *353*, 443-460. (c) R. Silbernagel, A. Diaz, E. Steffensmeier, A. Clearfield, J. Blümel, *J. Mol. Catal. A* **2014**, *394*, 217-223. (d) C. Merckle, J. Blümel, *Adv. Synth. Catal.* **2003**, *345*, 584-588. (e) C. Merckle, J. Blümel, *Top. Catal.* **2005**, *34*, 5-15. (f) J. H. Baker, N. Bhuvanesh, J. Blümel, *J. Organomet. Chem.* **2017**, *847*, 193-203. (g) Y. Yang, B. Beele, J. Blümel, *J. Am. Chem. Soc.* **2008**, *130*, 3771-3773. (h) J. C. Pope, T. Posset, N. Bhuvanesh, J. Blümel, *Organometallics* **2014**, *33*, 6750-6753. (i) T. Posset, J. Blümel, *J. Am. Chem. Soc.* **2006**, *128*, 8394-8395. (j) T. Posset, J. Guenther, J. Pope, T. Oeser, J. Blümel, *Chem. Commun.* **2011**, *47*, 2059-2061. (k) S. Reinhard, P. Soba, F. Rominger, J. Blümel, *Adv. Synth. Catal.* **2003**, *345*, 589-602. (l) F. Piestert, R. Fetouaki, M. Bogza, T. Oeser, J. Blümel, *Chem. Commun.* **2005**, 1481-1483. (m) K. J. Cluff, N. Bhuvanesh, J. Blümel, *Chem. Eur. J.* **2015**, *21*, 10138-10148. (n) J. Guenther, J. Reibenspies, J. Blümel, *Mol. Catal.* **2019**, *479*, 110629.

22. (a) R. K. Iler, *The Chemistry of Silica*, John Wiley, New York, 1979. (b) J. Blümel, *J. Am. Chem. Soc.* **1995**, *117*, 2112-2113. (c) K. D. Behringer, J. Blümel, *J. Liq. Chromatogr.* **1996**, *19*, 2753-2765.
23. Y. Oprunenko, I. Gloriov, K. Lyssenko, S. Malyugina, D. Mityuk, V. Mstislavsky, H. Günther, G. Von Firks, M. Ebener, *J. Organomet. Chem.* **2002**, *656*, 27-42.
24. C. R. Hilliard, S. Kharel, K. J. Cluff, N. Bhuvanesh, J. A. Gladysz, J. Blümel, *Chem. Eur. J.* **2014**, *20*, 17292-17295.
25. S. Kharel, K. J. Cluff, N. Bhuvanesh, J. A. Gladysz, J. Blümel, *Chem. Asian J.* **2019**, *14*, 2704-2711.
26. C. R. Hilliard, N. Bhuvanesh, J. A. Gladysz, J. Blümel, *Dalton Trans.* **2012**, *41*, 1742-1754.
27. S. Kharel, N. Bhuvanesh, J. A. Gladysz, J. Blümel, *Inorg. Chim. Acta* **2019**, *490*, 215-219.
28. N. A. Bewick, A. Arendt, Y. Li, S. Szafert, T. Lis, K. A. Wheeler, J. Young, R. Dembinski, *Curr. Org. Chem.* **2015**, *19*, 469-474.
29. (a) F. F. Arp, S. H. Ahn, N. Bhuvanesh, J. Blümel, *New J. Chem.* **2019**, *43*, 17174-17181. (b) F. F. Arp, N. Bhuvanesh, J. Blümel, *Dalton Trans.* **2019**, *48*, 14312-14325.
30. (a) S. H. Ahn, D. Lindhardt, N. Bhuvanesh, J. Blümel, *ACS Sustainable Chem. Eng.* **2018**, *6*, 6829-6840. (b) S. H. Ahn, D. Bhuvanesh, J. Blümel, *Chem. Eur. J.* **2017**, *23*, 16998-17009. (c) S. H. Ahn, K. J. Cluff, N. Bhuvanesh, J. Blümel, *Angew. Chem. Int. Ed.* **2015**, *54*, 13341-13345.
31. K. J. Cluff, M. Schnellbach, C. R. Hilliard, J. Blümel, *J. Organomet. Chem.* **2013**, *744*, 119-124.

32. K. J. Cluff, J. Blümel, *Organometallics* **2016**, *35*, 3939–3948.
33. (a) K. J. Cluff, J. Blümel, *Chem. Eur. J.* **2016**, *22*, 16562-16575. (b) K. J. Cluff, N. Bhuvanesh, J. Blümel, *Organometallics* **2014**, *33*, 2671-2680.
34. K.-T. Li, C.-N. Yang, *Mater. Today Commun.* **2019**, *19*, 80-86.
35. (a) F. Silveira, R. Brambilla, N. P. da Silveira, M. do Carmo Martins Alves, F. C. Stedile, S. B. C. Pergher, J. H. Z. dos Santos, *J. Mater. Sci.* **2010**, *45*, 1760-1768. (b) F. Silveira, M. do Carmo Martins Alves, F. C. Stedile, S. B. Pergher, J. H. Z. dos Santos, *J. Mol. Catal.* **2010**, *315*, 213-220.
36. A. N. Estrada-Ramirez, C. Ventura-Hunter, J. Vitz, E. Díaz-Barriga Castro, R. D. Peralta-Rodriguez, U. S. Schubert, C. Guerrero-Sánchez, O. Pérez-Camacho, *Macromol. Chem. Phys.* **2019**, *220*, 1900259.
37. A. A. Bernardes, G. L. Scheffler, C. Radtke, D. Pozebon, J. H. Z. dos Santos, Z. N. da Rocha, *Colloids Surf. A Physicochem. Eng. Asp.* **2020**, *584*, 124020.
38. W. P. McKenna, S. Bandyopadhyay, E. M. Eyring, *Applied Spectrosc.* **1984**, *38*, 834-837.
39. F. J. Karol, G. L. Karapinka, C. Wu, A. W. Dow, R. N. Johnson, W. L. Carrick, *J. Polym. Sci. A1* **1972**, *10*, 2621.
40. M. Schnellbach, J. Blümel, F. H. Köhler, *J. Organomet. Chem.* **1996**, *520*, 227-230.
41. L. Qiao, X. Zhou, X. Li, W. Du, A. Yu, S. Zhang, Y. Wu, *Talanta* **2017**, *163*, 94-101.

42. M. D. Lowery, R. J. Wittebort, M. Sorai, D. N. Hendrickson, *J. Am. Chem. Soc.* **1990**, *112*, 4214-4225.
43. Z. Narankiewicz, A. L. Blumenfeld, V. L. Bondareva, I. A. Mamedyarova, M. N. Nefedova, Sokolov, *Journal of Inclusion Phenomena and Molecular Recognition in Chemistry* **1991**, *11*, 233-245.
44. J. Pope, H.-J. Sue, T. Bremner, J. Blümel, *Polymer* **2014**, *55*, 4577-4585.
45. J. C. Pope, H.-J. Sue, T. Bremner, J. Blümel, *J. Appl. Polym. Sci.* **2015**, *132*, 1804-1816.
46. H. Günzler, H.-U. Gremlich, *IR-Spektroskopie*, 4th ed., Wiley-VCH, **2003**.
47. W. K. Winter, B. Curnutte, S. E. Whitcomb, *Spectrochim. Acta* **1959**, *12*, 1085-1102.
48. E. R. Lippincott, R. D. Nelson, *Spectrochim. Acta* **1958**, *10*, 307-329.
49. N. Mohammadi, A. Ganesan, C. T. Chantler, F. Wang, *J. Organomet. Chem.* **2012**, *713*, 51-59.
50. R. H. Hesas, A. Arami-Niya, W. M. A. Daud, J. N. Sahu, *BioResources* **2013**, *8*, 2950-2966.
51. A. Belgacem, M. Belmedani, R. Rebiai, H. Hadoun, *Chem. Eng. Trans.* **2013**, *32*, 1705-1710.
52. A. J. Campbell, C. A. Fyfe, D. Harold-Smith, K. R. Jeffrey, *Mol. Cryst. Liq. Cryst.* **1976**, *36*, 1-23.

53. D. Kuwahara, F. Imashiro, T. Terao, *Chem. Phys. Lett.* **1993**, *204*, 533-537.
54. C. H. Holm, J. A. Ibers, *J. Chem. Phys.* **1959**, *30*, 885-888.
55. A. M. Orendt, J. C. Facelli, Y. J. Jiang D. M. Grant, *J. Phys. Chem. A* **1998**, *102*, 7692-7697.
56. D. Massiot, F. Fayon, M. Capron, I. King, C. S. Le, K.-O. Alonso, B.; Durand, B. Bujoli, Z. Gan, G. Hoatson, *Magn. Reson. Chem.* **2002**, *40*, 70-76.
57. M. Ormaza, P. Abufager, N. Bachellier, R. Robles, M. Verot, T. Le Bahers, M.-L. Bocquet, N. Lorente, L. Limot, *J. Phys. Chem. Lett.* **2015**, *6*, 395-400.
58. M. Kempniński, M. Śliwińska-Bartkowiak, W. Kempniński, *Rev. Adv. Mater. Sci.* **2007**, *14*, 163-166.
59. A. B. Wieckowski, L. Najder-Kozdrowska, P. Rechnia, A. Malaika, B. Krzyzyska, M. Kozłowski, *Acta Phys. Pol. A.* **2016**, *130*, 701-704.
60. Y. Xu, T. Watermann, H.-H. Limbach, T. Gutmann, D. Sebastianib, G. Buntkowsky, *J. Phys. Chem. Chem. Phys.* **2014**, *16*, 9327- 9336.
61. P. J. F. Harris, Z. Liu, K. Suenaga, *J. Phys. Condens. Matter* **2008**, *20*, 362201-362206.
62. H. L. Chiang, C. P. Huang, P. C Chiang, *Chemosphere* **2002**, *46*, 143-152.
63. S. K. Parida, S. Dash, S. Patel, B. K. Mishra, *Advances in Colloid and Interface Science* **2006**, *121*, 77-110.

64. M. A. Hernandez, J. A. Velasco, M. Asomoza, S. Soli's, F. Rojas, V. Lara, *Ind. Eng. Chem. Res.* **2004**, *43*, 1779-1787.
65. Z. G. Zhao, L. H. Zhang, Y. J. Lin, *Colloid and Interface Science* **1994**, *166*, 23-28.
66. P. A. Russo, M. L. R. Carrott, Carrott, *Adsorption* **2008**, *14*, 367-375.
67. J. J. Bishop, A. Davison, M. L. Katcher, D. W. Lichtenberg, R. E. Merrill, *J. Organomet. Chem.* **1971**, *27*, 241-249.
68. K. Levenberg, *Quart. Appl. Math.* **1994**, *2*, 164-168.

CHAPTER IV

ADSORPTION OF VOLATILE ORGANIC COMPOUNDS

Introduction

Upon completion of the mobility studies of phosphine oxides and ferrocene on diverse surfaces, we considered how we could apply this knowledge towards solving a real-life problem. Around this same time our group was contacted by a waste management company, Waste Equipment LLC, to investigate ways to reduce, or entirely remove, the odor emanating from solid-waste containers. This fortuitous circumstance provided an avenue for us to utilize the previous academic adsorption work towards solving a tangible problem.

Waste disposal is an increasing problem for modern society. As the population of the world continues to grow additional waste is produced. Common waste containers, trash barrels and dumpsters, contribute to a large portion of the everyday inconveniences associated with waste disposal.

Typically, these refuse bins contain many different volatile organic compounds, VOCs, that are responsible for the pungent odor of common waste that is of a repellent and potentially toxic nature. Many of these VOCs build up in the headspace of a closed trash container or in the access shafts of apartment buildings and are released upon opening of the lid. In commercial settings odors next to food stores reduce the interest of customers and therefore lead to financial losses. At present commercial odor removal systems use expensive ozonizers, ozone generating devices, that have only a limited impact on improving the air quality in the described settings. This situation led to the idea

of creating an air purification system that could mitigate the build-up of VOCs and completely remove the malodorous emanations associated with large food dumpsters or other waste receptacles.

A general literature search for the compounds responsible for the odor of common waste yields a large diversity of different VOCs containing a multitude of functional groups. However, the VOCs found in roadside dumpsters in the UK contained mostly alkanes, alkylbenzenes, aldehydes and terpenes.¹ Additionally, analysis done at a biogas food waste generation plant showed that hydrogen sulfide, ethyl sulfide, and trimethylamine contributed the most to complaints about air pollution.² This finding denoting sulfur-based compounds as being responsible for the majority of the scent associated with food spoilage was further corroborated by an investigation into the local refuse bins in urban communities containing mostly an excess of spoiled prepared foods.³ Typical odors in retirement homes are dominated by aldehydes with long methylene chains like nonanal. In essence, the major culprits in most settings are the substance classes aldehydes, carboxylic acids, hydrocarbons (aromatic and aliphatic), amines, and sulfur-containing compounds.

At first sight this gives the impression of a plethora of compounds one would have to target to remove all odors. However, once separated into four principal categories, aldehydes, acids, bases, and non-polar compounds, the idea of their removal appears much more manageable. The proposed concept was to design individual filters that would adsorb VOCs, chemically transform them into non-volatile species, and therewith trap each of

these compounds. This goal was realized using oxidizers, acid-base principles, and strong van der Waals forces to retain the molecules on the surfaces.

For instance, basic VOCs like amines would be adsorbed on an acidic support which would then form a salt or an adduct with the alkaline VOC and trap it on the surface. Benzoic acid, spread out in a monolayer on the surface of a porous support, represents a favorable candidate as a solid acidic modifier in order to trap volatile bases. This assumption is corroborated, for example, by the X-ray crystal structure of the hydrogen-bonded adduct of benzoic acid with triethylamine.⁴ Along with benzoic acid, citric acid and terephthalic acid were also considered for their additional carboxylic acid groups per molecule. The more intramolecular carboxylic acid groups there are, the fewer surface sites will be occupied and the less filter material will be needed for a given amount of basic VOC.

For generating a base-modified filter that targets the removal of volatile odorous acids like butyric acid, triethylamine vapor can be deposited on a favorable surface as the least expensive option. Additionally, if any triethylamine modifier were to leave the support it could be trapped by subsequent benzoic acid-modified filters, along with any other bases produced by the waste.

This concept appears straightforward for volatile acids and bases, however, hydrocarbons, aldehydes and sulfur-containing compounds still need specific scavenging. In order to trap hydrocarbons, using additional nonpolar, solid surface modifiers to enhance the van der Waals interactions of these VOCs with the support was planned. The

formed film of a hydrocarbon mixture was intended to bind more firmly and retain any volatile hydrocarbons on the surface.

For removing aldehydes and sulfur-based compounds from the air, using a solid oxidizer on the surface of a porous support appeared most viable. If a solid oxidizer is spread out on the surface in a monolayer and then reacts with an aldehyde, it can be oxidized to a non-volatile carboxylic acid that remains in the support material. In case the formed acid is volatile, it can be absorbed in the next step with a base-modified filter. Sulfur-based compounds can be oxidized to sulfates or sulfones. The former are usually not volatile, while the latter adsorb readily on support surfaces.

For the choice of oxidizers there are several options. One prerequisite was that it had to be a solid oxidizer because a) gas phase oxidants like ozone have not been efficient in the past, and b) liquid oxidants like aqueous hydrogen peroxide are too corrosive and not practical to handle by service personnel. Another requirement the oxidizer had to fulfill was that its lifetime had to be sufficiently long. While it was desirable that the oxidizer should be inexpensive, the level of desperation of many dumpster owners was deemed high enough by the cooperating company to justify a higher price of the generated filter material.

Thankfully, previous research performed within the group by Dr. Shin Hye Ahn and Dr. Casie Hilliard led to two new branches of stable solid oxidizers based on hydrogen-bonded adducts of trialkyl- and triarylphosphine oxides with hydrogen peroxide and di(hydroperoxy)alkanes.^{5a,b} In particular, the di(hydroperoxy)propane adduct of

triphenylphosphine oxide was promising for the intended application based on its long shelf life and reasonable cost to generate.

The final, important decision towards designing a system to trap malodorous VOCs was to choose a support. Again, the chosen support had to be economical, environmentally benign, modifiable, and it needed to have a sufficient pore size and surface area to accommodate large amounts of VOCs within a small volume of bulk support material. Therefore, based on our previous adsorption studies of ferrocene, activated carbon was chosen as it fulfilled all these requirements.

As mentioned previously, activated carbon has received significant attention for its ability to adsorb VOCs due to its large surface area per gram and simplicity to modify for target adsorption.⁶⁻⁹ Activated carbon is made from numerous different carbon sources including wood, peat, and anthracite.^{10,11} Typically, phosphoric acid or potassium hydroxide are used as activating agents in the industrial production of activated carbon.¹⁰ Recently, activated carbon has received significant attention for the removal of environmental odors,¹² and the treatment of waste water.¹³ Additionally, modified activated carbons are used in respirators for gas masks.¹⁴ Given the abundance of applications, activated carbon seemed like the perfect candidate to test for the adsorption of VOCs.

Results and Discussion

As outlined above, the first step was designing the optimal acid-modified filter for trapping alkaline VOCs. It was desired that no organic solvent was required for generating the filter materials, as these entail safety issues and additional costs. Therefore, based on our knowledge about solid-solid surface adsorption, three solid acids were tested for their mobility on DARCO[®] brand activated carbon, benzoic, citric and terephthalic acid. In each case, in order to prevent clogging the pores, the desired sub-monolayer amount of the acid (Table 10) was dry ground with a mortar and pestle together with 1g of activated carbon for 5 minutes and left to equilibrate overnight in a glass vial. Subsequently, ¹³C MAS NMR was measured for each sample (Figure 32).

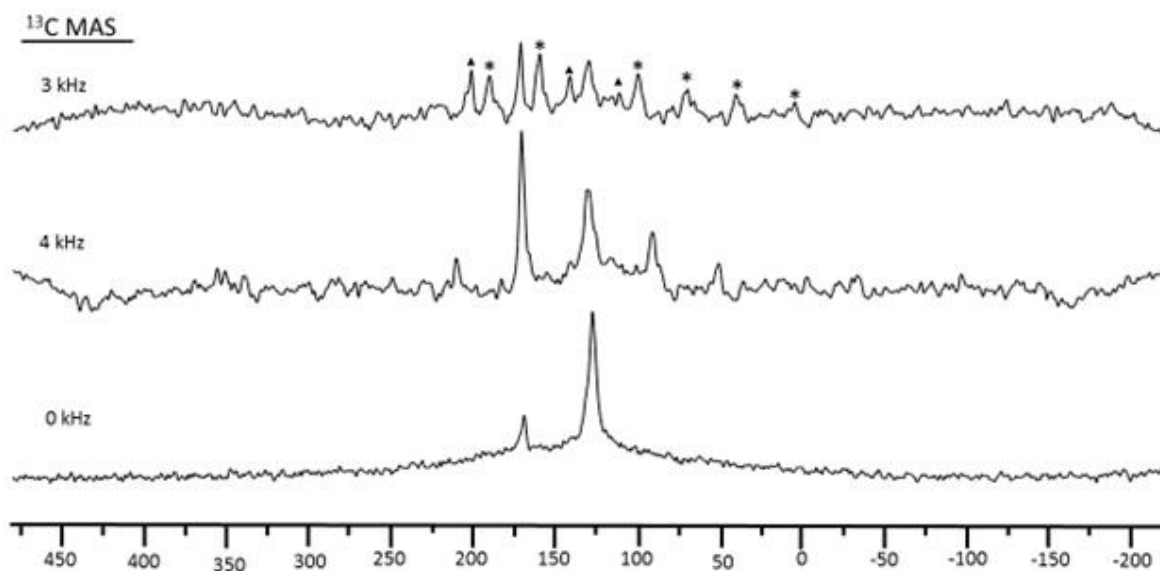


Figure 32. ¹³C MAS NMR of neat polycrystalline benzoic acid at a rotational speed of 3 kHz (top) and 4 kHz (middle), and ¹³C NMR of a static sample of benzoic acid adsorbed on DARCO (bottom).

First, the polycrystalline benzoic acid sample, rotated at 3 and 4 kHz, were used to determine the isotropic peaks of benzoic acid. The aryl carbon signals overlap at 126.2, the carboxylic acid carbon corresponds to the signal at 169.8 ppm (Figure 32). The other peaks visible in the spectra correspond to the rotational sidebands of these signals. After the dry adsorption of benzoic acid onto the DARCO[®] surface a complete collapse of the CSA of the benzoic acid signals is seen even at 0 kHz rotational speed. This effect reiterates the aforementioned mobility of different compounds on solid supports, as described in the previous chapters of this thesis for triphenylphosphine oxide and ferrocene. Again, the complete averaging out of the CSA indicates liquid-like isotropic reorientations in the solid state. Regarding the use of the generated material as a scavenger of volatile bases, this spread of the benzoic acid on the surface is highly favorable, as it prevents clogging of the pores and provides maximal exposure of the reagent to the gas phase.

Citric acid and terephthalic acid showed similar NMR characteristics as compared to benzoic acid, despite their additional carboxylic acid groups. After adsorption on DARCO[®] the CSA was completely averaged out and the three isotropic signals of citric acid appeared at 172, 71, and 41.5 ppm (Figure 33).

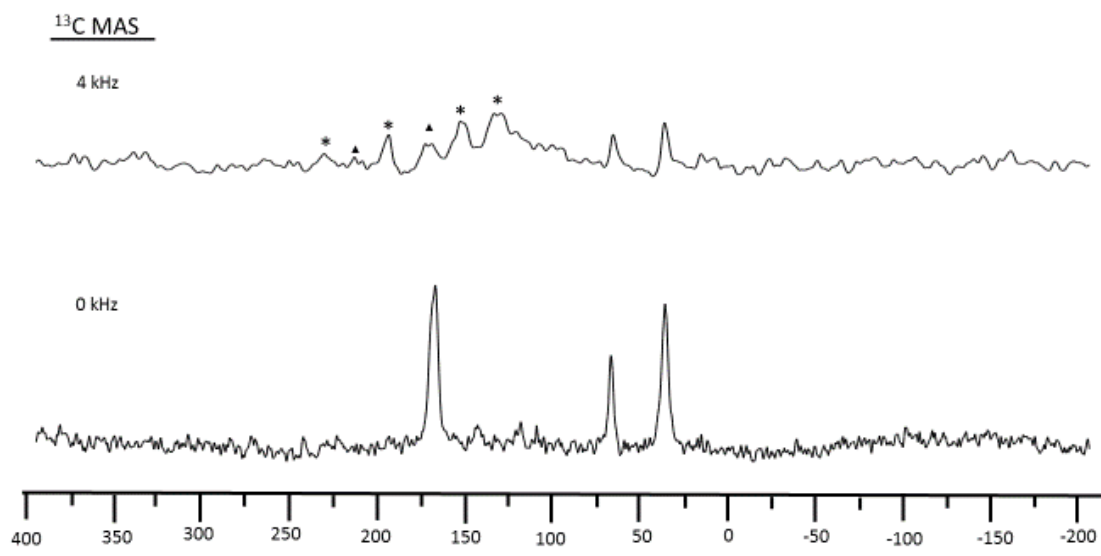


Figure 33. ^{13}C MAS and static NMR of polycrystalline citric acid (top) and citric acid adsorbed on DARCO (bottom) in a sub-monolayer.

Terephthalic acid was not as favorable regarding adsorption on DARCO[®]. The modified sample only showed a single broad resonance at ~130 ppm (Figure 34). This means that terephthalic acid was not spread out and as mobile on the surface as benzoic or citric acid. This may be due to size restrictions within the pores, or too strong interactions with the surface due to the two carboxylic acid groups.

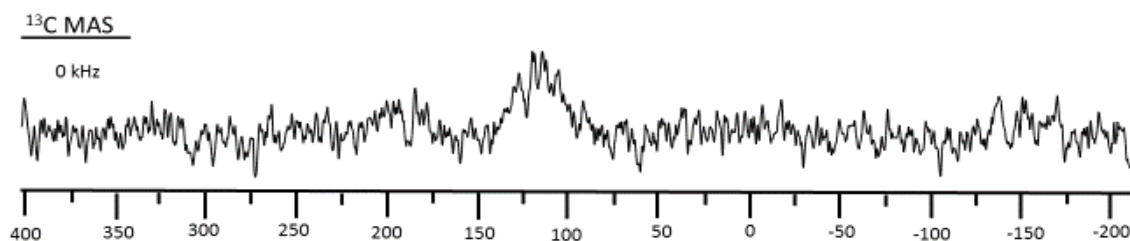


Figure 34. ^{13}C Wideline NMR of terephthalic acid adsorbed on DARCO.

Next, the three different surface-adsorbed acids were tested regarding their ability to absorb triethylamine as the VOC over 24 hours. As a general example, a standard

experiment is shown in Figure 35. A colored gas (nature non-disclosable due to NDA) is used for visualizing the diffusion of a VOC. The volatile compound is separated from the solid support using a glass bridge and the entire system is closed to prevent adsorption of additional vapors during testing and to afford reproducible conditions.

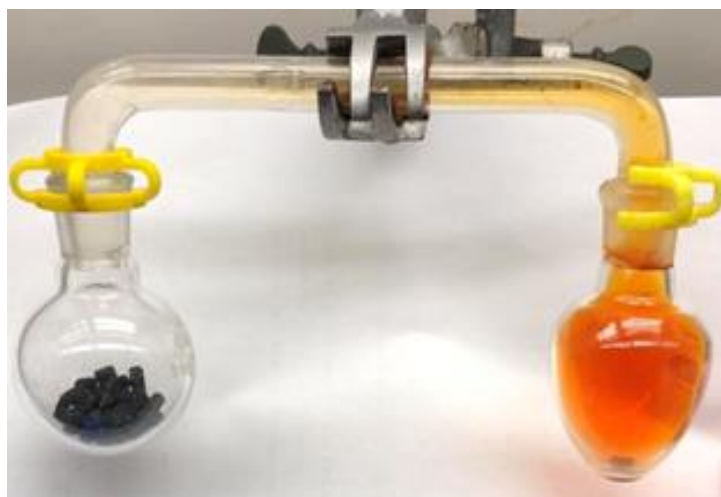


Figure 35. Standard setup to test the uptake of a gas into a solid support.

Benzoic acid far outperformed citric acid and terephthalic acid in terms of mmoles of triethylamine per gram of DARCO[®] with 5.83, 1.15 and 4.29 mmoles per g of support, respectively (Table 10). No correlation between the number of carboxylic acid groups per modifier molecule and the mmoles of absorbed triethylamine has been found.

Support/Modifier/NEt ₃	Surface Coverage Modifier (%)	Modifier (mmol/1g Support)	Adsorbed NEt ₃ (mmol/1g Support)	Ratio NEt ₃ :Modifier
DARCO [®] /Benzoic Acid/Triethylamine	75	4.03	5.83	1.45
DARCO [®] /Benzoic Acid/Triethylamine	95	5.02	2.33	0.46
DARCO [®] /Citric Acid/Triethylamine	75	3.93	1.15	0.29
DARCO [®] /Terephthalic Acid/Triethylamine	75	4.54	4.29	0.95
150 Å Silica/Benzoic Acid/Triethylamine	75	0.82	2.77	3.38

Table 10. Amounts of triethylamine odor molecules adsorbed per gram of DARCO[®] after exposure of the modified supports to vapors of the base for 24 hours.

Benzoic acid with one carboxylic acid group absorbed 1.45 equivalents of base. Citric acid with three carboxylic acid groups adsorbed 0.29 equivalents and terephthalic acid with two adsorbed 0.95 equivalents. Additionally, when a 95% sub-monolayer of benzoic acid was compared to a 75% sub-monolayer, the 20% increased coverage decreased the mmoles of odor molecules adsorbed per gram of DARCO[®] from 5.83 to 2.33 mmoles. The decrease in absorbed odor molecules per benzoic acid molecule can be most likely attributed to pore clogging effects or the formation of double layers on the support that hinder the access to the benzoic acid.

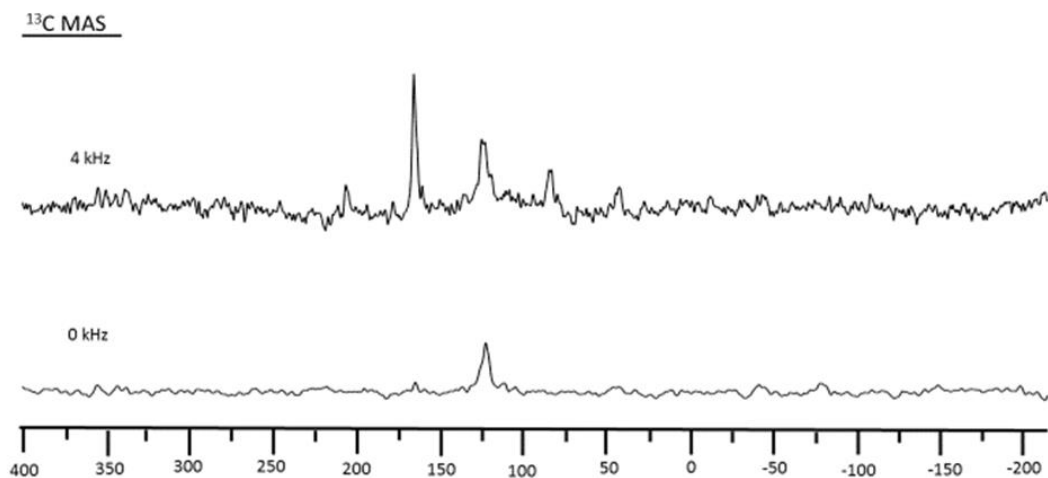


Figure 36. ^{13}C MAS NMR of polycrystalline benzoic acid (top, 4 kHz), and a static sample of benzoic acid adsorbed on silica (150 Å average pore size, 0 kHz, bottom).

Finally, for comparison, silica with a large average pore size of 150 Å was chosen as the support material instead of DARCO[®]. When Benzoic acid was dry ground with the silica a similar collapse of the CSA was seen as in the case of DARCO[®] as the support (Figure 36). However, when comparing the modified activated carbon to the modified silica, the former outperformed the silica with 5.83 to 2.77 mmoles of triethylamine per gram of support. This can also be attributed to the difference in surface area and specific weight between the two supports. DARCO[®] has a surface area of 1700 m²/g and the used silica has a specific surface area of only 350 m²/g. However, the decrease in the amount of triethylamine adsorbed is not directly proportional to the ratio of the two different supports surface areas. In fact, by that measure the silica performed surprisingly well. Interestingly, when a ^{13}C solid-state NMR spectrum of benzoic acid-modified silica is recorded after exposure to triethylamine, no signal of the latter is found. In comparison, residual triethylamine can easily be seen in both the benzoic acid-modified DARCO[®] and

the terephthalic acid-modified DARCO[®] samples after exposure to the base (Figure 37). This could be interpreted as an indication that in the silica sample the formed adducts between benzoic acid and triethylamine are not mobile on the surface, leading to no signal in the wide-line solid-state NMR spectrum because the anisotropic interactions are no longer averaged out. The mobilities of salts and hydrogen-bonded adducts on diverse surfaces are studied in a parallel project in the group.

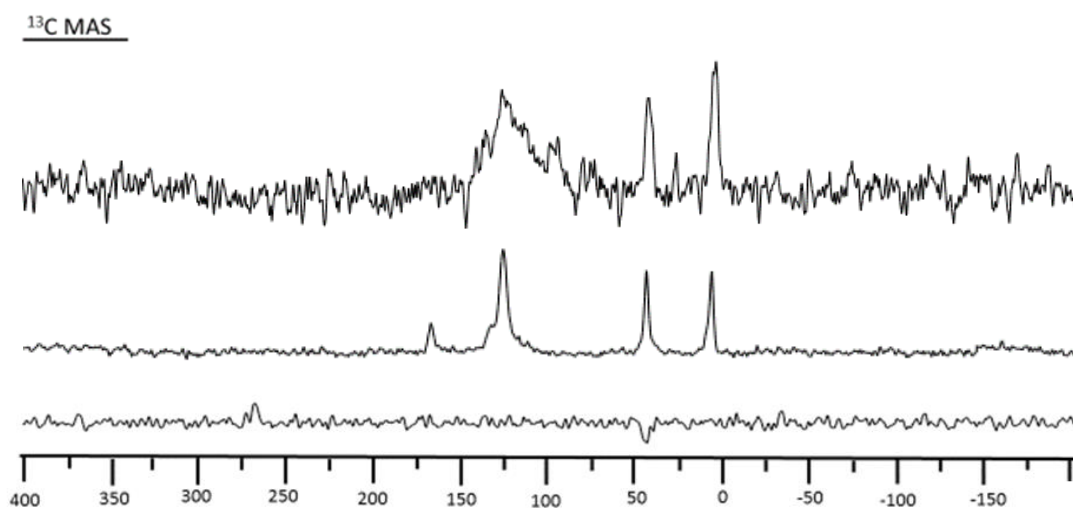


Figure 37. ¹³C Wideline NMR of terephthalic acid-modified DARCO[®] (top), benzoic acid-modified DARCO[®] (middle), and benzoic acid-modified silica (bottom) after treating the samples with triethylamine for 24 hours.

After these preliminary experiments with 24-hour exposure times, long-term testing of the adsorption was pursued. For this investigation, four different modified surfaces were monitored gravimetrically over the course of 14 days to determine their maximal adsorption capacity. Specifically, the four different supports were 75% benzoic acid-modified DARCO[®], 95% benzoic acid-modified DARCO[®], 75% citric acid-modified DARCO[®] and Norit[®] pellets, a cheaper brand of activated carbon, soaked in phosphoric

acid over the course of 24 hours. The adsorption curves (Figure 38, Table 11) show that after 14 days citric acid-modified material absorbed the largest amount of triethylamine with 1.033 g per 1.000 g of support. The 95% benzoic acid-modified DARCO actually retained more triethylamine than the 75% benzoic acid-modified DARCO[®]. The phosphoric acid-soaked Norit[®] pellets performed quite well with 0.864 g of triethylamine per 1.000 g of support. Surprisingly, the citric acid-modified support surpassed the benzoic acid-modified sample in capacity and ended up with a ratio of triethylamine to modifier of 2.5 (Figure 39, Table 11). Although this value is still 0.5 too small for a direct adduct equivalent between triethylamine and citric acid (theoretical ratio 3: 1), it does show that offering more carboxylic acid groups per molecule enhances the overall capacity of the support to absorb a volatile base. In comparison, the benzoic acid modified DARCO[®] sample displayed a ratio of about 1.5 at the end of the 14 days. This higher value than the expected capacity (theoretical ratio 1:1) may be due to additional direct adsorption of triethylamine on the bare surface of the support that adds to the absorption due to salt formation.

Table 11. Amounts of triethylamine odor molecules adsorbed per gram of DARCO[®] after exposure of the modified supports to vapors of the base for 14 days.

Support/Modifier/NEt ₃	Surface Coverage Modifier (%)	Modifier (mmol/1g Support)	Adsorbed NEt ₃ (g/1g Support)	Ratio NEt ₃ :Modifier
DARCO [®] /Benzoic Acid/Triethylamine	75	4.03	0.72	1.81
DARCO [®] /Benzoic Acid/Triethylamine	95	5.02	0.80	1.56
DARCO [®] /Citric Acid/Triethylamine	75	3.93	1.03	2.54
Norit [®] /Phosphoric Acid/Triethylamine	-	-	0.86	0.95

Furthermore, work performed previously by another graduate student in the group, Jordon Benzie, has shown that triethylamine can be taken up and retained for some time on the surface of DARCO[®]. His independent experiments indicated that 1 gram of DARCO[®] can adsorb up to 200 mg of triethylamine, with 160 mg being retained at the end of a 7 day period of exposure to the atmosphere.¹⁵ This insight of lacking retention of triethylamine on the surface actually set the foundation for the base-modified DARCO[®] in order to better retain basic VOCs.

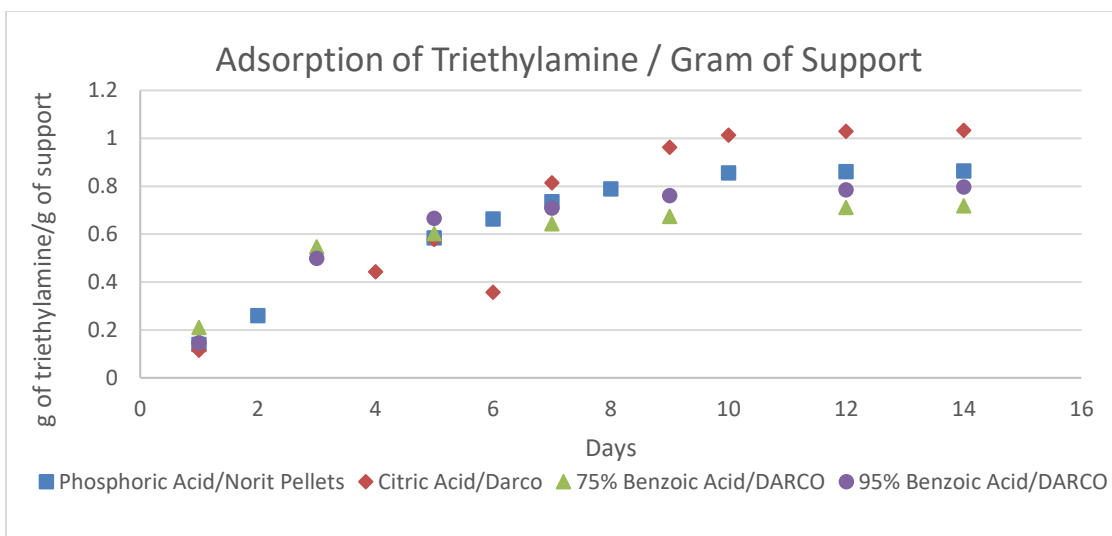


Figure 38. Adsorption capacities of several modified surfaces expressed in grams of triethylamine per gram of support.

Equally important to the uptake capacity for an odor removal system is the retention of the absorbed molecules on the surface. Therefore, desorption curves under ambient conditions were collected over the course of 9 days. During this time each sample was left exposed to the atmosphere in a glass vial and the loss of mass was monitored gravimetrically (Figure 40). Each sample lost a small amount of mass over the course of time, but each stabilized slightly higher or lower than their expected equivalent ratios (Figure 41). Overall, the citric acid-modified DARCO[®] retained the highest amount of triethylamine even after a prolonged desorption period.

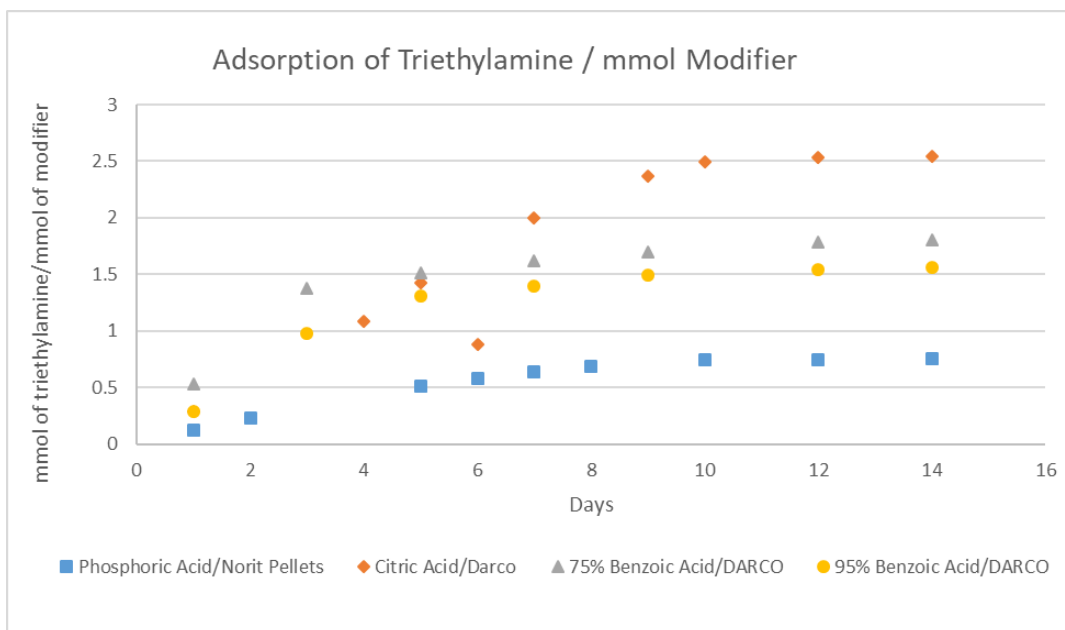


Figure 39. Adsorption curves for several modified supports expressed as molar ratios of triethylamine versus modifier.

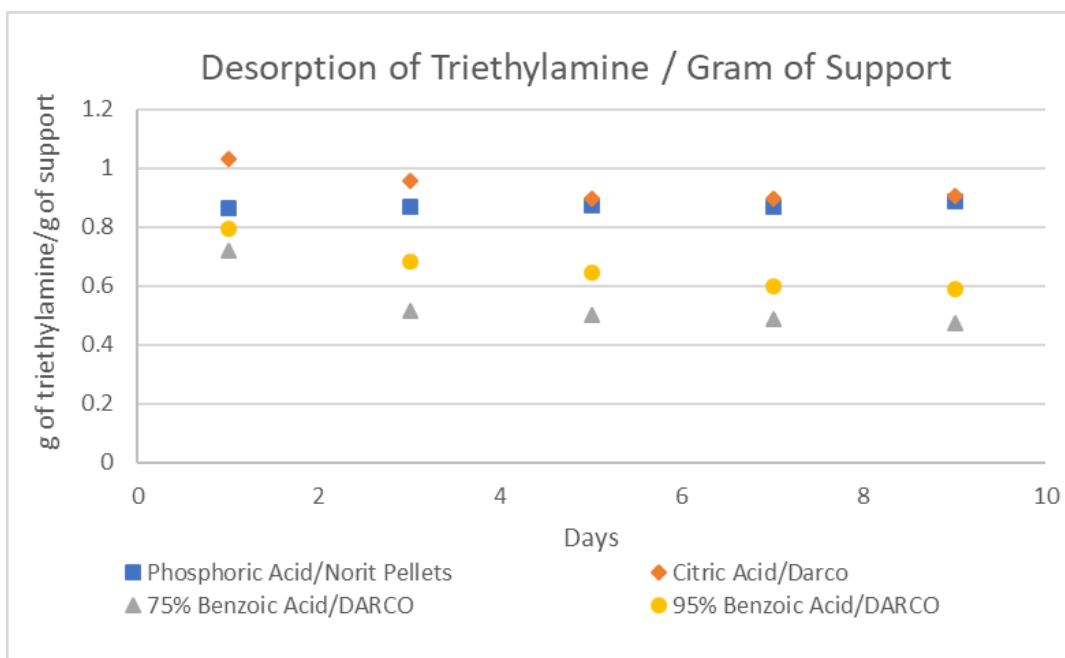


Figure 40. Desorption curves for several modified surfaces, expressed in grams of triethylamine versus grams of support.

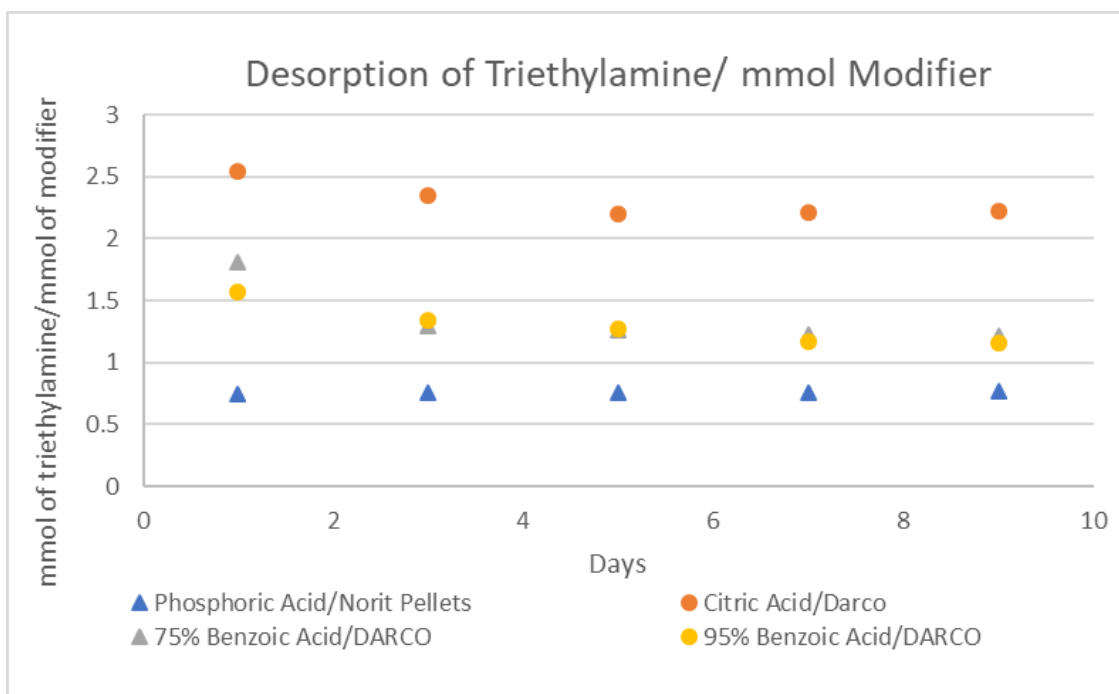


Figure 41. Desorption curves for several modified surfaces, expressed in the molar ratios of triethylamine versus modifiers.

The phosphoric acid-modified Norit[®] pellets are by far the most economical choice of all the possible options for supports that were tested, and they did perform well. However, the largest drawback is the hygroscopic nature of phosphoric acid. After time had passed, a pool of viscous liquid was collecting in the round bottom flask (Figure 42). There were also white crystals, which suggested the formation of triethylammonium phosphate over time. The fact that a stable salt is created and not just a labile adduct explains the perfect retention characteristic for this support material. Unfortunately, the hygroscopic and potentially corrosive nature of the phosphoric acid-modified Norit[®] pellets and their liquid emanation disqualified this support material from practical applications in an air purification filter.



Figure 42. Phosphoric acid-modified Norit[®] pellets during the desorption experiment.

The base-modified filter would be the reverse of an acid-modified filter, and ideally a small, non-volatile amine should be applied. Unfortunately, the slightly less volatile aniline is toxic and had to be disqualified. Therefore, the inexpensive triethylamine was used as the basic modifier of the supports. The main concern with triethylamine was that it could detach from the surface and add to the smell of the waste container. However, as previously stated the DARCO[®] brand activated carbon can retain 160 mg of triethylamine per gram of unmodified support.⁶ In order to combat the leaching of triethylamine, the correct sequence of placing the filters within the assembled device is imperative. The initial prototype followed Figure 43, where the gentle air stream is propagated by two fans. This system oxidizes odor components such as aldehydes, in filter 1. Then, any formed or originally present acids are caught in the next, base-modified filter. In case any triethylamine is leaching from filter 2, the acid-modified filter 3 would catch it, along with any other alkaline odorous components. Finally, the non-polar filter 4, which will be discussed in the next section, would trap any hydrocarbon-based scent molecules, such as carvone from rotting meat. Finally, the last filter consists of unmodified DARCO

to act as a final catch for any residual scent molecules or odors being leached from the previous filters.

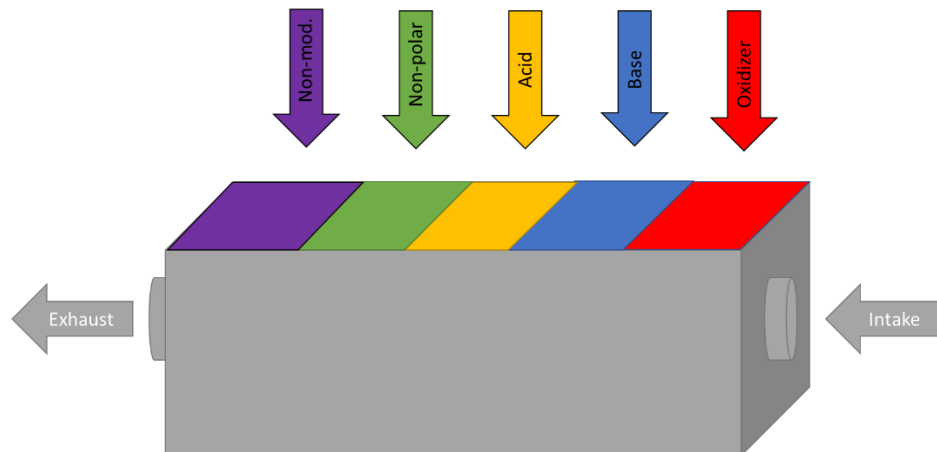


Figure 43. Prototype design for the air purification device used to remove VOCs from waste containers.

Preliminary experiments with this prototype involved using unmodified activated carbon to remove a colored, non-polar proprietary VOC. The prototype was connected to a sealed showcase via large-diameter plastic tubing to allow for unrestricted circulation of the air (Figure 44). The showcase featured two ports, one for intake, and one for exhaust machined into the top of the cover. There were several strips of paper taped to the top inside of the box in order to visualize the airflow within the container.

After dispersing the brown vapors of the VOC (Figure 44), the container was completely saturated. After 15 seconds of turning on the purification prototype, a clear improvement of the air quality can be seen. At about one minute, the color within the container is almost completely back to normal, only some lingering scent of the VOC

remained. Finally, after two minutes, the scent and color had been completely removed and the air quality returned to normal. Prolonged operation of the system did not show any leaching of the colored VOC.

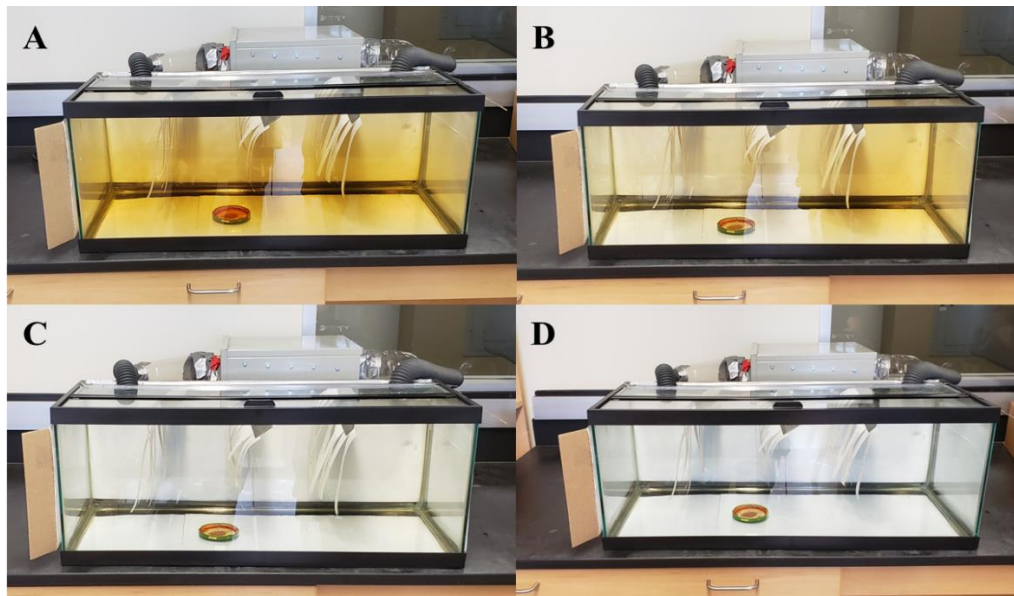


Figure 44. (A) Sealed showcase after dispersing proprietary colored VOC. (B) 15 seconds after activating the purification prototype. (C) 60 seconds after activating the prototype. (D) 120 seconds after activating the prototype. All color and scent had been removed from the showcase.

After functional acid- and base-modified filters were created, the next type of absorber was intended to remove nonprotic and less polar VOCs from an air stream. The idea was to maximize the retention of those types of odor molecules in modified DARCO[®] materials. In order to achieve this, two different nonpolar modifiers were tested on DARCO[®], cyclododecane and paraffin. The presence of films of these modifiers on the surface was thought to improve the absorption characteristics, as found previously for various oxide materials with layers of solvents on their surfaces.¹⁰

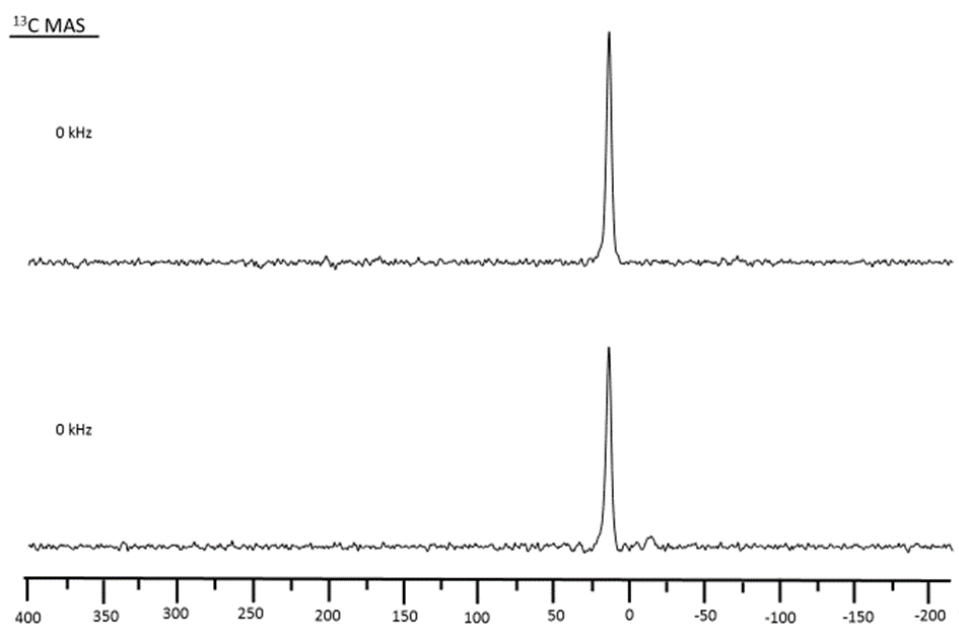


Figure 45. ^{13}C Wideline solid-state NMR spectra of cyclododecane adsorbed on DARCO (top), and cyclododecane-modified DARCO treated with ethyl acetate (bottom).

Cyclododecane-modification of DARCO[®] was straightforward. After dry grinding of the two solid components, solid-state NMR clearly showed mobility for cyclododecane on the surface based on the single sharp isotropic resonance at 23.4 ppm (Figure 45). Curiously, after exposure to ethyl acetate, the nonpolar test scent molecule, no additional signals can be seen despite a strong residual odor of ethyl acetate. For comparison, when acid-modified DARCO was treated with triethylamine, no residual odor of the base was noticeable, although it can be detected in the air in amounts of nanograms. The same results were found for paraffin, most importantly a collapse of the CSA in the ^{13}C NMR spectrum, but no additional signals for ethyl acetate. Despite of this, adsorption and desorption curves were obtained (Figures 46, 47).

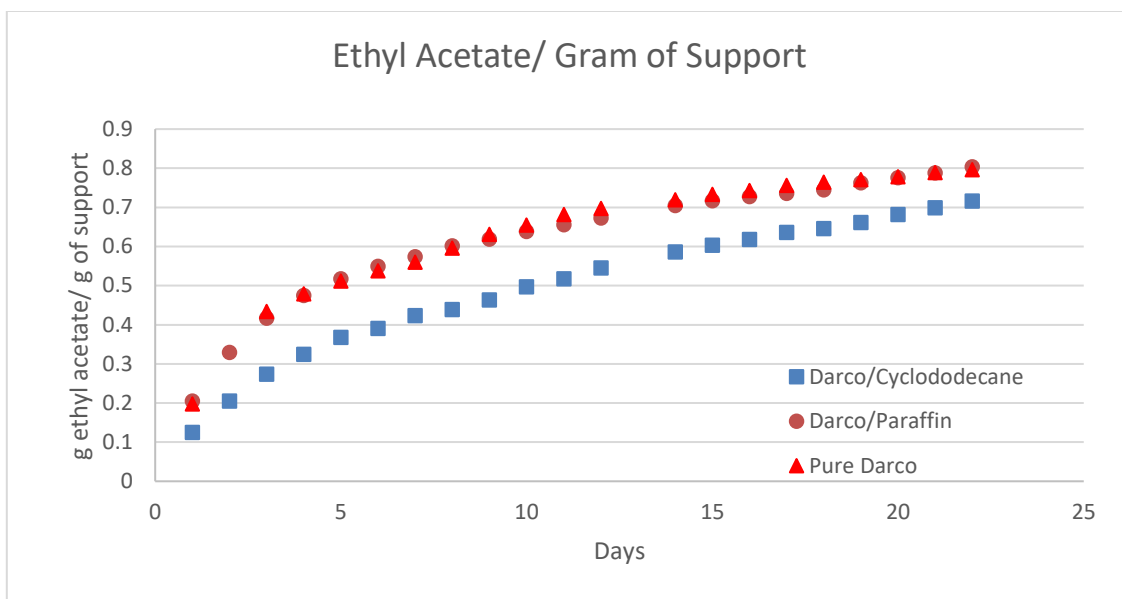


Figure 46. Adsorption curves for cyclododecane- and paraffin-modified DARCO[®] with ethyl acetate as the odor molecule.

As clearly shown by the absorption curve neither cyclododecane nor paraffin performed better than pure DARCO[®]. Unfortunately, neither the uptake nor the desorption of ethyl acetate changed much, regardless of the modifying agent. In the case of cyclododecane there was even less uptake of ethyl acetate as for unmodified DARCO, and more ready desorption. This led us to abandon the quest to optimize DARCO for nonprotic and less polar compounds and unmodified activated carbon was used instead for the prototype of odor absorber.

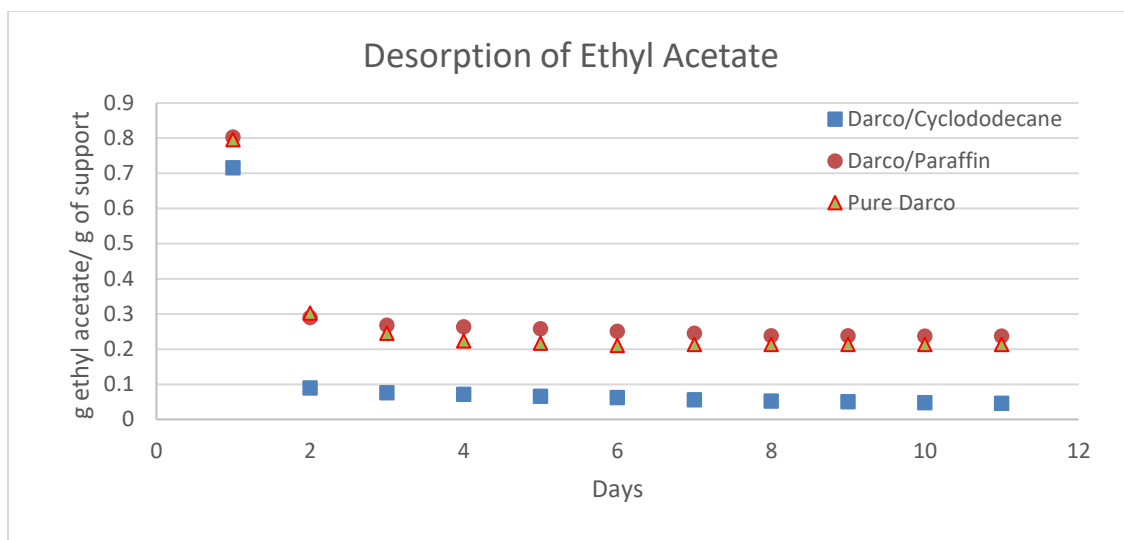


Figure 47. Desorption curve of cyclododecane- and paraffin-modified DARCO[®] treated with ethyl acetate as a nonprotic and less polar scent molecule.

The final filter material was developed as an oxidizer in order to remove sulfur-containing odors and aldehydes. For this purpose, two different solid oxidizers were tested. The first was commercially available meta-chloroperbenzoic acid (*m*-CPBA) and the second was the di(hydroperoxy)propane adduct of triphenylphosphine oxide (Ahn adduct). Unfortunately, *m*-CPBA proved to be too sensitive and did not retain its oxidizing power long enough at ambient temperature to be applicable in a commercial odor remover. Therefore, subsequently, more detailed tests involved using the solid oxidizer developed in the group, the Ahn adduct, to oxidize nonyl aldehyde, a common scent found in homes for the elderly (Figure 48).

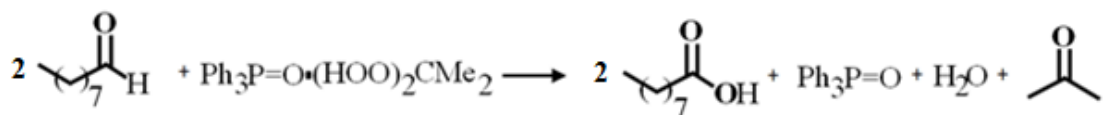


Figure 48. Reaction of nonyl aldehyde with di(hydroperoxy)propane adduct of triphenylphosphine oxide.

Table 12. Reaction conditions for the conversion of nonyl aldehyde to nonanoic acid using the di(hydroperoxy)propane adduct of triphenylphosphine oxide.

Ratio of nonyl aldehyde to oxidizer	Solvent	Temperature	Duration	Percent conversion to nonanoic acid
1.5	C ₆ D ₆	RT	90 mins	35
1.5	C ₆ D ₆	RT	Overnight	70
1.5	DCM	RT	Overnight	35
1.5	Toluene	60 °C	Overnight	30
1.0*	CDCl ₃	RT	90 mins	95

* Addition of one drop of H₂SO₄ as an acid catalyst

Several different experiments were performed in solution in order to determine the viability of the Ahn adduct^{5b} for oxidizing aldehydes (Table 12). Initial results lead to modest conversion of nonyl aldehyde to nonanoic acid. At first deuterated benzene overnight at room temperature seemed the best. The ¹³C solution NMR showed a small peak at 210 ppm that corresponds to unreacted aldehyde (Figure 49). The ¹H NMR was used to quantify the conversion by integration of the methyl protons at the end of the chains in both the aldehyde and acid (Figure 50).

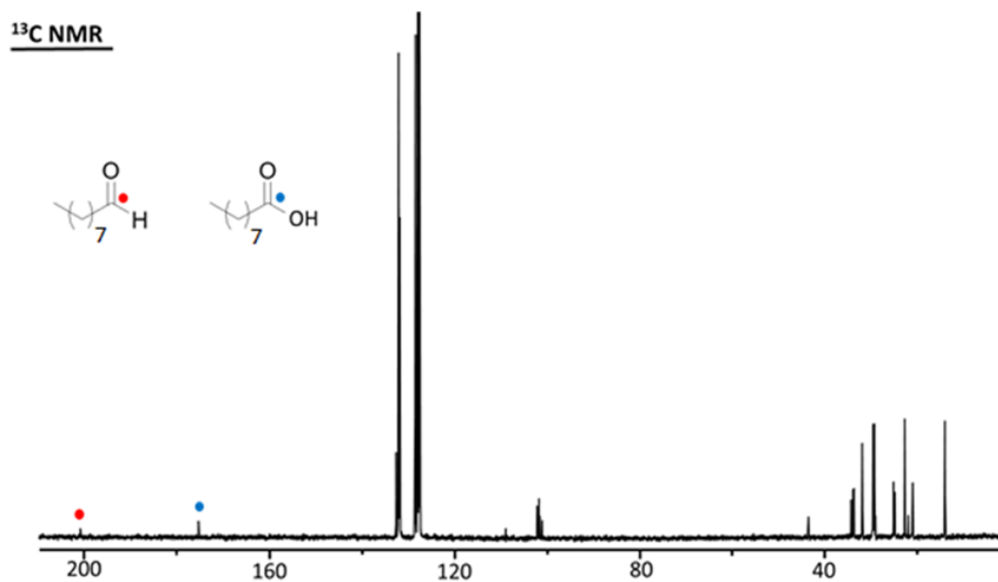


Figure 49. ¹³C NMR spectrum recorded after oxidation of nonyl aldehyde overnight in C₆D₆ at room temperature.

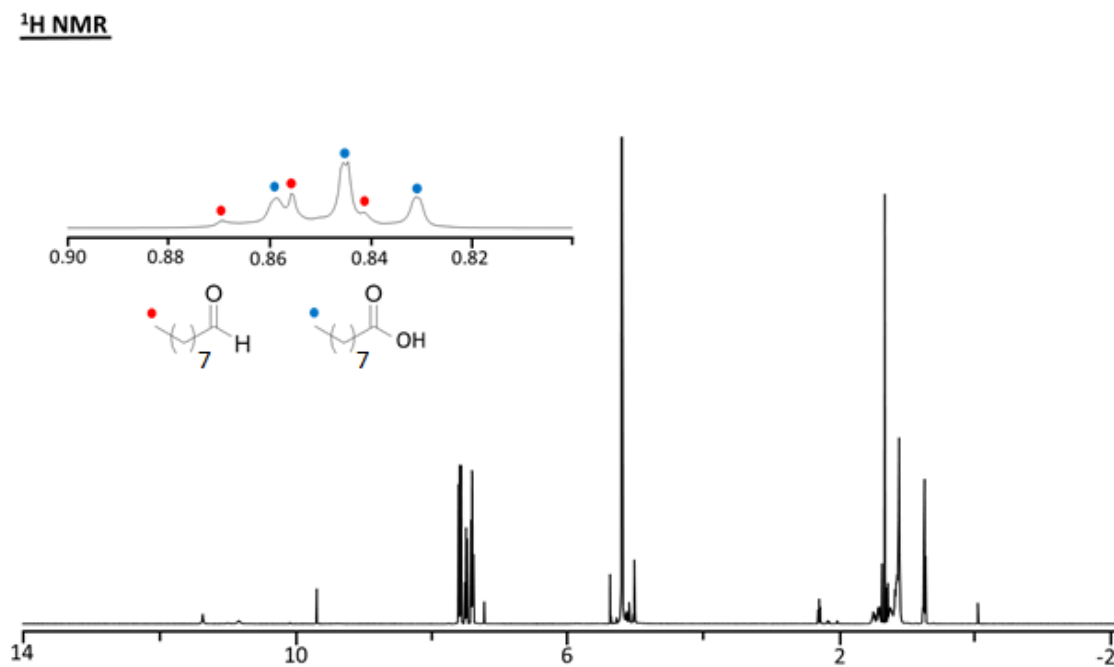


Figure 50. ¹H NMR spectrum after oxidation of nonyl aldehyde overnight in C₆D₆ at room temperature.

Additional experiments utilized H₂SO₄ as an acid catalyst. One drop of sulfuric acid was added before the addition of the oxidizer in hopes of acting as an acid activating the carbonyl group.

With the addition of an acid catalyst nonyl aldehyde was completely oxidized to nonanoic acid after only 90 minutes. The ¹³C NMR spectrum showed all desired resonances for nonanoic acid with no trace of nonyl aldehyde (Figure 51). The ¹H NMR showed only an insignificant integral for the aldehyde peak of nonanal (Figure 52), with an estimated amount of less than 5 percent of nonanal remaining.

¹³C NMR

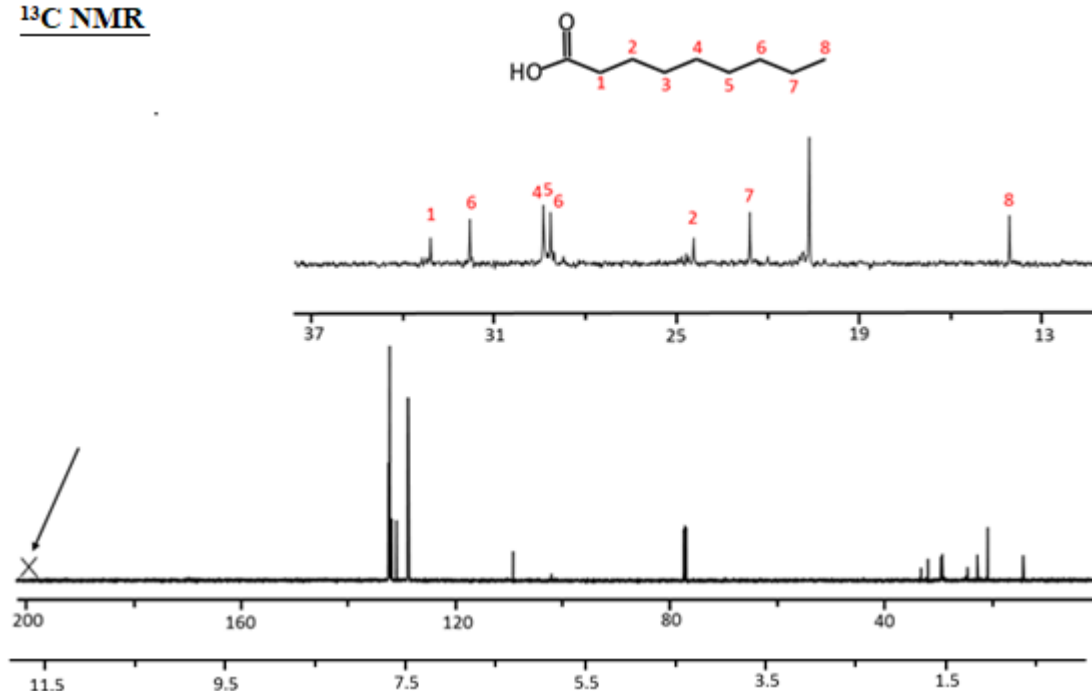


Figure 51. ¹³C NMR spectrum after the oxidation of nonyl aldehyde in 90 minutes at room temperature using one drop of H₂SO₄ as an acid catalyst.

¹H NMR

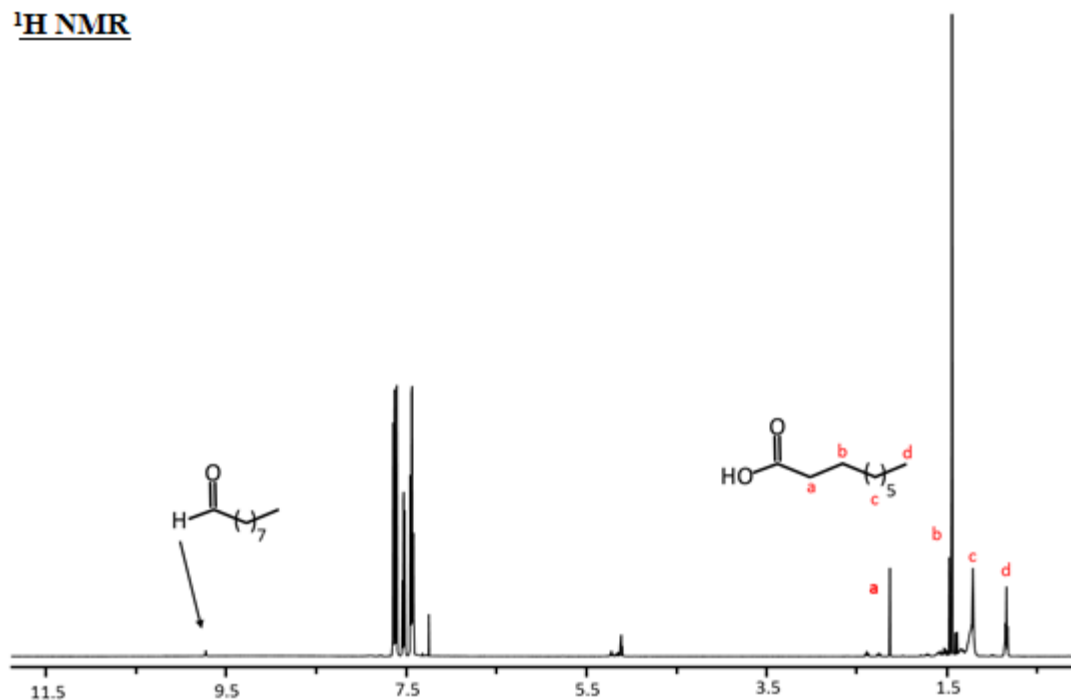


Figure 52. ¹H NMR spectrum after the oxidation of nonyl aldehyde in 90 minutes at room temperature using one drop of H₂SO₄ as an acid catalyst.

In the next step, the Ahn oxidizer^{5b} was applied to the Norit[®] brand of activated carbon that was comparatively inexpensive and available as pellets. In order to do this, 10 grams of Ahn oxidizer was dissolved in 100 mL of acetone and placed in a squirt bottle. 250 grams of Norit[®] pellets were placed in a large dish. The Norit[®] pellets were then doused with the solution of Ahn oxidizer^{5b} and left to dry for 2 hours. Initially, a ratio of oxidizer to Norit pellets was calculated to be 0.025 g of oxidizer per gram of Norit[®] pellets.

Finally, the prototype model was tested in a real-life dumpster at the waste disposal facility. Facility workers noticed a decrease in the scent of the large trash containers within the first hour. The prototype continued to work over the course of four days in the Texas summer in high temperatures and humidity before the facility employees reported that

they noticed a smell again. At this point the prototype was collected and the oxidizer was tested regarding its lifespan.

In order to determine whether the oxidizer had been spent prematurely, 35 g of the modified Norit pellets (corresponding to originally 0.90 g of Ahn adduct) that had been used in the trash container were extracted with 100 mL of dichloromethane. Then the resulting filtrate was tested with a procedure described earlier^{5b} and used to oxidize 1.28 g of triphenylphosphine. The ³¹P NMR spectrum of the reaction mixture is shown below (Figure 53). Based on the integration of the signals it can be concluded that after exposure to the odors in the trash container and an additional 5 days of exposure to the lab atmosphere, no more oxidizing power remained. This might have been the reason for the diminished odor removal after 4 days in the dumpster. Therefore, in a future real-life test, more Ahn oxidizer or another type of oxidizer will have to be included in the prototype.

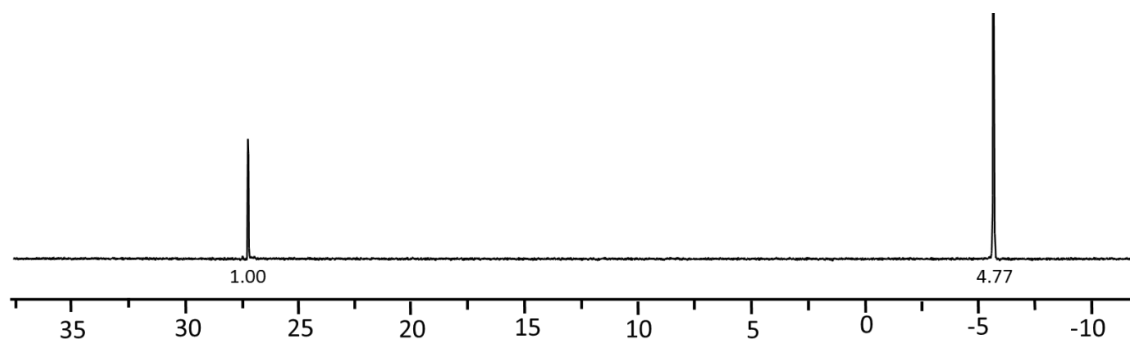


Figure 53. ³¹P NMR spectrum of the oxidizer after exposure to the trash container for 4 days. The upfield resonance corresponds to triphenylphosphine, the downfield one to triphenylphosphine oxide from the spent Ahn oxidizer.

A second test was performed in which excess Norit pellets modified with Ahn adduct were tested for their oxidizing power after being exposed in the lab atmosphere for two

weeks. The ^{31}P NMR spectrum showed triphenylphosphine oxide to triphenylphosphine in a 1 : 1.77 ratio (Figure 44). This shows that the oxidizer still maintained about 20% of its oxidizing power. Therefore, one can conclude that the oxidizer did not just decompose but "did its job" and was spent in odor removal reactions while being exposed in the dumpster.

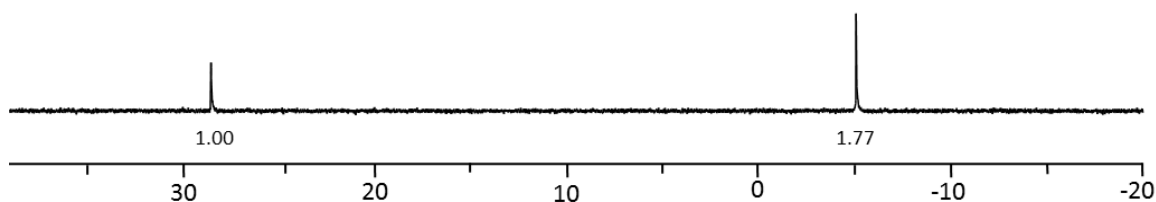


Figure 54. ^{31}P NMR of the extracted oxidizer and a test amount of triphenylphosphine oxide^{5b} after exposure to the lab atmosphere for 2 weeks.

Conclusion

The design of a new odor removing device was quite successful. The large surface area of activated carbon and mobility of common VOCs on the surface allows for a large uptake of odorous compounds. Additionally, using acid- and base-modified activated carbon guarantees an increased retention of VOCs over the course of time, most likely due to an irreversible salt or adduct formation on the surface of activated carbon.

The use of a solid oxidizer worked well based on the real-life test results, although improved longevity is sought in future experiments. This could easily be remedied by more Ahn-modified Norit[®] pellets, especially for large waste containers. However, different solid oxidizers are already in consideration, namely permanganate-based solid oxidizers because they are relatively cheap.

Overall, the prototype performed properly in the real-life experiments. The combination of materials worked well, especially given that results were noticed so quickly by employees of the facility. The prototype managed to completely remove odors for 4 days, before succumbing to the Texas summer atmosphere. Larger amounts of absorbents will be applied in future real-life experiments.

Experimental Section

All experiments were carried out in ambient atmosphere unless otherwise stated. Reagent grade solvents were purchased from VWR and Sigma Aldrich. KGB DARCO[®] brand activated carbon was purchased from Sigma Aldrich. The di(hydroperoxy)propane adduct of triphenylphosphine oxide was synthesized according to a literature procedure.^{5b}

The $^{13}\text{C}\{^1\text{H}\}$ CP, spinning (MAS) and static (wideline) NMR experiments were carried out on a Bruker Avance 400 solid-state NMR spectrometer (400 MHz for ^1H nuclei), equipped with standard two-channel 7 mm and 4 mm MAS probeheads. The standard single pulse (direct nuclear excitation with a 50° rf pulse) and CP pulse sequences were applied for and ^{13}C with recycle delays of 12 s, needed for complete spin-lattice relaxation. The contact times of 2 ms were adjusted for the standard $^{13}\text{C}\{^1\text{H}\}$ and CP/MAS NMR experiments. The tppm15 (two pulse phase modulation) pulse sequence has been used for complete ^1H decoupling. The external standard used for referencing the solid-state NMR chemical shifts was TMS.

Standard Solid Modification Procedure

The desired amount of surface-modifying agent corresponding to a sub-monolayer surface coverage was weighed out on an analytical balance. Then 1 g of a support material was dry ground with the modifying agent for 5 minutes. The samples were then placed in glass vials for storage.

Large Scale Solid Modification Procedure for Oxidizing Filter Materials

10.0 g of solid modifier was dissolved in 100 mL of acetone and placed inside a squirt bottle. Approximately 250 grams of Norit[®] pellets were placed inside a large glass dish and the oxidizer solution was slowly added to the Norit[®] pellets while stirring gently. The wet pellets were then left to dry for 2 hours and placed inside the mesh filter frames.

Large Scale Liquid Modification Procedure for Filter Materials

A portion of the modifying liquid was placed in a large petri dish and put inside a large steel paint can. The desired support was then placed inside a mesh bag and suspended inside the can. The can was sealed and allowed to sit for at least 7 days.

Testing Oxidative Power of Used Oxidizing Filter Material

35 g of the Ahn modified Norit[®] pellets were stirred with 200 mL of dichloromethane for 2 hours. A filtration was performed, and the filtrate was collected and calculated to contain 0.905 g (2.328 mmol) of the Ahn adduct. Then 1.280 g (4.599 mmol) of triphenylphosphine oxide, corresponding to a 2:1 ratio, was added to the filtrate and

stirred at room temperature for 3 hours. The solvent was evaporated, and the resulting solids were dissolved in deuterated dichloromethane for solution NMR analysis.

Oxidation of Nonyl Aldehyde with the Di(hydroperoxy)propane Adduct of Triphenylphosphine Oxide

0.05 mL of nonyl aldehyde was added to 1 mL of deuterated chloroform in a glass vial. One drop of concentrated sulfuric acid was added to the vial. 0.106 g of Ahn adduct was added to the vial. The contents were stirred for 90 minutes and then solution NMR spectroscopy was performed.

References

1. M. Statheropoulos, A. Agapiou G. Pallis, *Atmos. Environ.* **2005**, *39*, 4639-4645.
2. Y. Di, J. Liu, S. Liu, L. Yan, *JA&WMA*, **2013**, *63*, 1173-1181.
3. T. Wu, X. Wang, D. Li, Z. Yi, *Atmos. Environ.* **2010**, *44*, 5065-5071.
4. M. A. Yakovleva, E. V. Perova, I. S. Kislina, N. B. Librosvich, S. E. Nefedov, *Russ. J. Inorg. Chem.* **2010**, *55*, 1228–1233.
5. (a) C. R. Hilliard, N. Bhuvanesh, J. A. Gladysz, J. Blümel, *Dalton Trans.* **2012**, *41*, 1742-1754. (b) S. H. Ahn, K. J. Cluff, N. Bhuvanesh, J. Blümel, *Angew. Chem.* **2015**, *127*, 13539-135

6. P. Harb, N. Locoge, F. Thevenet, *Chem. Eng. J.* **2020**, *380*, 122525.
7. X. Li, L. Zhang, Z. Yang, P. Wang, Y. Yan, J. Ran, *Sep. Purif. Technol.* **2020**, *235*, 116213.
8. K. Vikrant, K.-H. Kim, W. Peng, S. Ge, Y. Sik Ok, *Chem. Eng. J.* **2020**, *387*, 123943.
9. L. Ma, M. He, P. Fu, X. Jiang, W. Lv, Y. Huang, Y. Liu, H. Wang, *Sep. Purif. Technol.* **2020**, *235*, 116146.
10. H. Marsh, F. Rodriguez-Reinoso, *Activated Carbon*, Elsevier, Amsterdam 2006.
11. N. Hagemann, K. Spokas, H. -P. Schmidt, R. Kagi, M. A. Bohler, T. D. Bucheli, *Water* **2018**, *10*, 182.
12. N. Le-Minh, E. C. Sivret, A. Shammay, R. M. Stuetz, *Crit. Rev. Environ. Sci. Tech.* **2018**, *48*, 341-375.
13. M. Smisek, S. Cerney, *Activated Carbon*, Elsevier Co., New York 1970.
14. J. W. H. Smith, J. V. Romero, T. R. Dahn, K. Dunphy, B. Sullivan, M. Mallay, L. M. Croll, J. H. Reynolds, C. Andress, J. R. Dahn, *J. Colloid Interface Sci.* **2011**, *364*, 178-194.
15. Unpublished results of J. W. Benzie.

CHAPTER V

CONCLUSION

The adsorption studies performed provided fundamental knowledge about the interactions of molecules on different surfaces and helped aid the design of a prototype air purification system. First, the translational mobility of triphenylphosphine oxide on the surface of alumina was proven. Different surface coverages, from a densely packed monolayer (99% coverage) to a dilute sub-monolayer (25%) were produced. The samples were studied by diverse multinuclear ^1H , ^{13}C , and ^{31}P variable temperature solid-state NMR techniques. The interactions of **1** with the surface were determined as consisting mainly of hydrogen bonding of the P=O group to OH groups on the surface. The ^{31}P solid-state NMR spectra proved that even at low temperatures the molecules of triphenylphosphine oxide are highly mobile on the surface. Using T_1 and T_2 relaxation time analyses of the ^{31}P resonance in the solid state at variable temperatures allowed the identification and quantification of two different modes of mobility. Besides the translational mobility that consists of jumps from one hydrogen-bonding OH site on the surface to an adjacent one, a rotational movement around the axis defined by the P=O group of triphenylphosphine oxide was found.

Ferrocene was adsorbed on the surface of silica and activated carbon within the pores by dry grinding in the absence of a solvent at room temperature. Using variable temperature ^{13}C and ^2H solid-state NMR and T_1 relaxation time measurements, the dynamics of ferrocene on the surfaces of silica and activated carbon within the pores has been quantitatively characterized on the molecular scale. The obtained data indicate that

ferrocene molecules show a liquid-like behavior on the surface. Fast exchange between isotropically moving molecules and surface-attached molecular states of ferrocene has been found in samples with sub-monolayer surface coverages. The surface-attached molecular states have been characterized by the free energies ΔG^\ddagger of 6.1 kcal/mol for silica and ΔG^\ddagger of 6.2 kcal/mol for activated carbon at 223 and 263 K, respectively. The horizontally oriented ferrocene molecules are the most thermodynamically stable states on the surfaces of both materials. These molecules exhibit fast C_5 rotation of the Cp rings, as established by low temperature ^{13}C and ^2H NMR. The interactions of ferrocene with the pore surfaces have been characterized by adsorption enthalpies measured as -8.4 to -7.0 kcal/mol and -6.7 kcal/mol for activated carbon and silica, respectively. It has been suggested that the ferrocene–surface interactions for both support materials have a polar character.

Finally, a prototype air purification system was developed in conjunction with Waste Equipment LLC. Several different modified filters were developed including acid- and base-modified activated carbon filters. A new type of solid oxidizer-modified filter was also developed. The prototype performed well in a real-life test during the Texas summer and mitigated the scent of a large trash container over the course of four days. Additional research is continuing to increase the longevity of the system in order to work for weeks or months at a time.

APPENDIX A

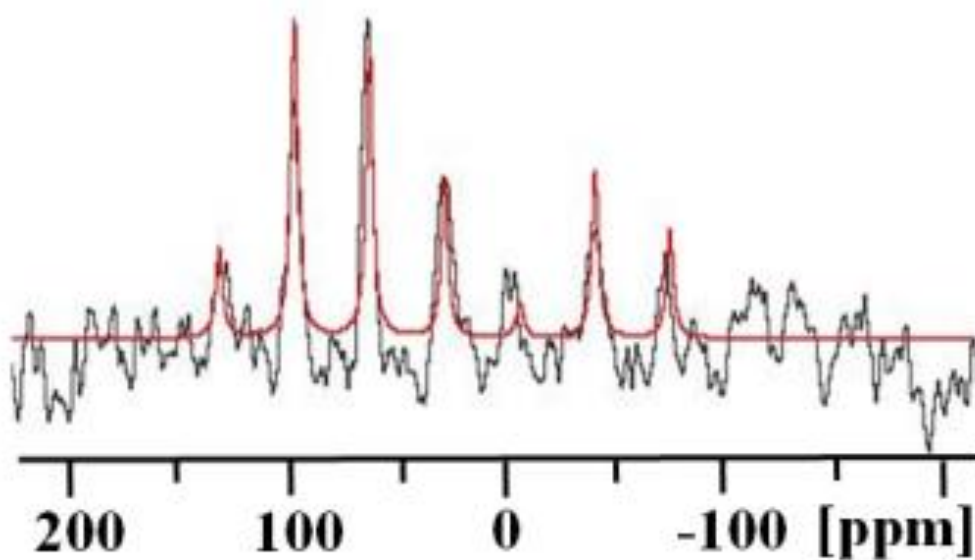


Figure A1. Experimental (black) and simulated (red) $^{31}\text{P}\{^1\text{H}\}$ MAS NMR spectrum of polycrystalline **1**, spinning at 5 kHz.

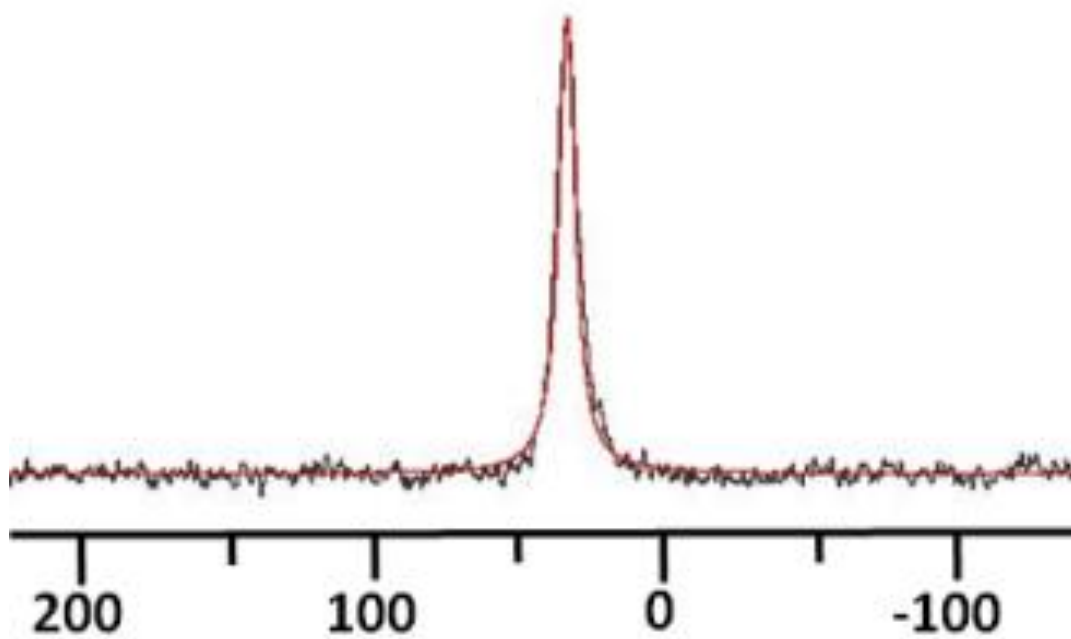


Figure A3. $^{31}\text{P}\{^1\text{H}\}$ static NMR spectrum of **5**, recorded at 295 K (black line), and simulated spectrum (red line).

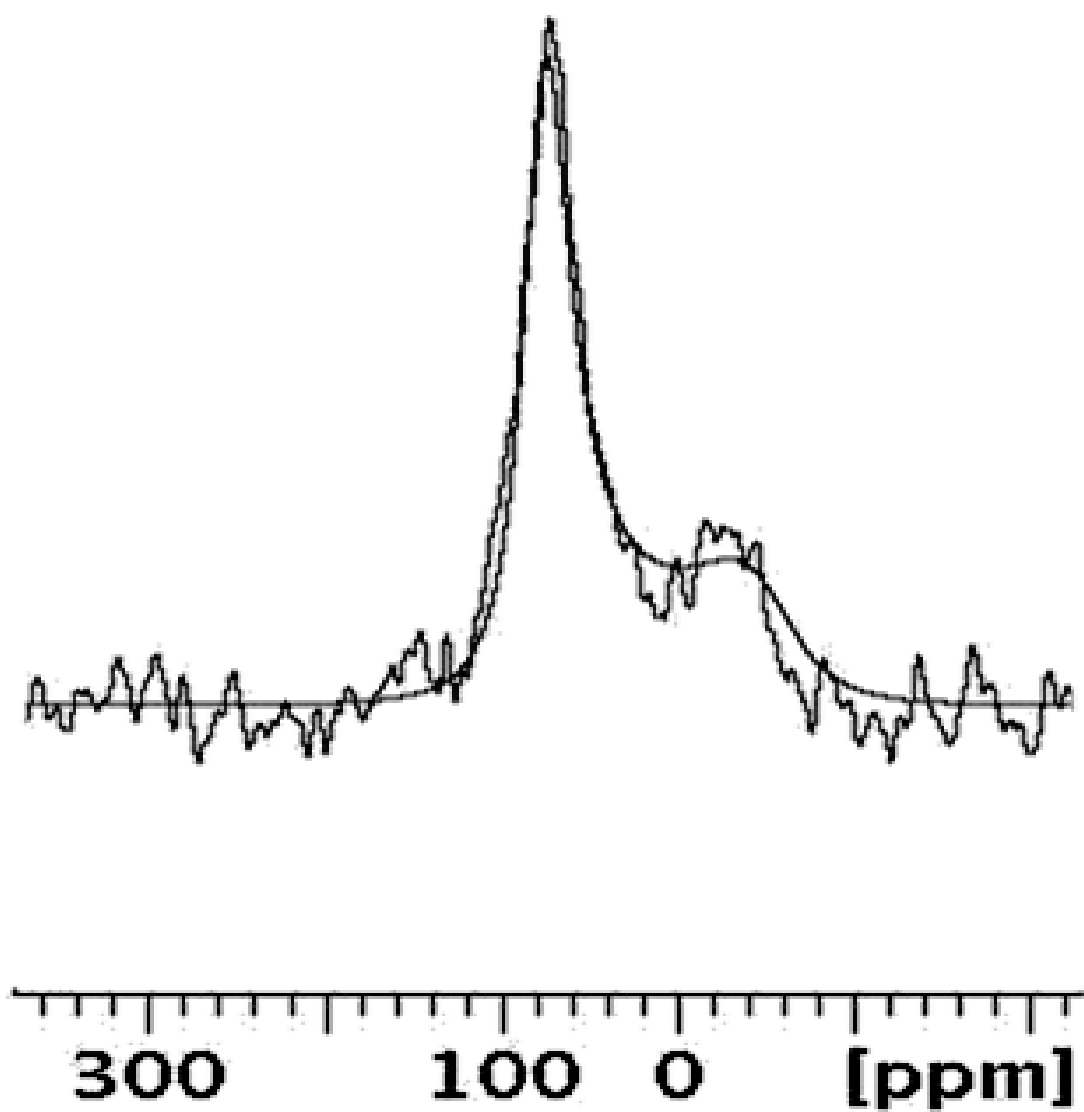


Figure A5. Experimental and simulated $^{31}\text{P}\{^1\text{H}\}$ wideline NMR spectrum of **4** at 253 K.

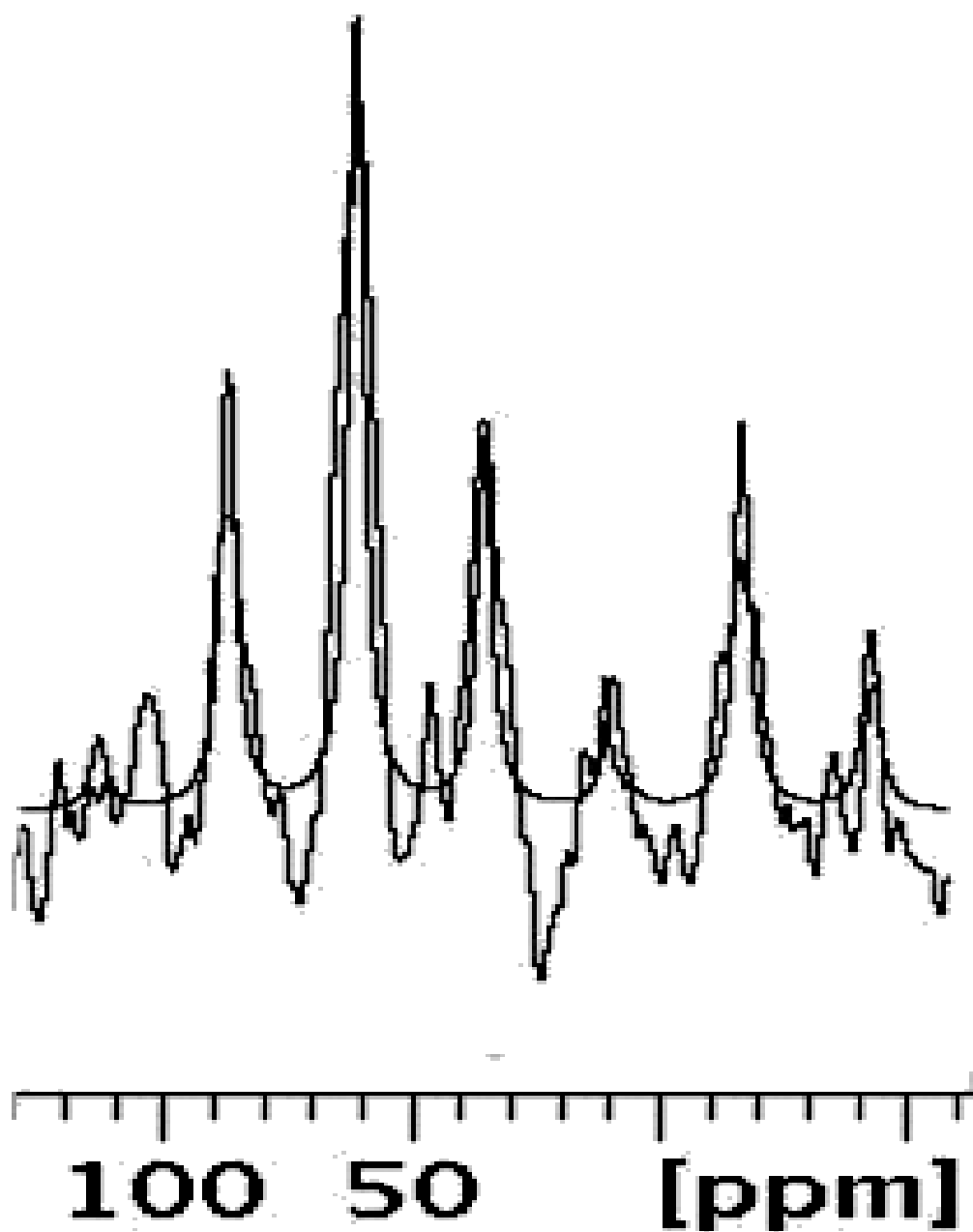


Figure A6. Experimental and simulated $^{31}\text{P}\{^1\text{H}\}$ NMR spectrum of **4** at 183 K, spinning with a rate of 4 kHz.